

AD-763 718

APPLICATION OF EXTENDED KALMAN FILTER-
ING TO A DYNAMIC LABORATORY CALIBRATION
OF AN INERTIAL NAVIGATION SYSTEM

Frazier J. Hellings

Aerospace Corporation

Prepared for:

Space and Missile Systems Organization

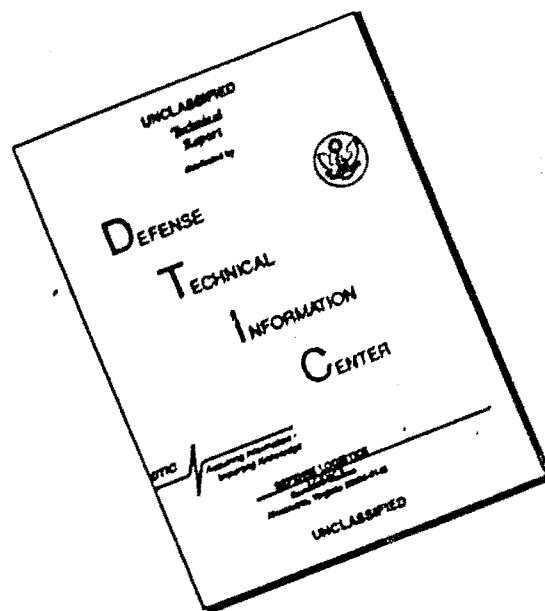
12 March 1973

DISTRIBUTED BY:

NTIS

National Technical Information Service
U. S. DEPARTMENT OF COMMERCE
5285 Port Royal Road, Springfield Va. 22151

DISCLAIMER NOTICE



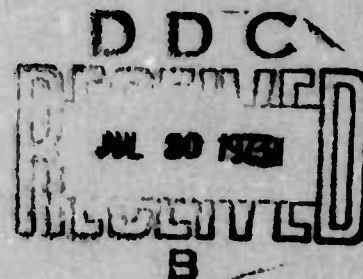
THIS DOCUMENT IS BEST QUALITY AVAILABLE. THE COPY FURNISHED TO DTIC CONTAINED A SIGNIFICANT NUMBER OF PAGES WHICH DO NOT REPRODUCE LEGIBLY.

AD 763718

Application of Extended Kalman Filtering to a Dynamic Laboratory Calibration of an Inertial Navigation System

Prepared by FRAZIER J. HELLINGS

73 MAR 12



Engineering Science Operations
THE AEROSPACE CORPORATION

Prepared for SPACE AND MISSILE SYSTEMS ORGANIZATION
AIR FORCE SYSTEMS COMMAND
LOS ANGELES AIR FORCE STATION
Los Angeles, California

Reproduced by
NATIONAL TECHNICAL
INFORMATION SERVICE
U.S. Department of Commerce
Springfield VA 22151

APPROVED FOR PUBLIC RELEASE: DISTRIBUTION UNLIMITED

UNCLASSIFIED

Security Classification

DOCUMENT CONTROL DATA - R & D

(Security classification of title, body of abstract and indexing annotation must be entered when the overall report is class.)

1 ORIGINATING ACTIVITY (Corporate author)		2a REPORT SECURITY CLASSIFICATION	
The Aerospace Corporation El Segundo, California		Unclassified	
3 REPORT TITLE		2b GROUP	
APPLICATION OF EXTENDED KALMAN FILTERING TO A DYNAMIC LABORATORY CALIBRATION OF AN INERTIAL NAVIGATION SYSTEM			
4 DESCRIPTIVE NOTES (Type of report and inclusive dates)			
5 AUTHOR(S) (First name, middle initial, last name)			
Frazier J. Hellings			
6 REPORT DATE	7a TOTAL NO. OF PAGES	7b NO. OF REFS	
73 MAR 12	247 250	20	
8a CONTRACT OR GRANT NO.	9a ORIGINATOR'S REPORT NUMBER(S)		
F04701-72-C-0073	TR-0073(3115)-3		
b PROJECT NO	9b OTHER REPORT NO(S) (An) other numbers that may be assigned this report)		
	SAMSO-TR-73-219		
10 DISTRIBUTION STATEMENT			
Approved for public release; distribution unlimited.			
11 SUPPLEMENTARY NOTES		12 SPONSORING MILITARY ACTIVITY	
13 ABSTRACT			
<p>The report describes a data reduction technique that obtains estimates of inertial sensor error model coefficients from a dynamic laboratory calibration of a typical Inertial Navigation System. The error model coefficients are those associated with gyros, accelerometers, and their misalignment errors that have been found by test and analysis to be the predominant sources of error affecting system accuracy. All the error terms considered are categorized as either fixed (independent of applied acceleration), first-order (proportional to the first power of acceleration), or higher-order terms, which are proportional to the square or cube of acceleration. In the case of the higher-order terms, the error model coefficients of inertial grade sensors are from one to four orders of magnitude smaller than the fixed and first-order terms. To obtain measurable quantities of these error sources requires the application of precise high-acceleration inputs from a laboratory test device. Until 1971, there were no laboratory test devices that maintained a low angular-rate environment while providing precise high-acceleration inputs to permit recovery of the high-order gyro compliance terms. In 1971, the United States Air Force completed the 260-inch Radius Precision Centrifuge which is located at the Central Inertial Guidance Test Facility, Holloman AFB, New Mexico. The unique feature of this centrifuge that permits high-acceleration testing of gyros and/or systems is that the test specimen is located on a counter-rotating platform that isolates the gyros from the centrifuge angular rate. Unfortunately, accurate estimates of the error terms require more than a precision test device.</p>			

UNCLASSIFIED

Security Classification

KEY WORDS

Extended Kalman Filter

System Calibration

Centrifuge

Inertial Navigation System

Estimation Theory

Abstract (Continued)

In addition to the test device, one must have a positively controlled test procedure that varies the system orientation with respect to the input acceleration to provide better observation of the error coefficients in the measurement data and a data reduction program that provides the "best" estimates of the error coefficients from noisy measurement data. This report proposes a dynamic test procedure and an associated data reduction method for obtaining estimates of the error model coefficients from a 260-inch Centrifuge System Test.

The dynamic test procedure is obtained by command torquing the platform gyros to drive the platform through a prespecified torque profile so that each axis is subjected to the applied acceleration. Since the platform motion is a combination of commanded rate, applied earth-rate, and drift due to the gyro error terms, tracking the platform motion with Euler angle rates provides the basis for the state dynamics. The measurements, obtained from the triad of platform accelerometers, are functions of the accelerometer error terms and the Euler angles, which in turn contain the drift motion due to the gyro error coefficients. Therefore, the problem is a parameter estimation problem where the Euler angles and error model coefficients are designed as system states to be estimated from noisy measurements. Since both the state and measurement equations are nonlinear functions of the state variables, an Extended Kalman Filter is applied.

The results of two simulations verify the application of the filtering algorithm to the calibration problem. The results show that significant improvement can be obtained in reducing the time required to calibrate an Inertial Navigation System. In addition, a method of applying the off-diagonal terms of the filtering error covariance matrix provides a new dimension in evaluating filter performance with respect to system observability.

UNCLASSIFIED

Security Classification

Air Force Report No.
SAMSO-TR-73-219

Aerospace Report No.
TR-0073(3115)-3

APPLICATION OF EXTENDED KALMAN FILTERING TO A
DYNAMIC LABORATORY CALIBRATION OF AN
INERTIAL NAVIGATION SYSTEM

Prepared by
Frazier J. Hellings

73 MAR 12

Engineering Science Operations
THE AEROSPACE CORPORATION

Prepared for
SPACE AND MISSILE SYSTEMS ORGANIZATION
AIR FORCE SYSTEMS COMMAND
LOS ANGELES AIR FORCE STATION
Los Angeles, California

Approved for public release;
distribution unlimited.

FOREWORD

This report is published by The Aerospace Corporation, El Segundo, California, under Air Force Contract No. F04701-72-C-0073. This report was prepared by Major Frazier J. Hellings as a part of the Inertially Designated Tracker (IDT) Study. IDT is a part of the Range Improvement Study Project (RISP). RISP, in turn, is a study conducted by the Space and Missile Test Center (SAMTEC). SAMTEC has provided funds for Aerospace support of the IDT Study, with Dr. Edwin B. Stear, Senior Consultant to SAMTEC, acting as coordinator of the effort. The IDT concept was originated by Dr. Stear.

In addition, the Central Inertial Guidance Test Facility (CIGTF), Holloman Air Force Base, New Mexico, has provided additional funds to defray the computer costs associated with that portion of the IDT study reported herein. All funding for IDT is through SAMSO, with Aerospace support then being provided under the Air Force Contract cited above. Cognizant SAMSO Air Force officers are Cols. P. V. Osburn and H. V. Wright, and Lt. Col. W. J. Lantier. The Aerospace Project Manager for IDT is Dr. Joseph L. LeMay.

This report, which documents research carried out from January 1972 through March 1973, was submitted for review and approval on 8 May 1973 to W. J. Lantier, Lt. Col., USAF.

Approved by

Joseph L. LeMay
Joseph L. LeMay
Project Manager
IDT Study

Publication of this report does not constitute Air Force approval of the report's findings or conclusions. It is published only for the exchange and stimulation of ideas.

Ward J. Lantier
W. J. Lantier
Lt. Col., USAF

ABSTRACT

The report describes a data reduction technique that obtains estimates of inertial sensor error model coefficients from a dynamic laboratory calibration of a typical Inertial Navigation System. The error model coefficients are those associated with gyros, accelerometers, and their misalignment errors that have been found by test and analysis to be the predominant sources of error affecting system accuracy. All the error terms considered are categorized as either fixed (independent of applied acceleration), first-order (proportional to the first power of acceleration), or higher-order terms, which are proportional to the square or cube of acceleration. In the case of the higher-order terms, the error model coefficients of inertial grade sensors are from one to four orders of magnitude smaller than the fixed and first-order terms. To obtain measurable quantities of these error sources requires the application of precise high-acceleration inputs from a laboratory test device. Until 1971, there were no laboratory test devices that maintained a low angular-rate environment while providing precise high-acceleration inputs to permit recovery of the high-order gyro compliance terms. In 1971, the United States Air Force completed the 260-inch Radius Precision Centrifuge which is located at the Central Inertial Guidance Test Facility, Holloman AFB, New Mexico. The unique feature of this centrifuge that permits high-acceleration testing of gyros and/or systems is that the test specimen is located on a counter-rotating platform that isolates the gyros from the centrifuge angular rate. Unfortunately, accurate estimates of the error terms require more than a precision test device. In addition to the test device, one must have a positively controlled test procedure that varies the system orientation with respect to the input acceleration to provide better observation of the error coefficients in the measurement data and a data reduction program that provides the "best" estimates of the error coefficients from noisy measurement data. This report proposes a dynamic

Preceding page blank

test procedure and an associated data reduction method for obtaining estimates of the error model coefficients from a 260-inch Centrifuge System Test.

The dynamic test procedure is obtained by command torquing the platform gyros to drive the platform through a prespecified torque profile so that each axis is subjected to the applied acceleration. Since the platform motion is a combination of commanded rate, applied earth-rate, and drift due to the gyro error terms, tracking the platform motion with Euler angle rates provides the basis for the state dynamics. The measurements, obtained from the triad of platform accelerometers, are functions of the accelerometer error terms and the Euler angles, which in turn contain the drift motion due to the gyro error coefficients. Therefore, the problem is a parameter estimation problem where the Euler angles and error model coefficients are designed as system states to be estimated from noisy measurements. Since both the state and measurement equations are non-linear functions of the state variables, an Extended Kalman Filter is applied.

The results of two simulations verify the application of the filtering algorithm to the calibration problem. The results show that significant improvement can be obtained in reducing the time required to calibrate an Inertial Navigation System. In addition, a method of applying the off-diagonal terms of the filtering error covariance matrix provides a new dimension in evaluating filter performance with respect to system observability.

CONTENTS

1.	INTRODUCTION	1
1.1	Objective	1
1.2	Problem Description	2
1.3	Problem Approach	6
1.4	Scope of Effort	11
2.	SENSOR AND PLATFORM PERFORMANCE MODELS .	13
2.1	Vector and Matrix Notation	13
2.2	Gyro Performance Model	16
2.3	Accelerometer Performance Model	27
2.4	Platform Performance Models	32
3.	APPLIED ACCELERATION	39
3.1	Description of the 260-Inch Centrifuge	39
3.2	Coordinate Transformations	44
3.2.1	Inertial - Earth Transformation	44
3.2.2	Earth-Centrifuge Main Arm Transformation	49
3.2.3	Centrifuge Main Arm - Centrifuge Counter-Rotating Platform Transformation	56
3.2.4	System Inner Gimbal Platform- Sensor Transformation	61
3.3	Applied Acceleration Equation	68
4.	EXTENDED KALMAN FILTER EQUATIONS	75
4.1	State Variables	77
4.2	System Dynamic Model	82
4.3	State and Measurement Equations	86
4.4	Extended Kalman Filter Equations and Filtering Algorithm	97
5.	SIMULATION OF A 1-g CALIBRATION	119
5.1	Simulation States and Equations	119
5.2	Measurement Simulation	125

CONTENTS (Continued)

5.3	Filter Algorithm	137
5.4	Simulation Results	144
6.	SIMULATION OF A CENTRIFUGE CALIBRATION . . .	161
6.1	Simulation States and Equations	161
6.2	Measurement Simulation	175
6.3	Filter Algorithm	179
6.4	Simulation Results	180
7.	SUMMARY AND RECOMMENDATIONS FOR FUTURE STUDY	197
	REFERENCES	203
	APPENDIXES	
A.	KINEMATIC ACCELERATION OF THE SENSOR FRAME	205
B.	CALCULATION OF APPLIED ACCELERATION GROUP 2 TERMS	215
B.1	Calculations for the 1-g Simulation	215
B.2	Calculations for the Centrifuge Simulation . . .	220
C.	ANALYTIC PARTIALS	227
C.1	Analytic Partial for the 1-g Simulation	227
C.2	Analytic Partial for the Centrifuge Simulation	232

FIGURES

1.1.	260-Inch Radius Precision Centrifuge	5
2.1.	Line Schematic of a Single-Degree-of-Freedom Integrating Gyro	17
2.2.	Line Schematic of a Force-Rebalance Pendulous Accelerometer	28
3.1.	Simplified Centrifuge Acceleration Profile	43
3.2.	Inertial and Earth Coordinate Frames	45
3.3.	Accelerometer at Rest on a Spherical Homogeneous Nonrotating Earth	48
3.4.	Local Gravity Vector	50
3.5.	Earth - Centrifuge Main Arm Coordinate Frames	51
3.6.	Centrifuge Main Arm - CRP Coordinate Frames	57
3.7.	Accelerometer Case Axis System	63
3.8.	Gyro Case Axis System	64
3.9.	Platform - Accelerometer Coordinate Frames	65
3.10.	Platform - Gyro Coordinate Frames	67
4.1.	State Estimation Problem	79
4.2.	Euler Transformation	83
4.3.	Schematic of the Extended Kalman Filter Algorithm	116
5.1.	Flow Diagram of Measurement Simulation Program	134
5.2.	Command Torque Generation Block	135
5.3.	Flow Diagram of Filter Algorithm	138

FIGURES (Continued)

5.4.	Schematic of the Alternate Extended Kalman Filter Algorithm	145
A.1.	Vector Map of Basic Coordinate Frames	208

TABLES

4.1.	States of the Calibration Process	81
5.1.	States of the 1-g Simulation	121
5.2.	Initial State Means and Standard Deviations	126
5.3.	Carousel VB 1-Sigma Error Budget	128
5.4.	Standard Deviations of Disturbance and Measurement Noise	129
5.5.	Values of Initial State Estimate for 1-g Simulation	147
5.6.	Results of 10-Percent Case for 1-g Simulation	148
5.7.	Accelerometer Parameter Correlation Pattern for 1-g Simulation	151
5.8.	Results of 30-Percent Case for 1-g Simulation	154
5.9.	Results of 60-Percent Case for 1-g Simulation	156
5.10.	Results of 100-Percent Case for 1-g Simulation	157
5.11.	Comparison of Basic and Alternate Filters for Δv Approximation	159
6.1.	States of the Centrifuge Simulation	162
6.2.	State Variables for Three Program Options	164
6.3.	Input Constants for Centrifuge Simulation	166
6.4.	Initial State Means and Standard Deviations	176
6.5.	Standard Deviations of Disturbance and Measurement Noise	177

TABLES (Continued)

6.6.	Improvement in Estimates Versus Platform Orientation Based on Correlation Pattern Data	183
6.7.	Comparison of Transition Options	186
6.8.	Comparison of Analytic and Numerical Partial	188
6.9.	Results of 30-Percent Case Basic Option	189
6.10.	Results of 30-Percent Case Option 1	190
6.11.	Results of 30-Percent Case Option 2	191
6.12.	Results of 100-Percent Case Basic Option	194
6.13.	Comparison of Filter Performance for 1-g and Centrifuge Simulations	195

SECTION 1

INTRODUCTION

1.1 OBJECTIVE

The objective of the report is to develop a data reduction technique that obtains estimates of inertial sensor error model coefficients from a dynamic laboratory calibration of a typical Inertial Navigation System (INS). The error model coefficients are those associated with the error sources that affect the ability of the inertial system to measure accurately the velocity, position, or attitude profile of the inertially guided vehicle. These inertial measurement errors are represented by gyro, accelerometer, and alignment errors; they have been found by test and analysis to be the predominant sources of error affecting system accuracy [1,2]. Present day accuracy requirements for inertial navigators are so stringent that gyro and accelerometer component manufacturing has reached the state-of-the-art in material selection, production tolerances, and assembly techniques. The cost of product improvement has become intolerable. Other than searching for completely new developments in sensor design, the most feasible approach to the problem is to find test and data reduction techniques that accurately determine all measurable sensor error sources. Once these errors are measured, a systems approach can be taken to either compensate for the errors or select a system configuration or mission profile that minimizes the effects of these errors on system accuracy. Computational schemes in airborne computers have become sophisticated enough to permit accurate compensation for bias and

scale-factor errors for each accelerometer, provide for precision torquing of platform gyros to compensate for fixed-restraint gyro drift, and finally to perform coordinate transformations to account for sensor misalignments. However, this assumes that accurate knowledge of each error coefficient is available for insertion in the navigation software program. Gyro mass unbalance terms are usually compensated by physical adjustment of gyro-float-trim weights via a remote adjustment mechanism. All the error terms discussed thus far are categorized as either fixed (i.e., independent of acceleration) or first-order terms (i.e., proportional to the first power of acceleration); they are the only error categories where compensation techniques are practical. Therefore, the purpose of obtaining accurate estimates of these error model coefficients, obviously, is to directly improve system performance through error compensation. Higher-order error terms that are proportional to the square or cube of acceleration are obtained for incorporation into system error analysis programs so that their effects on system accuracy can be ascertained. In addition, these error sources are also used in flight simulation programs to determine the best sensor orientations, platform orientation, and mission profiles for minimizing the effects of these error sources on system performance. Therefore, the purpose of obtaining accurate estimates of the higher-order error model coefficients is to provide for system accuracy determination and design optimization.

1.2 PROBLEM DESCRIPTION

Accurate estimates of the fixed and first-order coefficients can be obtained by using present day laboratory test methods in which the

system is precisely positioned and rotated with respect to the earth-rate and local-gravity vectors, quantities which are accurately determined at the test site. Sufficient measurements of the system output are taken to permit the performance of a least-squares-regression analysis on the measurement data with respect to a mathematical model of the system output. The math model is a function of the desired error model coefficients and the applied earth-rate and local-gravity vector components. In the case of the higher-order error terms, the error model coefficients of inertial grade sensors are from one to four orders of magnitude smaller than the fixed and first-order terms. Obtaining measurable quantities of these error sources requires the application of precise high-acceleration inputs from the laboratory test device. Accelerometer error terms have been obtained quite successfully since 1962, utilizing precision centrifuges that have the capability of applying precise acceleration over the range of 1 to 28 g's (i.e., 28 times the magnitude of the local-gravity vector). Gyros developed for platform stabilization systems are specifically designed for a very low angular-rate profile. Therefore, the centrifuge environment is not compatible with the gyro design, since a 10- to 20-arc-second misalignment of the gyro input-axis with respect to the centrifuge rotational plane can couple enough of the centrifuge angular rate into the gyro to completely mask the rate contribution of the desired error source terms and, in some instances, cause output saturation or destruction of the gyro bearing. Until 1971, there were no laboratory test devices that maintained a low angular-rate environment while providing precise high-acceleration inputs to

permit recovery of the high-order gyro compliance terms. In 1971, after a nine-year development, the United States Air Force completed the 260-inch radius precision centrifuge (Reference Figure 1.1), which is located at the Central Inertial Guidance Test Facility, Holloman Air Force Base, New Mexico [3]. The 260-inch centrifuge has the capability of testing both gyro and accelerometer inertial sensors, as well as complete navigational systems. The unique feature of this centrifuge, which permits high-g acceleration testing of gyros, is that the test specimen is on a counter-rotating platform (CRP), which isolates the gyros from the centrifuge angular rate, since the CRP rotates at the same rate but in opposition to the centrifuge main arm. Therefore, under perfect counter-rotation, the azimuth of the system under test remains fixed with respect to an earth reference frame. The acceleration applied to the system is a low frequency sinusoid with a zero to peak magnitude from 0.25 to 100 g's. The frequency of oscillation is less than 2 Hz and should be well within the system-gimbal-servo response so that there is no interference with the system stabilization function. The 260-inch centrifuge provides for the first time the precise high-g environment necessary to validate and accurately estimate for a complete navigational system the sensor error model coefficients proportional to acceleration. Unfortunately, accurate estimates of the error model coefficients require more than a precision test device. In addition to the test device, one must have (a) a positively controlled test procedure that varies the system orientation with respect to the input acceleration to provide better observation of the error coefficients

Reproduced from
best available copy.

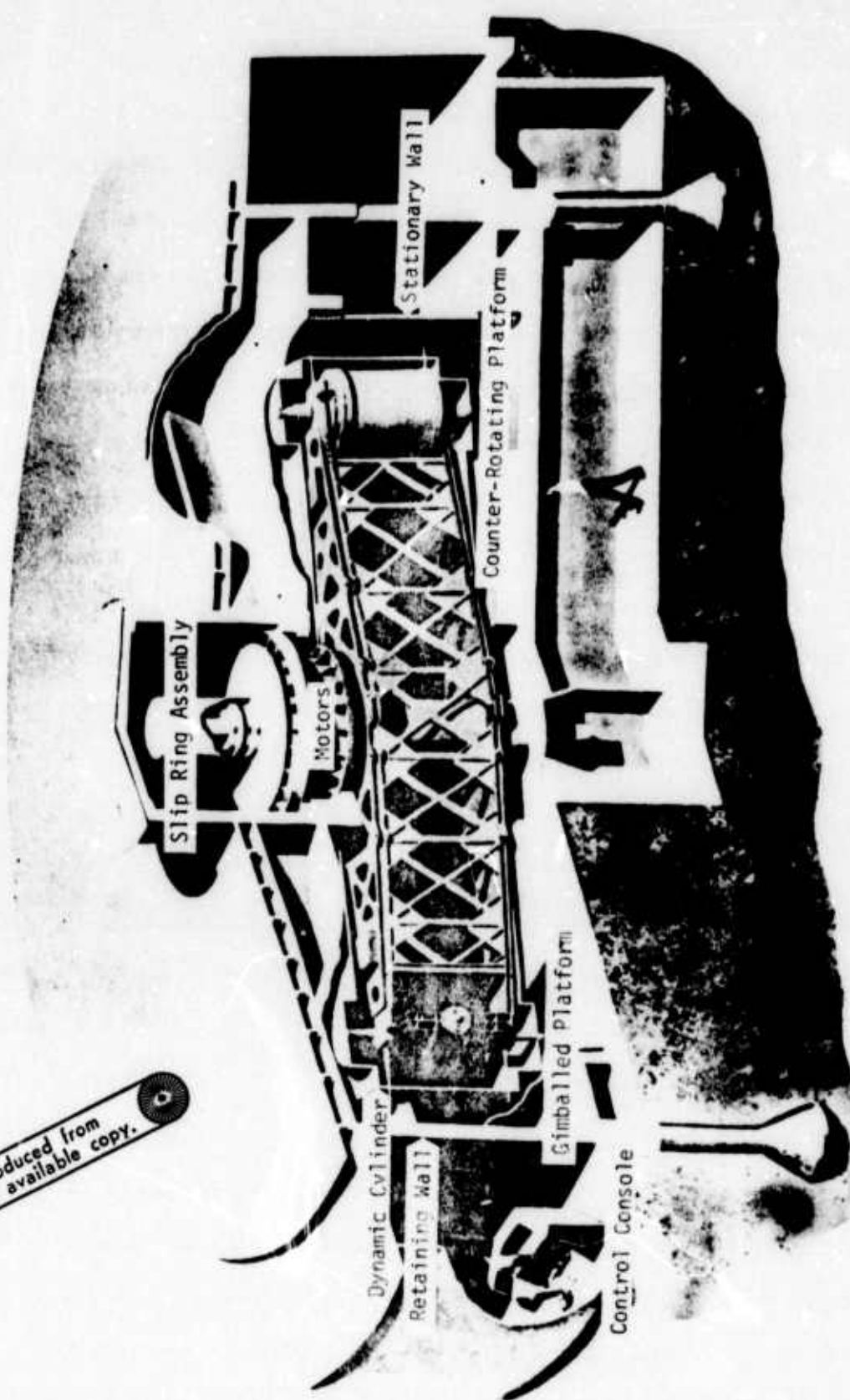


Figure 1.1. 260-Inch Radius Precision Centrifuge

in the measurement data; (b) a data collection scheme that does not corrupt the measurement data; and (c) a data reduction program that provides the "best" estimates of the error coefficients from noisy measurement data. The data processing problem is not considered in this report, since it is highly dependent on the particular system being tested and the data acquisition equipment available in the laboratory. The problem considered is to develop a dynamic test procedure and an associated data reduction method for obtaining estimates of the error model coefficients from a 260-inch centrifuge system test. The end product of the test program is to provide a dynamic laboratory calibration that identifies all the significant acceleration error sources of the Inertial Navigation System.

1.3 PROBLEM APPROACH

The stabilization function of an Inertial Navigation System provides base motion isolation of the inner gimbal or platform where the inertial sensors are located. Any angular motion of the base or mounting frame of the INS is transmitted through the outer system gimbals to the inner platform, where it is sensed by the triad of single-degree-of-freedom integrating gyros. The gyro outputs are sent to the gimbal stabilization loops, which consist of stabilization amplifiers driving gimbal torque motors. The end result is that, through rotation of the gimbals by the gimbal torque motors, the inner platform is driven in such a way as to null the gyro output signals so that the inner platform remains fixed with respect to inertial space or any other specified

navigational reference frame. The gyro output angular rate ω_O can be represented by the following performance model:

$$\begin{aligned} \omega_{Oi} = & (D_F + D_I a_I + D_O a_O + D_S a_S + D_{II} a_I^2 + D_{OO} a_O^2 + D_{SS} a_S^2 \\ & + D_{IO} a_I a_O + D_{IS} a_I a_S + D_{OS} a_O a_S) + \omega_I + \omega_{CMD} \end{aligned} \quad (1.1)$$

where

ω_{Oi} = output angular rate of the i th gyro

D_F = fixed restraint drift

D_I, D_O, D_S - mass unbalance drift coefficients

$D_{II}, D_{OO}, D_{SS}, D_{IO}, D_{IS}, D_{OS}$ - compliance drift coefficients

a_I, a_O, a_S - applied acceleration along the gyro input, output, and spin axes, respectively

ω_I = applied rate about the gyro input axis

ω_{CMD} = commanded angular rate due to command torque applied to gyro torque generator

Neglecting the commanded angular rate for now, the bracketed terms in Eq. (1.1) cause the inner platform to drift from the navigational reference frame, since they are not a function of input angular rate, but are generated by error sources internal to the gyro. In fact, these are the gyro error model coefficients that are to be identified.

Assuming that the applied rate about the gyro input axis is known, the angular motion of the platform with respect to the base mounting frame (which is equal in magnitude but opposite in direction to the gyro output angular rate) will be a function of the gyro error model coefficients and the applied acceleration. The applied acceleration for a 260-inch centrifuge test will be a combination of the local gravitational and kinematic accelerations. Tracking the platform motion with respect to a mounting frame, located on the counter-rotating platform of the centrifuge, provides the basis for the dynamics of the system calibration problem. The platform 3-degrees-of-freedom motion can be described in terms of three Euler angle rates. Numerous laboratory tests of inertial sensors have shown that the actual physical system error coefficients are best described by a stochastic process whose behavior at any given time is adequately described by a Gaussian distribution [4, 5, 6]. Therefore, the problem is an identification or parameter estimation problem, where the Euler angles and error model coefficients are designated as system state variables to be estimated from noisy measurements. Before discussing the measurement dynamics, it should be noted that the accelerations in Eq. (1.1) are defined in the sensor frame that is fixed to the inner platform; therefore, the accelerations will be functions of the Euler angle states. Therefore, the evolution of the system's state with time will be a nonlinear function of the state variables. One of the INS outputs is usually the integral of the accelerations sensed by the triad of accelerometers mounted on the inner platform. Since the system output interfaces with an airborne digital computer, the velocity is quantized into velocity

pulses that are counted over some measurement interval. The output is therefore the velocity change over the sample interval. This implies that the measurement dynamic equations are discrete-time processes. The relationship between the system dynamics and the measurement sequence can be seen from the following model of an accelerometer output.

$$a_{\text{IND}}^i = K_0 + K_1 a_I + K_2 a_I^2 + K_3 a_I^3 + K_{\text{IP}} a_I a_P \quad (1.2)$$

where

a_{IND}^i = indicated output of the i th accelerometer

K_0 = bias

K_1 = scale factor

K_2, K_3 - nonlinear coefficients

K_{IP} = cross-axis nonlinearity

a_I, a_P - applied acceleration along the accelerometer input and pendulous axes, respectively

The K -terms are the accelerometer error model coefficients to be identified; therefore, they will be designated as state variables. The definition of the accelerations in Eq. (1.2) in the sensor frame implies that they will be functions of the Euler angle states. This in turn implies the following properties for the measurement sequence: (a) the measurement dynamics will be a nonlinear function of the state variables, and (b) since the Euler angles depict the platform position at

any point in time, the Euler angle states in the measurement sequence contain the dynamic motion generated by the gyro error coefficient states. Adequately representing all the error coefficient states in the measurement sequence implies that the platform motion must be positively controlled to orient each sensor axis with respect to the applied acceleration. If the platform motion is limited to the benign motion of the random drift plus earth rate, an observability problem could occur with some of the error states. To overcome this problem, one must use the ω_{CMD} term in Eq. (1.1) to drive the platform through a prespecified torque profile so that each axis of the platform is subjected to the applied acceleration. The commanded gyro output is generated by applying a prespecified signal to the internal gyro torque generator. This dynamic test procedure permits complete rotational control of the platform so that adequate representation of the contribution due to each error state can be obtained in the measurement sequence. Since both the state and measurement dynamics are nonlinear functions of the state variables, an extended Kalman filter will be applied to linearize the state and measurement trajectories about the optimal filtered estimates.

This dynamic test procedure, in conjunction with the filtering process, will provide, for the first time at the Central Inertial Guidance Test Facility, the capability of on-line system calibrations. The advantage of on-line data reduction is that the test procedure, the assumed system models, and the significance of the state estimates can be evaluated while the system is under test.

1.4 SCOPE OF EFFORT

The scope of the report is as follows:

- (a) Development of the system and measurement dynamic equations for a complete Inertial Navigation System Centrifuge Test Program. This task includes the inertial sensor error model equations, the platform rate equations, the kinematic and gravitational acceleration equations with the corresponding centrifuge coordinate transformations, and finally the Euler rate equations for tracking the platform motion.
- (b) Development of the extended Kalman filter equations.
- (c) Evaluation of the data reduction technique via the following simulations:
 - (1) The normal centrifuge test program consists of a 1-g calibration in the local gravitational field prior to and immediately following the operating centrifuge test. The purpose of this test is to determine the overall effect of the centrifuge environment on the fixed and first-order error coefficients, which are the major error sources. A simulation of the 1-g calibration program, consisting of 17 state variables, was made, using the same techniques proposed for the operating centrifuge test.
 - (2) A 10-state variable simulation was made of the centrifuge operating at the 10-g level to determine the ability of the filter to identify the higher-order error coefficients.

So that the error model coefficients in these simulations are representative of an actual physical system, the Carousel VB Inertial Measurement Unit developed by Delco Electronics was selected as the baseline Inertial Navigation System, since it is representative of the type of Inertial Guidance System being used in both ballistic missile and aircraft navigation applications. The United States Air Force selected the Carousel VB for use in their Titan IIC series of launch vehicles. The Carousel IV, which is similar to the Model VB, is presently installed in the Boeing Models 747 and 707, and McDonnell Douglas Models DC-8 and DC-10 aircraft.

SECTION 2

SENSOR AND PLATFORM PERFORMANCE MODELS

The performance models of the gyro, the accelerometer, and the system platform motion are developed in this section. The models contain the error terms whose coefficients are to be identified during the centrifuge tests. The error source terms are limited to those associated with an acceleration environment. Error terms generated by angular rate are neglected, since it is assumed that the angular rate environment is limited to the benign motion of the platform with respect to inertial space. Instances where this assumption could be invalid will be mentioned in Section 3 with the understanding that the performance models of this section must be expanded to include those error terms proportional to angular rate that contribute significant error.

2.1 VECTOR AND MATRIX NOTATION

Since both vector and matrix equations will be used throughout the report, a standardized notation will be used to distinguish between a physical vector and a mathematical vector. A physical vector will represent some physical quantity that has both magnitude and direction associated with it; however, its existence in space will be independent of any coordinate frame. Since physical vectors will be used in the application of the theorem of Coriolis, it will be necessary to indicate the reference frame in which a vector derivative is being taken. The notation for a physical vector will be an underlined variable. Subscripts will indicate the relative variables for which the

physical quantity is measured, and superscripts will indicate the reference frame in which a vector derivative is being taken. For example,

$\underline{\omega}_{ib}$ = the physical angular velocity of the b frame relative to the i frame

$\dot{\underline{R}}_{ie}^k$ = the physical vector velocity of the e frame with respect to the i frame as viewed from the reference frame k (i.e., the derivative is taken in the k frame)

A mathematical vector is associated with the three numbers or coordinates that are the components of the physical vector relative to some coordinate frame. The three coordinates representing the physical vector form a 3×1 column matrix that will be referred to as the mathematical vector. The notation for a mathematical vector will be a variable that is not underlined. Subscripts will indicate the relative variables for which the physical quantity is measured, and superscripts will indicate the reference frame in which the vector is coordinatized. For example,

$$\omega_{ib}^b = \begin{bmatrix} \omega_I \\ \omega_O \\ \omega_S \end{bmatrix} \triangleq \{ \omega_I, \omega_O, \omega_S \}$$

$$\dot{R}_{ie}^k = \begin{bmatrix} \dot{r}_x \\ \dot{r}_y \\ \dot{r}_z \end{bmatrix} \triangleq \{ \dot{r}_x, \dot{r}_y, \dot{r}_z \}$$

where ω_{ib} is coordinatized in the b frame and \dot{R}_{ie} is coordinatized in the k frame. The braced array $\{ \}$ is introduced to save space in the written text; it should not be confused with a row matrix.

Two other notations will be used throughout the text. The first is a direction cosine matrix, C_b^i , which transforms a column matrix from frame b to frame i. For example,

$$C_b^i R^b = \begin{bmatrix} c_{11} & c_{12} & c_{13} \\ c_{21} & c_{22} & c_{23} \\ c_{31} & c_{32} & c_{33} \end{bmatrix} \begin{bmatrix} r_x \\ r_y \\ r_z \end{bmatrix}$$

where c_{jk} is the direction cosine between the jth axis in the i frame and the kth axis in the b frame. The second notation is the skew-symmetric, cross-product matrix. It is the matrix form of the vector cross product [i.e., it represents the $(\underline{\omega}_{ie} \times)$ portion of the vector cross product $\underline{\omega}_{ie} \times \underline{R}$] and will be designated as follows:

$$W_{ie}^{ek} \triangleq \begin{bmatrix} 0 & -\omega_Z & \omega_Y \\ \omega_Z & 0 & -\omega_X \\ -\omega_Y & \omega_X & 0 \end{bmatrix}$$

where the first superscript e designates the reference frame in which the matrix elements are coordinatized, and the second superscript designates by the letter k that the quantity represented is by definition the 3×3 , skew-symmetric, cross-product matrix.

2.2 GYRO PERFORMANCE MODEL

Greenwood [7] shows that, from Newton's basic law of rotational motion, the following vector equation is obtained:

$$\dot{\underline{H}} = \underline{M} \quad (2.1)$$

where $\dot{\underline{H}}$ is the vector time rate of change of the angular momentum of a particle about a fixed point, which is equal to the vector moment \underline{M} of the total external force applied to the particle about the same fixed point. Equation (2.1) can be applied to a gyro to describe the dynamic motion of the gyro element, if some simplifying assumptions are made concerning the gyro element [8]. The gyro element consists of a spinning rotor, a drive mechanism for the rotor, and the supporting gimbal structure as shown in Figure 2.1. The gyro element is assumed to have the following simplifying properties that are valid for practical applications:

- (a) The rotor spins at a constant speed about an axis of symmetry.
- (b) The center of mass of the rotor coincides with that of the gyro element.
- (c) The gyro rotor and gimbal support structure are rigid.

Applying Eq. (2.1) to the gyro element gives

$$\dot{\underline{H}}_{i,ge}^i = \underline{M} \quad (2.2)$$

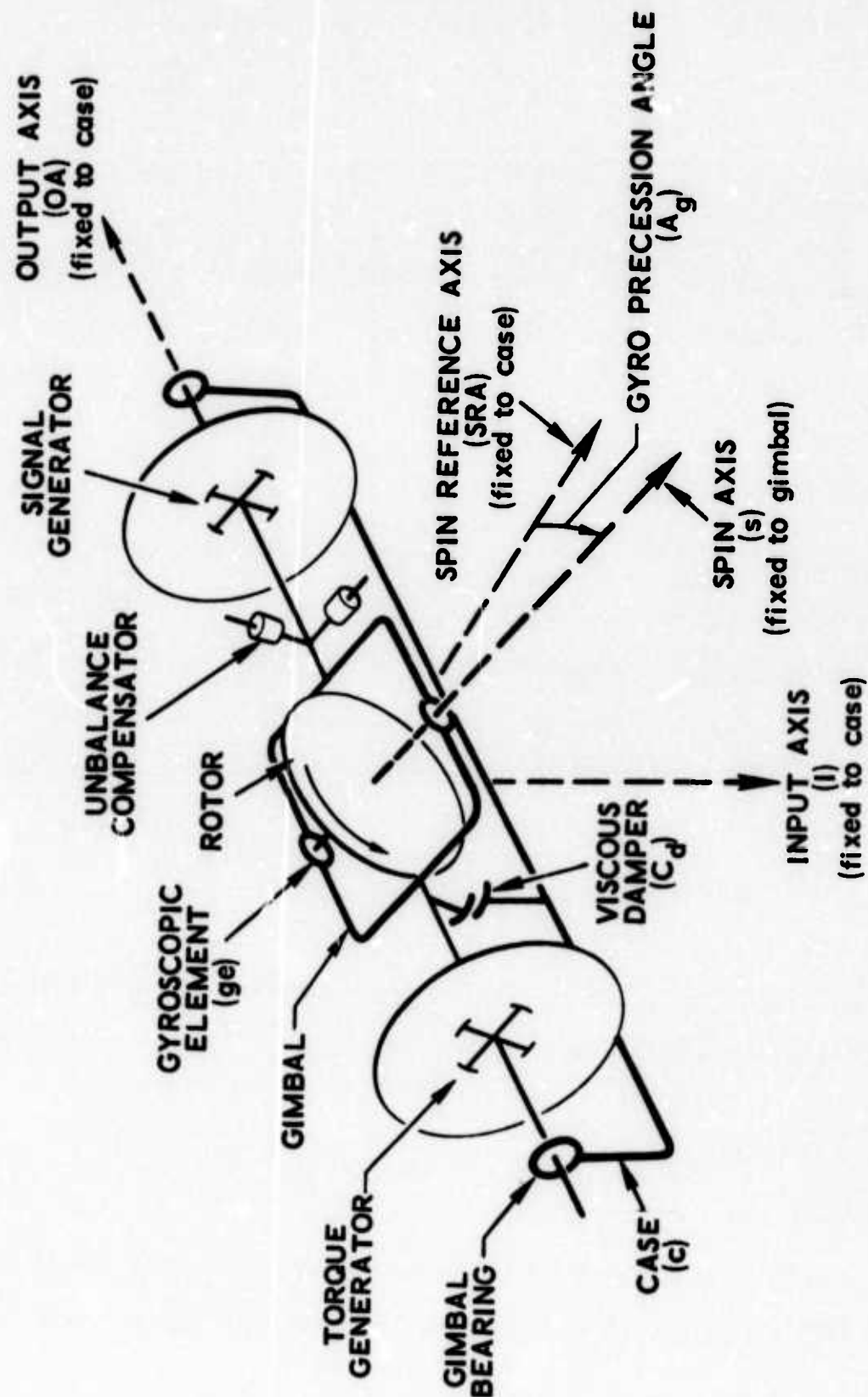


Figure 2.1. Line Schematic of a Single-Degree-of-Freedom Integrating Gyro

where

$\dot{\underline{H}}_{i,ge}^i$ = time rate of change of angular momentum of the gyro element ge, with respect to the inertial reference frame i, as viewed from the inertial frame

\underline{M} = torque applied about the center of mass of the gyro element

Applying the first equation of Coriolis [Reference Eq. (A.3) in Appendix A] to the left-hand side of Eq. (2.2) gives

$$\dot{\underline{H}}_{i,ge}^i = \dot{\underline{H}}_{i,ge}^{ge} + \underline{\omega}_{i,ge} \times \underline{H}_{i,ge} \quad (2.3)$$

The angular momentum vector of the gyro element, $\underline{H}_{i,ge}$, is equal to the vector sum of the spin angular momentum vector of the rotor, \underline{H}_s , and the nonspin angular momentum of the gyro element, \underline{H}_{ns} . Substituting this vector sum into the right-hand side of Eq. (2.3) and using the equality of Eq. (2.2) gives

$$\underline{M} = \dot{\underline{H}}_s^{ge} + \dot{\underline{H}}_{ns}^{ge} + \underline{\omega}_{i,ge} \times \underline{H}_s + \underline{\omega}_{i,ge} \times \underline{H}_{ns} \quad (2.4)$$

The rotor speed is assumed constant, implying that $\dot{\underline{H}}_s^{ge} \equiv 0$; therefore, Eq. (2.4) reduces to

$$\underline{M} = \dot{\underline{H}}_{ns}^{ge} + \underline{\omega}_{i,ge} \times \underline{H}_s + \underline{\omega}_{i,ge} \times \underline{H}_{ns} \quad (2.5)$$

Equation (2.5) is the basic law of motion of the gyroscopic element.

The $\dot{\underline{H}}_{ns}^{ge}$ term is the source of the characteristic dynamics or

transient response of the gyro element. The vector cross-product terms contribute to the gyro's steady-state behavior.

Since most Inertial Navigation Systems employ single-degree-of-freedom integrating (SDFI) gyros [9], an equation describing the motion or precession of the gyro element with respect to a gyro case axis frame will be developed for a SDFI gyro. Expressing Eq. (2.5) in a matrix form such that the applied torque is coordinatized in the case or c frame, as shown in Figure 2.1, gives the following matrix equation for the gyro element motion:

$$M^c = C_{ge}^c \dot{H}_{ns}^{ge} + W_{ic}^{ck} C_{ge}^c H_s^{ge} + W_{ic}^{ck} C_{ge}^c H_{ns}^{ge} \quad (2.6)$$

where

C_{ge}^c = the gyro element to case transformation matrix

\dot{H}_{ns}^{ge} = time rate of change of nonspin angular momentum matrix coordinatized in the moving gyro element frame

W_{ic}^{ck} = skew-symmetric, cross-product matrix of the angular velocity of the case frame relative to inertial space, coordinatized in the case reference frame

H_s^{ge} , H_{ns}^{ge} - are the spin and nonspin angular momentum matrices, respectively, both coordinatized in the ge frame

Since the gyro element motion of a SDFI gyro is constrained to precession about the output axis, an expression for the output axis torque, M_{OA} , will be obtained from Eq. (2.6). The gyro precession angle about the output axis (shown as A_g in Figure 2.1) is maintained well

below five arc-minutes by the platform stabilization loop. Therefore a small-angle transformation can be assumed for the gyro element to case transformation.

$$C_{ge}^c = \begin{bmatrix} 1 & 0 & A_g \\ 0 & 1 & 0 \\ -A_g & 0 & 1 \end{bmatrix} \quad (2.7)$$

Define

$$M^c = \{M_I, M_{OA}, M_{SRA}\} \quad (2.8)$$

$$\omega_{ic}^c = \{\omega_I, \omega_{OA}, \omega_{SRA}\}$$

Therefore, by the definition of the cross-product matrix

$$W_{ic}^{ck} = \begin{bmatrix} 0 & -\omega_{SRA} & \omega_{OA} \\ \omega_{SRA} & 0 & -\omega_I \\ -\omega_{OA} & \omega_I & 0 \end{bmatrix} \quad (2.9)$$

Now

$$H_s^{ge} = \{0, 0, H_s\}$$

$$\omega_{i,ge}^{ge} = \{\omega_x, \omega_y, \omega_z\} \quad (2.10)$$

$$H_{ns}^{ge} = \{I_x \omega_x, I_y \omega_y, I_z \omega_z\}$$

where

I_x, I_y, I_z - are the principal moments of inertia about the ge axes

An expression for obtaining the angular velocities of the ge frame is

$$\omega_{i,ge}^{ge} = C_{ic}^{ge} \omega_{ic}^c + \omega_{c,ge}^{ge} \quad (2.11)$$

where

$$\omega_{c,ge}^{ge} = \{0, \dot{A}_g, 0\} \quad (\text{Reference Figure 2.1})$$

$$C_{ic}^{ge} \triangleq [C_{ge}^c]^{-1} = [C_{ge}^c]^T$$

C_{ge}^c is a direction-cosine matrix, implying that it is an orthogonal matrix [7]; therefore, its inverse is equal to its transpose. Substituting the appropriate matrices from Eqs. (2.7), (2.8), and (2.10) into Eq. (2.11) gives the following set of equations for the ge frame angular velocities:

$$\omega_x = \omega_I - A_g \omega_{SRA}$$

$$\omega_y = \omega_{OA} + \dot{A}_g \quad (2.12)$$

$$\omega_z = \omega_{SRA} + A_g \omega_I$$

Therefore, from Eq. (2.10),

$$H_{ns}^{ge} = \begin{bmatrix} I_x (\omega_I - A_g \omega_{SRA}) \\ I_y (\omega_{OA} + \dot{A}_g) \\ I_z (\omega_{SRA} + A_g \omega_I) \end{bmatrix} \quad (2.13)$$

and the transient response is represented by

$$\dot{H}_{ns}^{ge} = \begin{bmatrix} I_x (\dot{\omega}_I - \dot{A}_g \omega_{SRA} - A_g \dot{\omega}_{SRA}) \\ I_y (\dot{\omega}_{OA} + \ddot{A}_g) \\ I_z (\dot{\omega}_{SRA} + \dot{A}_g \omega_I + A_g \dot{\omega}_I) \end{bmatrix} \quad (2.14)$$

Equations (2.7) through (2.14) define all the terms of Eq. (2.6) to permit a solution for the output axis torque.

$$\begin{aligned} M_{OA} = & I_y \dot{\omega}_{OA} + I_y \ddot{A}_g - H_s \omega_I + H_s \omega_{SRA} A_g \\ & - (I_z - I_x) \omega_I \omega_{SRA} - A_g (\omega_I^2 - \omega_{SRA}^2) (I_z - I_x) \end{aligned} \quad (2.15)$$

The output axis torque M_{OA} and the time constant τ_g for a SDFI gyro are, by the design characteristics of the gyro, equal to the following:

$$\begin{aligned} M_{OA} &= M_{tg} - C_d \dot{A}_g + (u) M \\ \tau_g &= I_y / C_d \end{aligned} \quad (2.16)$$

where

M_{tg} = torque applied by the gyro torque generator

C_d = viscous damping torque coefficient

$(u)M$ = uncertainty torque caused by internal gyro error sources

Substituting Eq. (2.16) into Eq. (2.15) and rearranging the terms gives the dynamic equation of motion for a SDFI gyro.

$$\begin{aligned} \tau_g \ddot{A}_g + \dot{A}_g &= \frac{H_s}{C_d} \omega_I + \frac{M_{tg}}{C_d} + \frac{(u)M}{C_d} - \frac{H_s}{C_d} \omega_{SRA} A_g - \tau_g \dot{\omega}_{OA} \\ &+ \frac{(I_z - I_x)}{C_d} \omega_I \omega_{SRA} + \frac{A_g}{C_d} (\omega_I^2 - \omega_{SRA}^2) (I_z - I_x) \end{aligned} \quad (2.17)$$

Except for the first three terms, all the remaining terms on the right-hand side of Eq. (2.17) are undesirable cross-coupling terms. The significance of these terms should be evaluated using the specific design characteristics of the SDFI gyro in conjunction with the expected values of the external parameters generated by the operating environment. Gyro operation in a platform mode involves the rotational stabilization of the gimballed platform upon which the gyros are mounted. If the platform is stabilized in the inertial frame of reference, then the last four terms of the right-hand side of Eq. (2.17) can be neglected, since an inertial frame mechanization subjects the gyros to the most benign rotational environment possible. In addition, the time constant, τ_g , of a platform type gyro is made very small by decreasing the output

axis moment of inertia I_y and increasing the viscous damping coefficient C_d . Making the time constant small minimizes the effects of the transient response terms ($\tau_g \ddot{A}_g$ and $\tau_g \dot{\omega}_{OA}$) on the loop performance. Those terms involving the product of the output precession angle A_g are further reduced, since the high-gain platform stabilization loop maintains A_g essentially at null (less than one arc-minute).

As discussed in Section 1.3, the platform calibration program employs a dynamic test procedure in which the gyros are command torqued to drive the platform through a prespecified rotational profile. This implies that an inertially rotating reference frame is being instrumented during the test program; therefore, the effects due to the cross-coupling terms must be evaluated to determine if any of the last four terms should be included in the final version of the gyro performance model. Rewriting Eq. (2.17) in an alternate form yields:

$$\begin{aligned} \frac{C_d}{H_s} \tau_g \ddot{A}_g + \omega_O = \omega_I + \omega_{CML} + (u)\omega_D - \omega_{SRA} A_g - \frac{C_d}{H_s} \tau_g \dot{\omega}_{OA} \\ + \frac{(I_z - I_x)}{H_s} \omega_I \omega_{SRA} + \frac{A_g}{H_s} (\omega_I^2 - \omega_{SRA}^2) (I_z - I_x) \end{aligned} \quad (2.18)$$

where

$$\omega_O = \frac{C_d}{H_s} \dot{A}_g = \text{output angular rate of the gyro}$$

$$\omega_I = \text{applied rate about the gyro input axis}$$

$$\omega_{CMD} = \frac{M_{tg}}{H_s} = \text{commanded angular rate}$$

$$(u)\omega_D = \frac{(u)M}{H_s} = \text{error drift generated by internal gyro error sources}$$

A comparison of the magnitude of the cross-coupling terms versus the first three terms on the right-hand side of Eq. (2.18) is given below. The given parameters are based on the design characteristics of the Carousel VB Inertial Measurement Unit SDFI gyros [10], and the angular rate and acceleration values are from a computer simulation of the platform rotational profile that was generated in support of the data reduction evaluation described in Section 1.4. Given:

$$A_g = 1 \text{ arc-minute}$$

$$C_d = 62,500 \text{ gm-cm}^2/\text{sec}$$

$$H_s = 1 \times 10^5 \text{ gm-cm}^2/\text{sec}$$

$$\tau_g = 2 \text{ milliseconds}$$

$$\omega_I = 5.4 \times 10^{-4} \text{ rad/sec}$$

$$\omega_{SRA} = 5 \times 10^{-4} \text{ rad/sec}$$

$$\dot{\omega}_{OA} = 3.2 \times 10^{-8} \text{ rad/sec}^2$$

$$I_z - I_x = 10 \text{ gm-cm}^2$$

The magnitudes of the terms in Eq. (2.18) are:

$$\omega_I + \omega_{CMD} + (u)\omega_D = 6.0 \times 10^{-4} \text{ rad/sec}$$

$$\omega_{SRA} A_g = 14.5 \times 10^{-8} \text{ rad/sec}$$

$$\frac{C_d}{H_s} \tau_g \dot{\omega}_{OA} = 4.0 \times 10^{-11} \text{ rad/sec}$$

$$\frac{(I_z - I_x)}{H_s} \omega_I \omega_{SRA} = 2.7 \times 10^{-11} \text{ rad/sec}$$

$$\frac{A_g}{H_s} (\omega_I^2 - \omega_{SRA}^2) (I_z - I_x) = 1.2 \times 10^{-15} \text{ rad/sec}$$

A comparison shows that the cross-coupling terms can be neglected.

Since τ_g is small, the transient response can also be neglected; therefore, Eq. (2.18) reduces to the following steady-state equation:

$$\omega_O = \omega_I + \omega_{CMD} + (u) \omega_D \quad (2.19)$$

As was shown in Eq. (1.1) of Chapter 1, the error drift term, $(u)\omega_D$, is equal to the sum of the drift-producing error sources internal to the gyro. Therefore, from Eq. (1.1), the gyro performance model equation is

$$\begin{aligned} \omega_O = & (D_F + D_I a_I + D_O a_O + D_S a_S + D_{II} a_I^2 + D_{OO} a_O^2 + D_{SS} a_S^2 \\ & + D_{IO} a_I a_O + D_{IS} a_I a_S + D_{OS} a_O a_S) + \omega_I + \omega_{CMD} \end{aligned} \quad (2.20)$$

As previously mentioned, the gyro error sources considered are limited to those normally found when subjecting the gyro to an acceleration environment. The error term expansion in Eq. (2.20) contains those terms that have been found, by numerous tests conducted at the Central Inertial Guidance Test Facility, to be the predominant sources

of error. Wrigley [8], Taylor [11], and Lorenzini [12] have excellent descriptions of the physical properties in the gyro that generate the error drifts.

2.3 ACCELEROMETER PERFORMANCE MODEL

The accelerometer considered in this study is a force-rebalance pendulous type device, which can be represented in the simplified form of Figure 2.2. Based on the behavior of a simple pendulum under the influence of pivot acceleration, the acceleration force acting on the center of gravity of the pendulum will cause the pendulum to accelerate in the direction of the force and, in addition, cause a moment to be applied about the pivot, which imparts an angular acceleration to the pendulum. The rotation of the pendulum about the pivot is represented by the angle about the output axis A_O in Figure 2.2. The force-rebalance feature of the accelerometer is normally feedback current flowing through a forcer coil, which is mounted on the pendulous element, reacting with a permanent magnet to drive the pendulum back to its null position. With an acceleration applied to the input axis, the moment about the output axis, M_{OA} , is as follows:

$$M_{OA} = F_a l_y = m a_I l_y = m a_I l \cos A_O \quad (2.21)$$

where

F_a = acceleration force

a_I = acceleration applied to the input axis

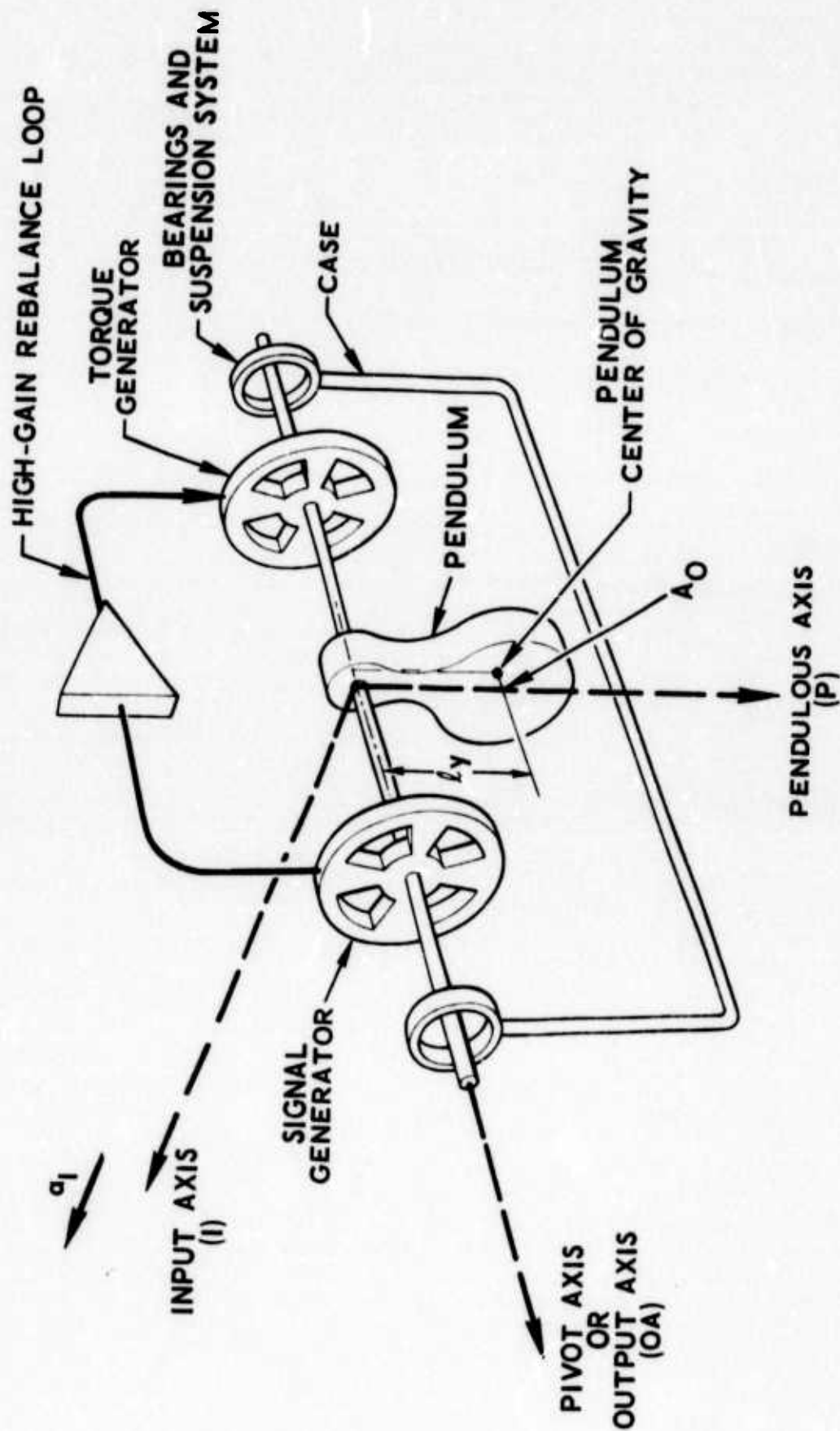


Figure 2.2. Line Schematic of a Force-Rebalance Pendulous Accelerometer

l = length of the pendulum of mass m

$l_y = l \cos A_O$ = effective length of the pendulum with respect to F_a

Based on the design characteristics of a force-rebalance accelerometer, M_{OA} is also represented by:

$$M_{OA} = I_P \ddot{A}_O + C_d \dot{A}_O + k A_O - (u)M \quad (2.22)$$

where

I_P = moment of inertia of the pendulum about the pivot or output axis

C_d = viscous damping coefficient

k = spring or elastance coefficient of the pivot hinge

$(u)M$ = uncertainty torque due to internal error sources of the accelerometer

Because of the high-gain rebalance loop, A_O is maintained essentially at null. Therefore, using a small angle approximation for A_O (i.e., $\cos A_O \approx 1$) and equating Eqs. (2.21) and (2.22) gives

$$\frac{I_P}{k} \ddot{A}_O + \frac{C_d}{k} \dot{A}_O + A_O = \frac{n \cdot l}{k} a_I + \frac{(u)M}{k} \quad (2.23)$$

Comparing the left-hand side of Eq. (2.23) with the standard form of a second-order transient solution

$$\frac{\ddot{A}_O}{\omega_n^2} + \frac{2\zeta}{\omega_n} \dot{A}_O + A_O$$

shows that

$$\omega_n = \sqrt{k/I_P} = \text{undamped natural frequency}$$

$$\zeta = \frac{C_d}{2\sqrt{k I_P}} = \text{damping ratio}$$

and therefore the accelerometer time constant, τ_a , is

$$\tau_a = \frac{1}{\zeta \omega_n} = \frac{2 I_P}{C_d}$$

Typical values are: $I_P = 7.06 \text{ gm-cm}^2$ and $C_d = 47,000 \text{ gm-cm}^2/\text{sec}$, which gives a value of 0.3 milliseconds for τ_a . Neglecting the transient response gives the following steady-state equation:

$$a_{\text{IND}} = a_I + (u)a \quad (2.24)$$

where

$$a_{\text{IND}} = \frac{k}{mI} A_O = \text{indicated output of the accelerometer}$$

$$(u)a = \frac{(u)M}{mI} = \text{uncertainty in acceleration due to internal error sources}$$

Reference Eq. (1.2); the uncertainty term, $(u)a$, is equal to the sum of the acceleration error sources:

$$(u)a = K_O + (u)K_1 a_I + K_2 a_I^2 + K_3 a_I^3 + K_{IP} a_I a_P \quad (2.25)$$

Substituting Eq. (2.25) into Eq. (2.24) gives the accelerometer performance model equation:

$$a_{IND} = K_O + K_1 a_I + K_2 a_I^2 + K_3 a_I^3 + K_{IP} a_I a_P \quad (2.26)$$

where

$$K_1 = (1 + (u)K_1)$$

$$(u)K_1 = \text{uncertainty in the accelerometer scale factor}$$

As was the case with the gyro performance model, the accelerometer error sources considered are limited to those normally found when the accelerometer is subjected to an acceleration environment. The cross-axis term $K_{IP} a_I a_P$ is to account for the case where an acceleration applied along the pendulous axis causes an additional moment about the pivot; the additional moment occurs because of the moment-arm generated by the offset of the pendulum, which was caused by the simultaneous application of a_I along the input axis. Obviously, the cross-axis contribution is small since the offset of the pendulum is the angle A_O , which is maintained very small to prevent the coupling effect.

2.4 PLATFORM PERFORMANCE MODELS

Based on the discussion in Section 1.3, one may derive two requirements for platform performance information. The first requirement is to obtain an expression of the platform rate with respect to some laboratory reference frame, in order to establish the system dynamic equations, which track the platform motion. The second requirement is to obtain an expression for the output of the platform accelerometers, which formulates the measurement dynamics and provides the basis for the measurement sequence.

The platform provides the stabilization or base motion isolation function, implying that a vector representation of the platform rate is essentially equal in magnitude but opposite in direction to the gyro output angular rate, ω_O .

$$\underline{\omega}_{rp} = -\underline{\omega}_O + \underline{\delta \omega}_{SERVO} \quad (2.27)$$

where

$\underline{\omega}_{rp}$ = angular rate of the platform frame p with respect to the platform base or mounting fixture frame r, which is the selected laboratory reference frame

$\underline{\delta \omega}_{SERVO}$ = uncertainty in platform rate due to the stabilization loop servo error

From Eq. (2.19), Eq. (2.27) is also equal to

$$\underline{\omega}_{rp} = -\underline{\omega}_I - \underline{\omega}_{CMD} - \underline{(u)\omega}_D + \underline{\delta \omega}_{SERVO} \quad (2.28)$$

A matrix equation of the platform rate coordinatized in the platform reference frame requires a clear understanding of the vectors given on the right-hand side of Eq. (2.28). ω_I is the angular rate sensed by the gyro about its input axis. The motion sensed by the gyro is identical to the motion of the inner gimbal platform where the gyro is mounted. However, the motion of the inner gimbal is identical to the motion of the system platform base or mounting fixture, since the outer gimbals of the system platform transmit the base motion directly to the inner gimbal. Therefore, the angular rate sensed by the gyro is identical to the angular rate of the base with respect to inertial space, ω_{ir} . So, coordinatizing ω_I in the base frame r gives the following matrix equation for the applied rate about the gyro input axis.

$$\omega_I^r = \omega_{ir}^r \quad (2.29)$$

The commanded angular rate, ω_{CMD} , and the error drift rate, $(u)\omega_D$, are both generated by sources internal to the gyro. They represent motion of the gyro element with respect to the gyro case as generated by command and uncertainty torquing. The gyro element axes, shown in Figure 2.1, will be defined as the gyro sensor axis frame s . The gyro case input axis will be considered identical to the direction of the inner gimbal platform axis for that gyro. In other words, the X, Y, and Z gyro case input axes establish the direction of the x, y, and z inner gimbal platform axes which will be known as the p frame.

Therefore, the matrix equations for the command angular rate and the error drift rate, both coordinatized in the p frame, are:

$$\begin{aligned}\omega_{\text{CMD}}^{\text{p}} &= C_s^{\text{p}} \omega_{\text{CMD}}^{\text{s}} \\ \omega_{\text{D}}^{\text{p}} &= C_s^{\text{p}} \omega_{\text{D}}^{\text{s}}\end{aligned}\tag{2.30}$$

where

$\omega_{\text{CMD}}^{\text{s}}$ = a matrix of commanded angular rates in the sensor frame

$\omega_{\text{D}}^{\text{s}}$ = a matrix of error drift rates in the sensor frame

C_s^{p} = transformation matrix from the sensor frame to the platform frame

Combining Eqs. (2.28) through (2.30) gives the matrix equation for the platform rate in the platform frame as

$$\omega_{\text{rp}}^{\text{p}} = \begin{bmatrix} \omega_{\text{xp}} \\ \omega_{\text{yp}} \\ \omega_{\text{zp}} \end{bmatrix} = - C_s^{\text{p}} \left[\omega_{\text{CMD}}^{\text{s}} + \omega_{\text{D}}^{\text{s}} \right] - C_r^{\text{p}} \omega_{\text{ir}}^{\text{r}} + \omega_{\text{SERVO}}^{\text{p}}\tag{2.31}$$

The first matrix expression on the right-hand side of Eq. (2.31) actually represents the combined contribution of the X, Y, and Z gyros. Therefore, Eq. (2.31) can be rewritten as

$$\begin{bmatrix} \omega_{xp} \\ \omega_{yp} \\ \omega_{zp} \end{bmatrix} = - C_{SGX}^p \left[\omega_{CMD}^{SGX} + \omega_D^{SGX} \right] - C_{SGY}^p \left[\omega_{CMD}^{SGY} + \omega_D^{SGY} \right] \\ - C_{SGZ}^p \left[\omega_{CMD}^{SGZ} + \omega_D^{SGZ} \right] - C_r^p \omega_{ir}^r + \omega_{SERVO}^p \quad (2.32)$$

C_{SGj}^p ($j = X, Y, Z$) are the coordinate transformations from the gyro sensor axes to the platform frame. These transformations will be defined in Section 3. C_r^p is the transformation from the platform base to the inner platform p frame and will be defined in Section 4. Equation (2.20) represents the performance model for all three gyros; therefore, Eq. (2.32) can be expanded to incorporate all the terms from Eq. (2.20) for each gyro. The final form of the platform rate performance model matrix equation is:

$$\begin{bmatrix} \omega_{xp} \\ \omega_{yp} \\ \omega_{zp} \end{bmatrix} = - C_{SGX}^p \left\{ \begin{bmatrix} D_{FX} \\ 0 \\ 0 \end{bmatrix} + \begin{bmatrix} D_{IX} & D_{OX} & D_{SX} \\ 0 & 0 & 0 \\ 0 & 0 & 0 \end{bmatrix} \begin{bmatrix} a_{IX} \\ a_{OX} \\ a_{SX} \end{bmatrix} \right. \\ + \begin{bmatrix} D_{IIX} & D_{OOX} & D_{SSX} \\ 0 & 0 & 0 \\ 0 & 0 & 0 \end{bmatrix} \begin{bmatrix} a_{IX}^2 \\ a_{OX}^2 \\ a_{SX}^2 \end{bmatrix} \\ \left. + \begin{bmatrix} D_{IOX} & D_{ISX} & D_{OSX} \\ 0 & 0 & 0 \\ 0 & 0 & 0 \end{bmatrix} \begin{bmatrix} a_{IX} & a_{OX} \\ a_{IX} & a_{SX} \\ a_{OX} & a_{SX} \end{bmatrix} \right\} \quad (2.33)$$

$$\begin{aligned}
& + \begin{bmatrix} \text{TSF}_X & 0 & 0 \\ 0 & 0 & 0 \\ 0 & 0 & 0 \end{bmatrix} \begin{bmatrix} t_{gX} \\ 0 \\ 0 \end{bmatrix} \Bigg\} - C_{SGY}^p \begin{bmatrix} D_{FY} \\ 0 \\ 0 \end{bmatrix} \\
& + \begin{bmatrix} D_{IY} & D_{OY} & D_{SY} \\ 0 & 0 & 0 \\ 0 & 0 & 0 \end{bmatrix} \begin{bmatrix} a_{IY} \\ a_{OY} \\ a_{SY} \end{bmatrix} + \begin{bmatrix} D_{IYY} & D_{OOY} & D_{SSY} \\ 0 & 0 & 0 \\ 0 & 0 & 0 \end{bmatrix} \begin{bmatrix} a_{IY}^2 \\ a_{OY}^2 \\ a_{SY}^2 \end{bmatrix} \\
& + \begin{bmatrix} D_{IOY} & D_{ISY} & D_{OSY} \\ 0 & 0 & 0 \\ 0 & 0 & 0 \end{bmatrix} \begin{bmatrix} a_{IY} & a_{OY} \\ a_{IY} & a_{SY} \\ a_{OY} & a_{SY} \end{bmatrix} + \begin{bmatrix} 0 & \text{TSF}_Y & 0 \\ 0 & 0 & 0 \\ 0 & 0 & 0 \end{bmatrix} \begin{bmatrix} 0 \\ t_{gY} \\ 0 \end{bmatrix} \Bigg\} \\
& - C_{SGZ}^p \begin{bmatrix} D_{FZ} \\ 0 \\ 0 \end{bmatrix} + \begin{bmatrix} D_{IZ} & D_{OZ} & D_{SZ} \\ 0 & 0 & 0 \\ 0 & 0 & 0 \end{bmatrix} \begin{bmatrix} a_{IZ} \\ a_{OZ} \\ a_{SZ} \end{bmatrix} \\
& + \begin{bmatrix} D_{IIZ} & D_{OOZ} & D_{SSZ} \\ 0 & 0 & 0 \\ 0 & 0 & 0 \end{bmatrix} \begin{bmatrix} a_{IZ}^2 \\ a_{OZ}^2 \\ a_{SZ}^2 \end{bmatrix} \\
& + \begin{bmatrix} D_{IOZ} & D_{ISZ} & D_{OSZ} \\ 0 & 0 & 0 \\ 0 & 0 & 0 \end{bmatrix} \begin{bmatrix} a_{IZ} & a_{OZ} \\ a_{IZ} & a_{SZ} \\ a_{OZ} & a_{SZ} \end{bmatrix} + \begin{bmatrix} 0 & 0 & \text{TSF}_Z \\ 0 & 0 & 0 \\ 0 & 0 & 0 \end{bmatrix} \begin{bmatrix} 0 \\ 0 \\ t_{gZ} \end{bmatrix} \Bigg\} \\
& - C_r^p \omega_{ir}^r + \omega_{SERVO}^p
\end{aligned}$$

(2.33)
Cont.

where

a_{Ij} , a_{Oj} , a_{Sj} ($j = X, Y, Z$) - are the applied accelerations along the gyro input, output, and spin axes respectively (these will be defined in Section 3)

TSF_j ($j = X, Y, Z$) - are the internal gyro torquer scale factors

t_{gj} ($j = X, Y, Z$) - are the gyro command torque values

Therefore,

$$TSF_j \times t_{gj} = \omega_{CMD_j} = j\text{th commanded angular rate}$$

To simplify the measurement equation, the indicated acceleration of the inner gimbal platform will be defined in the accelerometer sensor frames. Applying the accelerometer performance model equation, Eq. (2.26), to all three platform accelerometers, the platform indicated acceleration performance model is:

$$\begin{aligned} A_{IND}^s = \begin{bmatrix} A_X \\ A_Y \\ A_Z \end{bmatrix} &= \begin{bmatrix} K_{OX} \\ K_{OY} \\ K_{OZ} \end{bmatrix} + \begin{bmatrix} K_{1X} & 0 & 0 \\ 0 & K_{1Y} & 0 \\ 0 & 0 & K_{1Z} \end{bmatrix} \begin{bmatrix} a_{IAX} \\ a_{IAY} \\ a_{IAZ} \end{bmatrix} \\ &+ \begin{bmatrix} K_{2X} & 0 & 0 \\ 0 & K_{2Y} & 0 \\ 0 & 0 & K_{2Z} \end{bmatrix} \begin{bmatrix} a_{IAX}^2 \\ a_{IAY}^2 \\ a_{IAZ}^2 \end{bmatrix} \end{aligned} \quad (2.34)$$

$$\begin{aligned}
& + \begin{bmatrix} K_{3X} & 0 & 0 \\ 0 & K_{3Y} & 0 \\ 0 & 0 & K_{3Z} \end{bmatrix} \begin{bmatrix} a_{IAX}^3 \\ a_{IAY}^3 \\ a_{IAZ}^3 \end{bmatrix} \\
& + \begin{bmatrix} K_{IPX} & 0 & 0 \\ 0 & K_{IPY} & 0 \\ 0 & 0 & K_{IPZ} \end{bmatrix} \begin{bmatrix} a_{IAX} & a_{PX} \\ a_{IAY} & a_{PY} \\ a_{IAZ} & a_{PZ} \end{bmatrix}
\end{aligned}
\tag{2.34}$$

Cont.

where

a_{IAj} , a_{Pj} ($j = X, Y, Z$) - are the applied accelerations along the accelerometer input and pendulous axes respectively (these will be defined in Section 3)

We now have all the performance models necessary to define the state and measurement dynamics of the calibration problem. In the next section, the applied sensor acceleration with respect to inertial space will be developed.

SECTION 3

APPLIED ACCELERATION

The acceleration that is applied to the inertial sensor axis frames is developed in this section. Since the major portion of the applied acceleration is due to the kinematic motion of the centrifuge, a description of the centrifuge and the various coordinate transformations required to describe the motion will be defined.

3.1 DESCRIPTION OF THE 260-INCH CENTRIFUGE

The 260-inch radius precision centrifuge, shown in the cutaway view of Figure 1.1, is enclosed in a building 90 feet in diameter [3]. The main arm is a steel weldment formed by two double-edge beams tied together by trusses to form a single beam. The arm is totally enclosed in a cylindrically shaped aerodynamic shroud (referred to as the dynamic cylinder in Figure 1.1), 50 feet in diameter and 11 feet high, that rotates with the arm. The aerodynamic shroud is enclosed in a smooth-walled, stationary cylinder to reduce drag. Chilled-water cooling plates located at the top and bottom of the stationary wall reduce the temperature rise between the shroud and the stationary wall due to aerodynamic heating. The main spindle, which is 4 feet in diameter, is supported by upper and lower hydrostatic oil bearings. The lower bearing supports the entire weight of the rotating cylinder, consisting of the main arm structure and shroud, which is approximately 45 tons. Mounted just below the upper bearing are two drive motors: a 400-horsepower induction motor to accelerate the arm and a 175-horsepower synchronous motor for constant rate drive.

The speed of the main arm is continuously variable to attain acceleration levels from 0.25 to 100 g's by means of a frequency divider with a vernier control and a precision frequency source. The frequency divider provides the reference signal to stabilize the synchronous motor after the induction motor has driven the main arm up to the selected speed. Speed variations of the synchronous drive system are further reduced by damping in the centrifuge feedback stabilization loop. Angular velocity errors, averaged over a 50-second time period, have been measured at less than 3 micro-radians per second.

The centrifuge arm is statically balanced at rest by counterweights placed on the opposite end of the arm from the counter-rotating platform. Dynamic balance is achieved during operation by motor-driven weights located on the arm structure. The motor-driven weight locations are changed until the output of proximity detectors, located in the upper and lower bearings, are equalized. Equalization of the detector outputs implies that a dynamic balance has been achieved, since the main spindle rotational axis will be centered in the hydrostatic bearing housings, which were aligned to the local vertical during installation. The main spindle verticality is adjustable during the static balance procedure to 1 arc-second using the output of the proximity detectors; changes in verticality during operation are measurable to 0.2 arc-second using the detectors.

The centrifuge radius is also measured statically and dynamically. The static radius is measured to an accuracy of 2 parts per million of the 260-inch radius by a micrometer consisting of three calibrated Invar rods and a precision stepper motor. The motor

drives the rods to abut the main and CRP spindles, thereby measuring the desired distance between the center of the centrifuge and the center of the CRP. The change in radius or stretch of the arm due to g-loading and aerodynamic heating is measured to an accuracy of 1 part per million by determining the capacitance between two plates that are part of a capacitance bridge network. One plate is attached to a probe that is fixed to the CRP spindle, which rotates with the arm; the other is a movable plate that is attached to the stationary wall. During centrifuge operation, the stationary wall plate is moved outward to bring it in close proximity with the plate attached to the rotating arm; the value of capacitance between the plates and any change in capacitance are proportional to the distance and change in distance between the plates, which in turn provide the dynamic radius measurement. The stretch at both the top and bottom of the centrifuge arm is measured to detect arm droop or rise caused by unequal g-loading or heating of the upper and lower arm structure. There are three pairs of dynamic radius-measuring stations, equally spaced around the stationary wall, to separate a change in radius from a displacement of the main spindle.

The CRP is a cylinder, 50 inches in diameter and 50 inches high, that will support a 30,000-g-lb load (i. e., a 300-lb load at 100 g's). The CRP spindle is also supported by hydrostatic oil bearings; therefore, procedures similar to those used for the main spindle permit the CRP spindle to be adjusted within 5 arc-seconds of vertical with an accuracy of 0.2 arc-second when the centrifuge is at rest, and changes in verticality are measurable to 2 arc-seconds during operation. The

CRP drive system is a phase-lock position servo that utilizes an error signal to maintain synchronous counter-rotation. The error signal is obtained either from a pair of identical 16-pole resolvers, one mounted on the main spindle and the other on the CRP spindle, or from a pair of 720-tooth gears similarly mounted. The error signal is amplified to drive two induction motors on the CRP. Power and instrumentation signals are transferred to and from the main centrifuge arm and CRP via silver brush and slip ring assemblies mounted on the spindles.

A simplified example of the acceleration applied to the system platform axes during centrifuge operation in the counter-rotating mode is shown in Figure 3.1. The simplifying assumptions of this example are as follows:

- (a) Perfect counter-rotation of the CRP is assumed.
- (b) The system platform error drift and gyro command rate are zero.
- (c) The system stabilization function is assumed to be perfect.
- (d) Earth rate is assumed to be zero.
- (e) The acceleration applied to the platform axes is limited to the centripetal acceleration of the centrifuge.

The example shows that the acceleration along the platform axes in the rotational plane is a sinusoid with a zero-to-peak magnitude equal to the centripetal acceleration. The angular rate range of the centrifuge is 0.609 rad/sec at 0.25 g's to 12.176 rad/sec at 100 g's, based on a radius of 260 inches and a local-gravity magnitude of 32.1238 ft/sec^2 . The frequency range associated with the preceding angular rates is

LEGEND:

a_c - CENTRIFUGE CENTRIPETAL ACCELERATION
(ALWAYS ACTS INWARD)

x_p, y_p - SYSTEM PLATFORM AXES

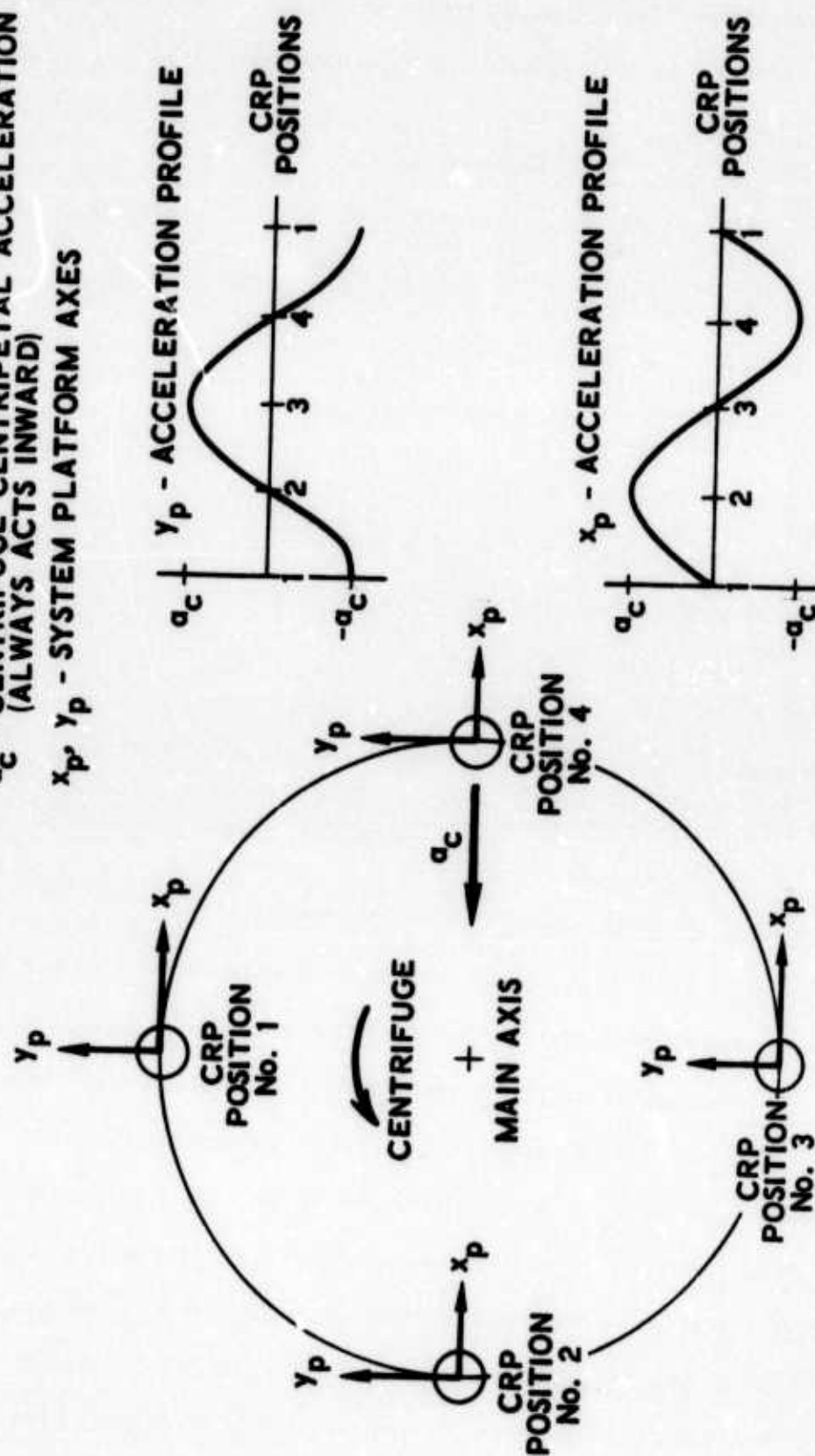


Figure 3.1. Simplified Centrifuge Acceleration Profile

0.097 to 1.938 Hz; therefore, as previously mentioned, the acceleration applied to the system is a low frequency sinusoid.

3.2 COORDINATE TRANSFORMATIONS

The basic coordinate frames represented in the major transformations linking inertial space to the sensor axes are:

- I - Inertial frame
- E - Earth frame
- C - Centrifuge main arm frame
- R - Centrifuge counter-rotating platform frame
- P - System inner gimbal platform frame
- S - Sensor frame

All coordinate frames will be considered right-hand orthogonal axis sets.

3.2.1 Inertial - Earth Transformation

The inertial frame is defined at the center of the earth and is nonrotating with respect to the "fixed stars". The X_i and Y_i axes lie in the equatorial plane and the Z_i axis is coincident with the earth's angular velocity vector, ω_{ie} . As illustrated in Figure 3.2, the X_i axis intersects the local meridian at the initial calibration time (i.e., when $t = 0$). The earth frame, reference Figure 3.2, is a tangent frame that is fixed on the rotating earth, with its origin at the intersection of the geographic latitude L , and the local meridian at a point on the earth's surface corresponding to the location of the center

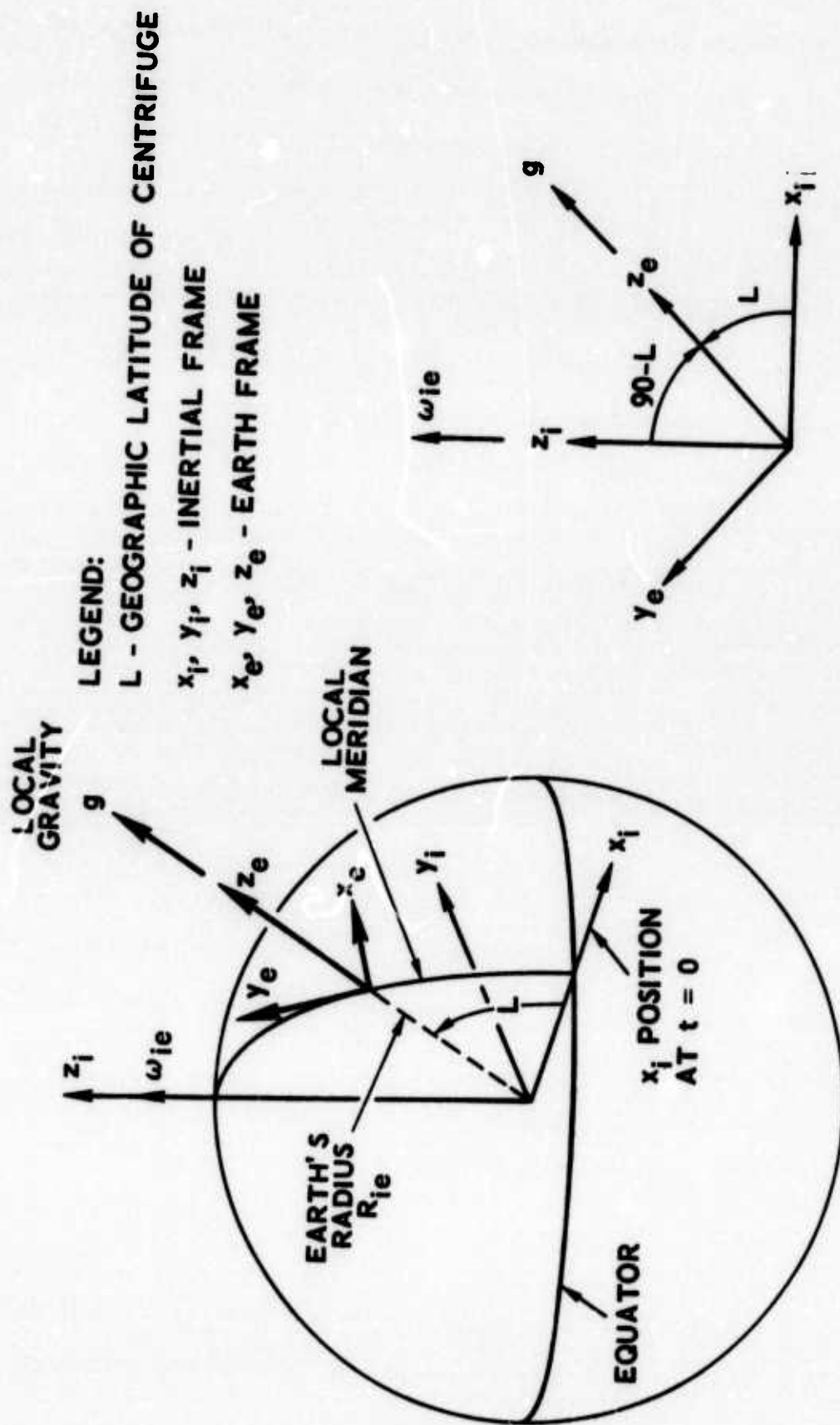


Figure 3.2. Inertial and Earth Coordinate Frames

of the centrifuge main spindle. The axes are aligned with the east, north, and up directions. The up axis, Z_e , is defined to be coincident with the local vertical. Since the best physical measure of the local vertical is the local-gravity vector \underline{g} , the local vertical is considered coincident with the local-gravity vector and any deviations of \underline{g} caused by mass anomalies are assumed negligible [13]. The north axis Y_e is in the direction of the projection of the earth's inertial angular velocity vector into the local horizontal plane. The east axis X_e completes the right-hand orthogonal set and also lies in the local horizontal plane.

From Figure 3.2, the inertial-earth coordinate transformation matrix is

$$C_i^e = \begin{bmatrix} 0 & 1 & 0 \\ -\sin L & 0 & \cos L \\ \cos L & 0 & \sin L \end{bmatrix} \quad (3.1)$$

The matrix representation of the rotation of the earth frame with respect to the inertial frame, coordinatized in the earth's axes, is

$$\omega_{ie}^e = \{0, \omega_{ie} \cos L, \omega_{ie} \sin L\} \quad (3.2)$$

where

$$\omega_{ie} = 7.292116 \times 10^{-5} \text{ rad/sec} = \text{the scalar value of earth rate}$$

$$L = 32^\circ 53' 26.614'' = \text{geographic latitude of the centrifuge}$$

Defining:

$$WES = \omega_{ie} \sin L = 3.95990552 \times 10^{-5} \text{ rad/sec}$$

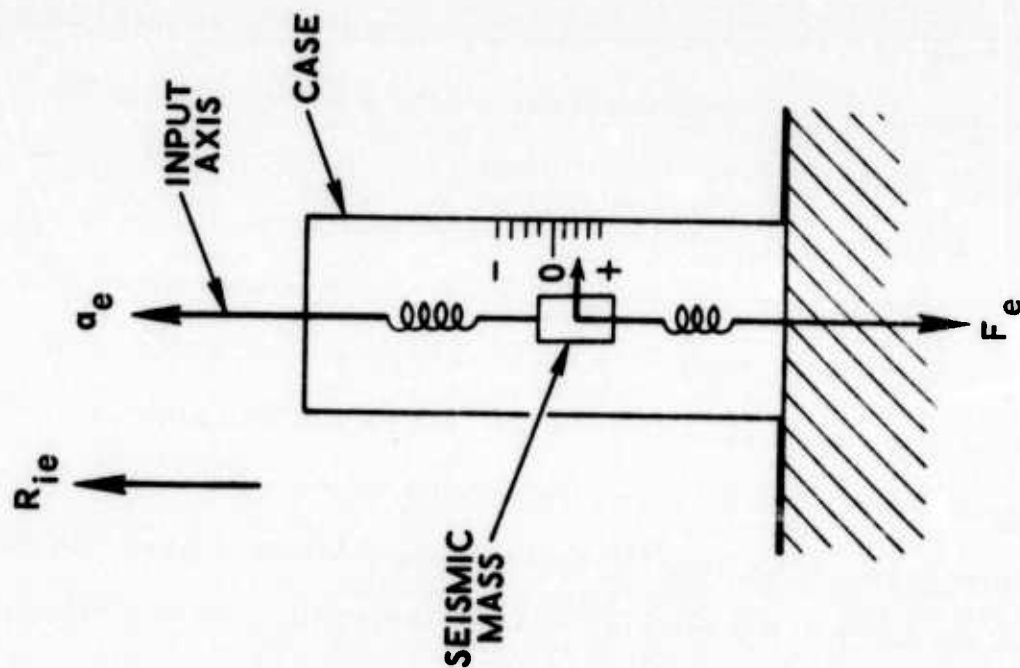
$$WEC = \omega_{ie} \cos L = 6.1232531 \times 10^{-5} \text{ rad/sec}$$

The cross-product matrix form is

$$W_{ie}^{ek} = \begin{bmatrix} 0 & -WES & WEC \\ WES & 0 & 0 \\ -WEC & 0 & 0 \end{bmatrix} \quad (3.3)$$

The scalar distance between the coordinate frames, R_{ie} , remains constant and is equal to the earth's radius.

Before describing the next transformation, it should be noted from Figure 3.2 that the local-gravity vector has been shown as acting outward from the earth, rather than inward. This convention is used in the guidance test field because of the concept of acceleration as measured by an accelerometer whose case is fixed on the platform, and the platform is mounted on the test device. Consider the simple linear accelerometer, at rest on a spherical homogeneous nonrotating earth, illustrated in Figure 3.3. The accelerometer input axis is parallel to the earth radius vector \underline{R}_{ie} , and a positive output acceleration corresponds to a positive displacement of the accelerometer's seismic mass. Since the case of the accelerometer is fixed, the mass attraction force of the earth \underline{F}_e acts on the seismic mass of the accelerometer. The seismic mass is displaced until the restoring



LEGEND:

F_e - EARTH MASS ATTRACTION FORCE

G_e - EARTH GRAVITATIONAL CONSTANT

M_e - EARTH MASS

m - SEISMIC ELEMENT MASS

R_{ie} - EARTH RADIUS

a_e - INDICATED ACCELERATION

$$F_e = \frac{G_e M_e m}{R_{ie}^2}$$

Figure 3.3. Accelerometer at Rest on a Spherical Homogeneous Nonrotating Earth

force of the spring equals the mass attraction force. Because of the positive mass displacement, the accelerometer will indicate a positive acceleration output of (Reference Figure 3.3):

$$\underline{a}_{IND} = \underline{a}_e = \frac{1}{R_{ie}} \frac{G_e M_e}{R_{ie}^2} = \frac{1}{R_{ie}} \frac{F_e}{m} \quad (3.4)$$

The second component of the local-gravity vector is due to the centripetal acceleration generated by earth's rotation, $\underline{\omega}_{ie} \times (\underline{\omega}_{ie} \times \underline{R}_{ie})$, illustrated in Figure 3.4. The specific force \underline{f}_c , acting on a unit seismic mass, is equal in magnitude, but opposite in direction, to the centripetal acceleration. The total force acting on the seismic element is the vector addition of \underline{F}_e and \underline{f}_e , causing a positive displacement, which, in turn, is interpreted by the accelerometer as a positive acceleration. Therefore, by convention, the local-gravity vector is defined as acting outward from the earth and is equal to the following vector equation:

$$\underline{g} = \underline{\omega}_{ie} \times (\underline{\omega}_{ie} \times \underline{R}_{ie}) + \frac{1}{R_{ie}} \frac{G_e M_e}{R_{ie}^2} \quad (3.5)$$

3.2.2 Earth-Centrifuge Main Arm Transformation

A number of intermediate transformations are required to go from the earth tangent axes to the centrifuge main arm axes [14]. The first intermediate transformation shown in Figure 3.5 accounts for any variation of the centrifuge main spindle from the local vertical.

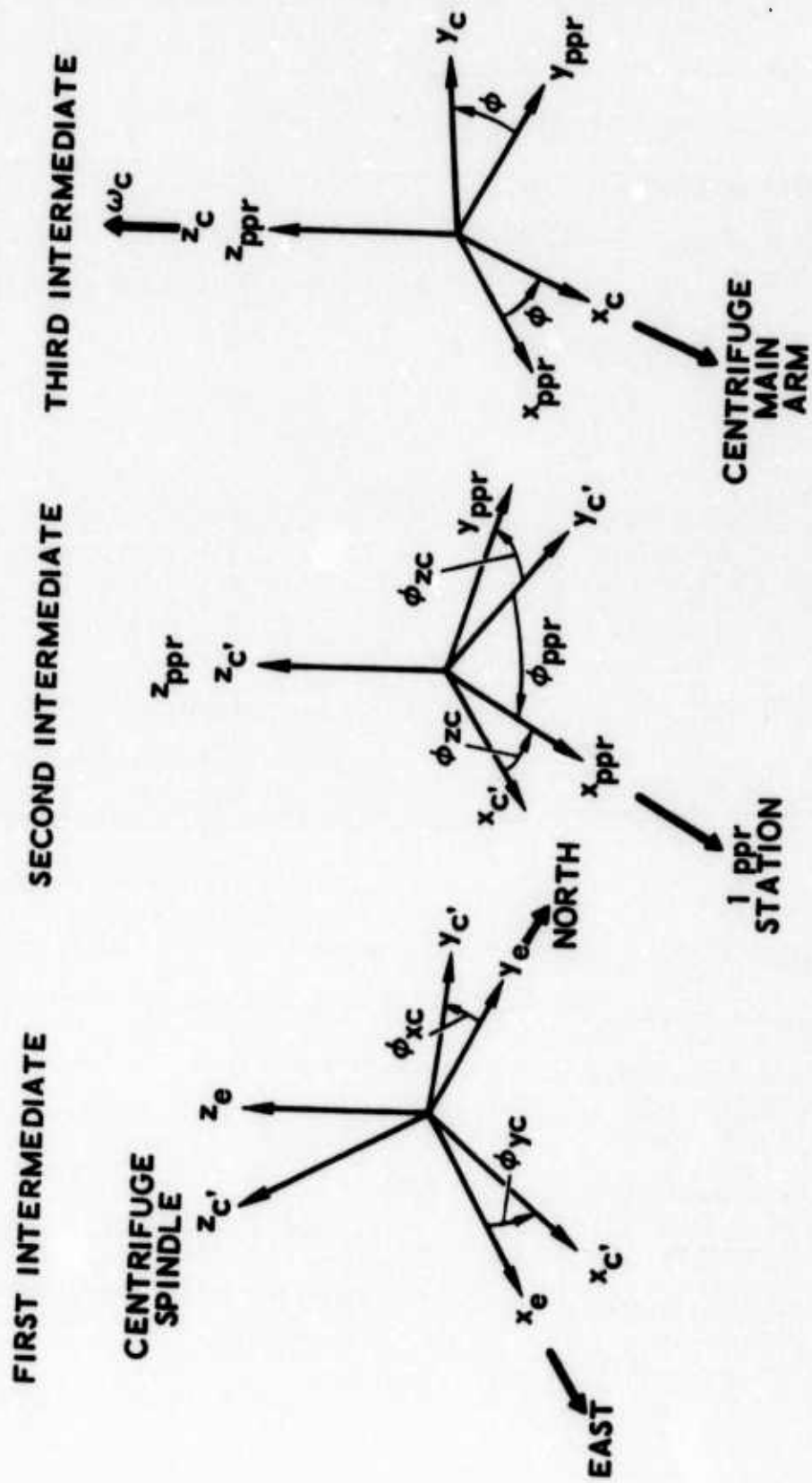


Figure 3.5. Earth - Centrifuge Main Arm Coordinate Frames

A tilt off of the east direction, caused by an east-west bearing deflection, is represented by the angle ϕ_{yc} ; a tilt of the north direction, caused by a north-south bearing deflection, is represented by the angle ϕ_{xc} . As discussed in Section 3.1, the main spindle verticality should be within a few arc-seconds, so that the following small angle transformation can be used to depict the earth frame e to misaligned spindle axis frame c' transformation.

$$C_e^{c'} = \begin{bmatrix} 1 & 0 & -\phi_{yc} \\ 0 & 1 & \phi_{xc} \\ \phi_{yc} & -\phi_{xc} & 1 \end{bmatrix} \quad (3.6)$$

The second intermediate transformation shown in Figure 3.5 is required to establish a physical time reference during the calibration program. One of the dynamic radius-measuring stations discussed in Section 3.1 is used to provide a pulse per revolution of the centrifuge. The electronic pulse is used to secure an initial condition ($t = 0$) time reference and to determine the average centrifuge angular rate by measuring the time between pulses. The 1-pulse-per-revolution axis frame is defined with the Z_{ppr} axis coincident with the centrifuge spindle, the X_{ppr} axis directed toward the pulse-per-revolution station, and the Y_{ppr} axis completes the orthogonal set. From Figure 3.5, the transformation from the misaligned spindle axis frame to the pulse-per-revolution frame is

$$C_{c'}^{ppr} = \begin{bmatrix} \cos \phi_{zc} & \sin \phi_{zc} & 0 \\ -\sin \phi_{zc} & \cos \phi_{zc} & 0 \\ 0 & 0 & 1 \end{bmatrix} \quad (3.7)$$

where

$$\phi_{zc} = 90^\circ - \phi_{ppr}$$

ϕ_{ppr} = astronomic heading of the 1-pulse-per-revolution (ppr) station with respect to north

The astronomic heading [13] is by definition the clockwise angle measured from north to the pulse-per-revolution station.

The last intermediate transformation shown in Figure 3.5 transforms the ppr axis frame into the centrifuge main arm frame. The main arm frame is defined with the Z_c axis along the centrifuge spindle, the X_c axis directed outward along the centerline of the main arm and through the center of the counter-rotating platform, and the Y_c axis completes the orthogonal set. The transformation is

$$C_{ppr}^c = \begin{bmatrix} \cos \phi & \sin \phi & 0 \\ -\sin \phi & \cos \phi & 0 \\ 0 & 0 & 1 \end{bmatrix} \quad (3.8)$$

where

$$\phi = \phi_c + \phi_o$$

ϕ_o = angle from 1-pulse-per-revolution contact to main arm
centerline through center of CRP at $t = 0$

$$\phi_c = \int_0^t \omega_c dt$$

$$\omega_c = \omega_{co} + \delta\omega_c$$

ω_{co} = average centrifuge angular rate

$\delta\omega_c$ = centrifuge rate variation about the average rate caused by
variations in the main arm drive system

Equations (3.6) through (3.8) give the following transformation for the earth-to-centrifuge main arm frame.

$$C_e^c = C_{ppr}^c C_{c'}^{ppr} C_e^{c'} \begin{bmatrix} c_{11} & c_{12} & c_{13} \\ c_{21} & c_{22} & c_{23} \\ c_{31} & c_{32} & c_{33} \end{bmatrix} \quad (3.9)$$

where

$$c_{11} = \cos \phi \cos \phi_{zc} - \sin \phi \sin \phi_{zc}$$

$$c_{12} = \cos \phi \sin \phi_{zc} + \sin \phi \cos \phi_{zc}$$

$$c_{13} = -\cos \phi \cos \phi_{zc} \cdot \phi_{yc} + \cos \phi \sin \phi_{zc} \cdot \phi_{xc} \\ + \sin \phi \sin \phi_{zc} \cdot \phi_{yc} + \sin \phi \cos \phi_{zc} \cdot \phi_{xc}$$

$$c_{21} = -\sin \phi \cos \phi_{zc} - \cos \phi \sin \phi_{zc}$$

$$c_{22} = -\sin \phi \sin \phi_{zc} + \cos \phi \cos \phi_{zc}$$

$$c_{23} = \sin \phi \cos \phi_{zc} \cdot \phi_{yc} - \sin \phi \sin \phi_{zc} \cdot \phi_{xc} \\ + \cos \phi \sin \phi_{zc} \cdot \phi_{yc} + \cos \phi \cos \phi_{zc} \cdot \phi_{xc}$$

$$c_{31} = \phi_{yc}$$

$$c_{32} = -\phi_{xc}$$

$$c_{33} = 1$$

The matrix representation of the rotation of the centrifuge with respect to the earth frame, coordinatized in the centrifuge axes, is

$$\omega_{ec}^c = \{0, 0, \omega_c\} \quad (3.10)$$

Therefore, the cross-product matrix is

$$W_{ec}^{ck} = \begin{bmatrix} 0 & -\omega_c & 0 \\ \omega_c & 0 & 0 \\ 0 & 0 & 0 \end{bmatrix} \quad (3.11)$$

Since the origins of the earth and centrifuge main arm frame are the same, the scalar distance $R_{ec} = 0$.

3.2.3 Centrifuge Main Arm - Centrifuge Counter-Rotating Platform Transformation

Two intermediate transformations are required to link the centrifuge main arm frame to the centrifuge counter-rotating platform frame. The first transformation shown in Figure 3.6 accounts for any variation of the CRP spindle axis with respect to the centrifuge main arm axes. In other words, it accounts for misalignments that exist between the main spindle and CRP spindle, since the centrifuge main arm vertical axis is coincident with the main spindle axis. The angles θ_{xr} and θ_{yr} represent static as well as dynamic misalignments due to g-loading. Since both the main and CRP spindle verticality are within a few arc-seconds, the misalignment between the two spindles should be within a few arc-seconds. Consequently, the following small angle transformation can be used to depict the centrifuge main arm frame to misaligned CRP spindle axis frame r' transformation.

$$C_c^{r'} = \begin{bmatrix} 1 & 0 & -\theta_{yr} \\ 0 & 1 & \theta_{xr} \\ \theta_{yr} & -\theta_{xr} & 1 \end{bmatrix} \quad (3.12)$$

The last transformation shown in Figure 3.6 transforms the misaligned CRP spindle axes into the CRP axis frame r .

$$C_r^r = \begin{bmatrix} \cos \theta & -\sin \theta & 0 \\ \sin \theta & \cos \theta & 0 \\ 0 & 0 & 1 \end{bmatrix} \quad (3.13)$$

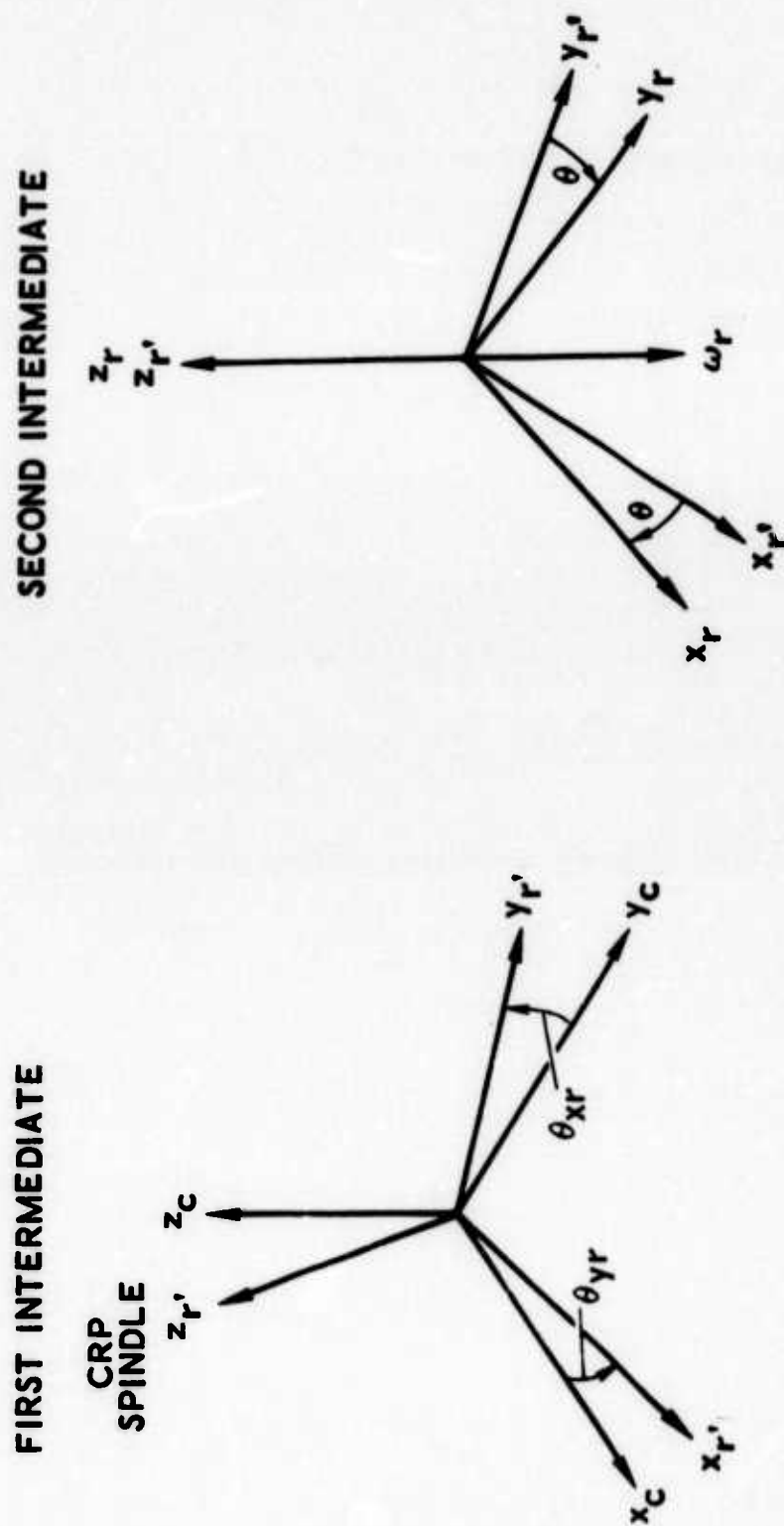


Figure 3.6. Centrifuge Main Arm - CRP Coordinate Frames

where

$$\theta = \theta_r + \theta_o$$

$$\theta_o = \text{angle between } X_r \text{ and } X_c \text{ axes at } t = 0$$

$$\theta_r = \int_0^t \omega_r dt$$

$$\omega_r = \text{CRP angular rate} = \omega_c + \delta\omega_r$$

$$= \omega_{co} + \delta\omega_c + \delta\omega_r [\text{Reference Eq. (3.8).}]$$

$$\delta\omega_r = \text{CRP rate uncertainty caused by variations in the CRP drive system}$$

Equations (3.12) and (3.13) give the total transformation:

$$C_c^r = C_r^r, C_c^{r'} = \begin{bmatrix} c_{11} & c_{12} & c_{13} \\ c_{21} & c_{22} & c_{23} \\ c_{31} & c_{32} & c_{33} \end{bmatrix} \quad (3.14)$$

where

$$c_{11} = \cos \theta$$

$$c_{12} = -\sin \theta$$

$$c_{13} = -\cos \theta \cdot \theta_{yr} - \sin \theta \cdot \theta_{xr}$$

$$c_{21} = \sin \theta$$

$$c_{22} = \cos \theta$$

$$c_{23} = -\sin \theta \cdot \theta_{yr} + \cos \theta \cdot \theta_{xr}$$

$$c_{31} = \theta_{yr}$$

$$c_{32} = -\theta_{xr}$$

$$c_{33} = 1$$

The rotational and cross-product matrices are

$$\omega_{cr}^r = \{0, 0, -\omega_r\} \quad (3.15)$$

$$W_{cr}^{rk} = \begin{bmatrix} 0 & \omega_r & 0 \\ -\omega_r & 0 & 0 \\ 0 & 0 & 0 \end{bmatrix}$$

The scalar distance between the coordinate frames is

$$R_{cr} = r_o + \delta r \quad (3.16)$$

where

r_o = nominal 260-inch radius

δr = static and dynamic change in the radius from nominal

Measurements of the centrifuge radius have shown that, once the centrifuge is stabilized at a specified g-level, the dynamic change in radius or stretch remains constant, implying that the change is mainly due to g-loading, rather than aerodynamic heating. Consequently, R_{cr} can be considered a constant at each g-level.

As mentioned in Section 1, the purpose of the counter-rotating platform is to isolate the platform gyros from the centrifuge angular rate. Perfect isolation implies perfect counter-rotation; however, the transformations of this section reveal that misalignment between the two spindles and/or variations in either the main or CRP drive system prevent perfect counter-rotation. Therefore, a component of centrifuge rate will be sensed by the platform gyros. If the magnitude of angular rate is large enough to stimulate instrument error terms proportional to rate, then the models of Section 2 must be expanded to include those effects. Measurement data taken thus far on the centrifuge environment shows that expansion of the performance models is not necessary. However, the component of centrifuge rate is large enough to mask the drift-producing terms contained in Eq. (2.20). As shown by Thede [14], a CRP axis misalignment of 5 arc-seconds gives a component of centrifuge rate equal to 9.48×10^{-8} rad/sec at the 10-g operating level of the centrifuge. This compares to a nominal value of a gyro compliance term (such as D_{II}) of 23.7×10^{-8} rad/sec. The centrifuge rate that is sensed by the platform gyros, whose outputs drive the platform via the stabilization loops to null the sensed rate, must be accounted for to distinguish between the platform motion due to sensed centrifuge rate and motion due to the drift terms. The term in the platform rate equation, Eq. (2.33), that accounts for the centrifuge rate effect is ω_{ir}^r .

$$\begin{aligned}
\omega_{ir}^r &= C_e^r \omega_{ie}^e + C_c^r \omega_{ec}^c + \omega_{cr}^r \\
&= C_e^r \omega_{ie}^e + C_c^r \begin{bmatrix} 0 \\ 0 \\ \omega_{co} + \delta\omega_c \end{bmatrix} + \begin{bmatrix} 0 \\ 0 \\ -\omega_c - \delta\omega_r \end{bmatrix} \quad (3.17)
\end{aligned}$$

So the variations in the main and CRP drive system are represented, and the misalignments are contained in the C_c^r transformation given by Eq. (3.14). The important point is that the misalignments and rate variations must be measured quantities. If the measurement accuracy is not sufficient to accurately account for the centrifuge rate effect, then these parameters must also be estimated by the filtering process.

The Inertial Navigation System will be mounted on a fixture located on the CRP. Since the mounting fixture is aligned and leveled by extremely accurate laboratory optical equipment, the mounting fixture or system platform base frame will be made coincident with the CRP frame. Therefore, the transformation from the centrifuge CRP frame to the system inner gimbal platform frame will be identical to the platform base to inner platform p frame, C_r^p , which will be defined in Section 4.

3.2.4 System Inner Gimbal Platform-Sensor Transformation

The system inner platform axes are defined by three fiducial lines that are physically inscribed on the platform. The inertial instruments also have a case axis system which is physically

inscribed on the case and referenced to a precision mounting surface. The instruments are mounted so that the case input axes are aligned with the platform inscribed axes. In other words, the X, Y, and Z gyro case input axes establish the direction of the inner platform axes. The instruments are located as close as is physically possible to the origin of the platform frame and are distributed about the origin to maintain a balanced inner gimbal. The accelerometer and gyro case axis system for the Carousel VB [10] are illustrated in Figures 3.7 and 3.8, respectively. Therefore, the locations of the instruments are

$$\begin{aligned}
 R_{p,GX}^p &= \{1, 0, -2\} && \text{(X-gyro)} \\
 R_{p,GY}^p &= \{-1, 0, -2\} && \text{(Y-gyro)} \\
 R_{p,GZ}^p &= \{0, -2, 1.5\} && \text{(Z-gyro)} \\
 R_{p,AX}^p &= \{0, -1, -2\} && \text{(X-accelerometer)} \\
 R_{p,AY}^p &= \{0, 1, -2\} && \text{(Y-accelerometer)} \\
 R_{p,AZ}^p &= \{0, 1.5, 1.5\} && \text{(Z-accelerometer)}
 \end{aligned} \tag{3.18}$$

The true sensitive or input axis of an accelerometer is based on the physical structure of the output axis and pendulous element. The true input axis will be misaligned with respect to the case axes. The sensor frames are defined by the true input axes. Figure 3.9 illustrates the inner platform-to-sensor transformations for the X, Y, and Z accelerometers.

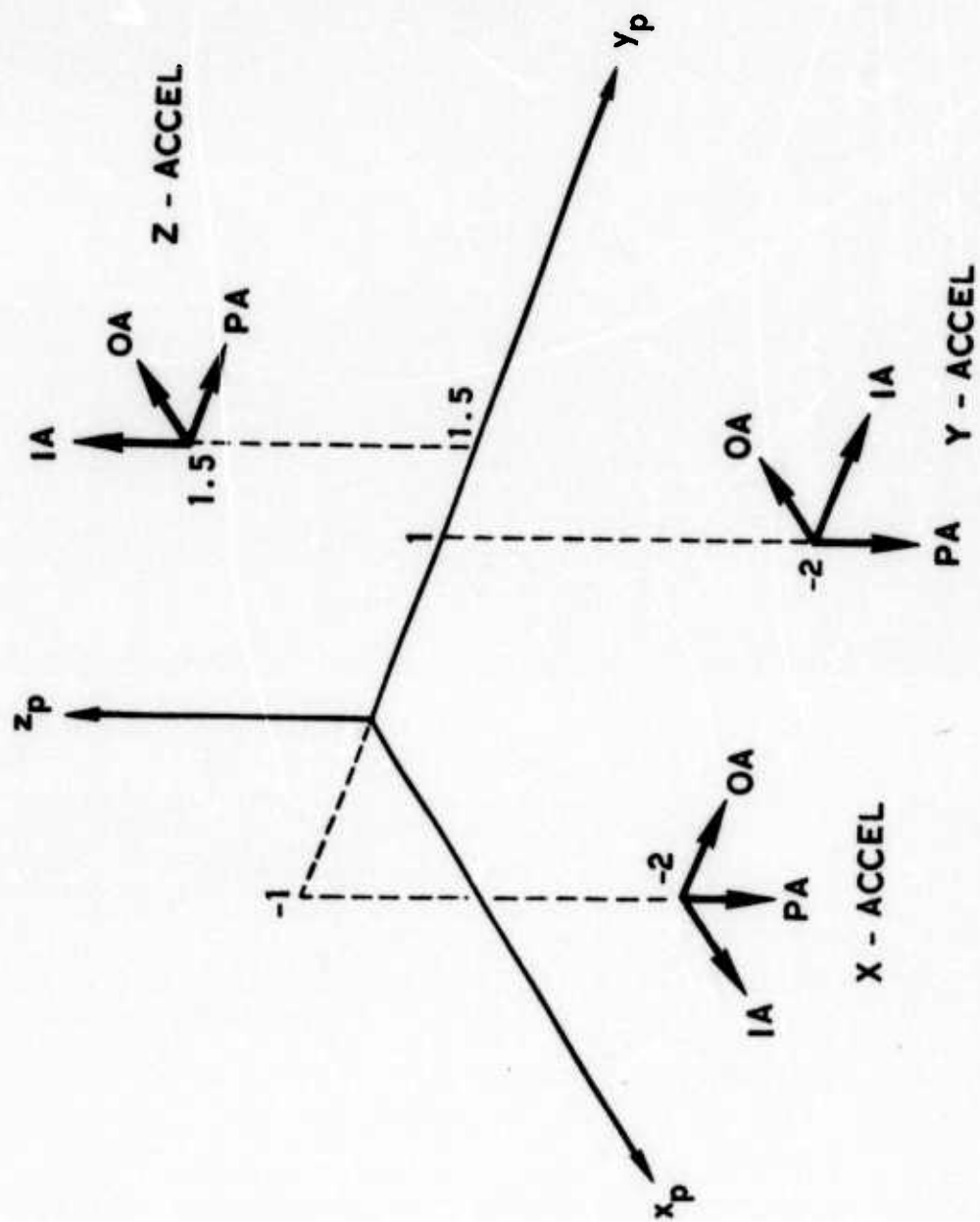


Figure 3.7. Accelerometer Case Axis System

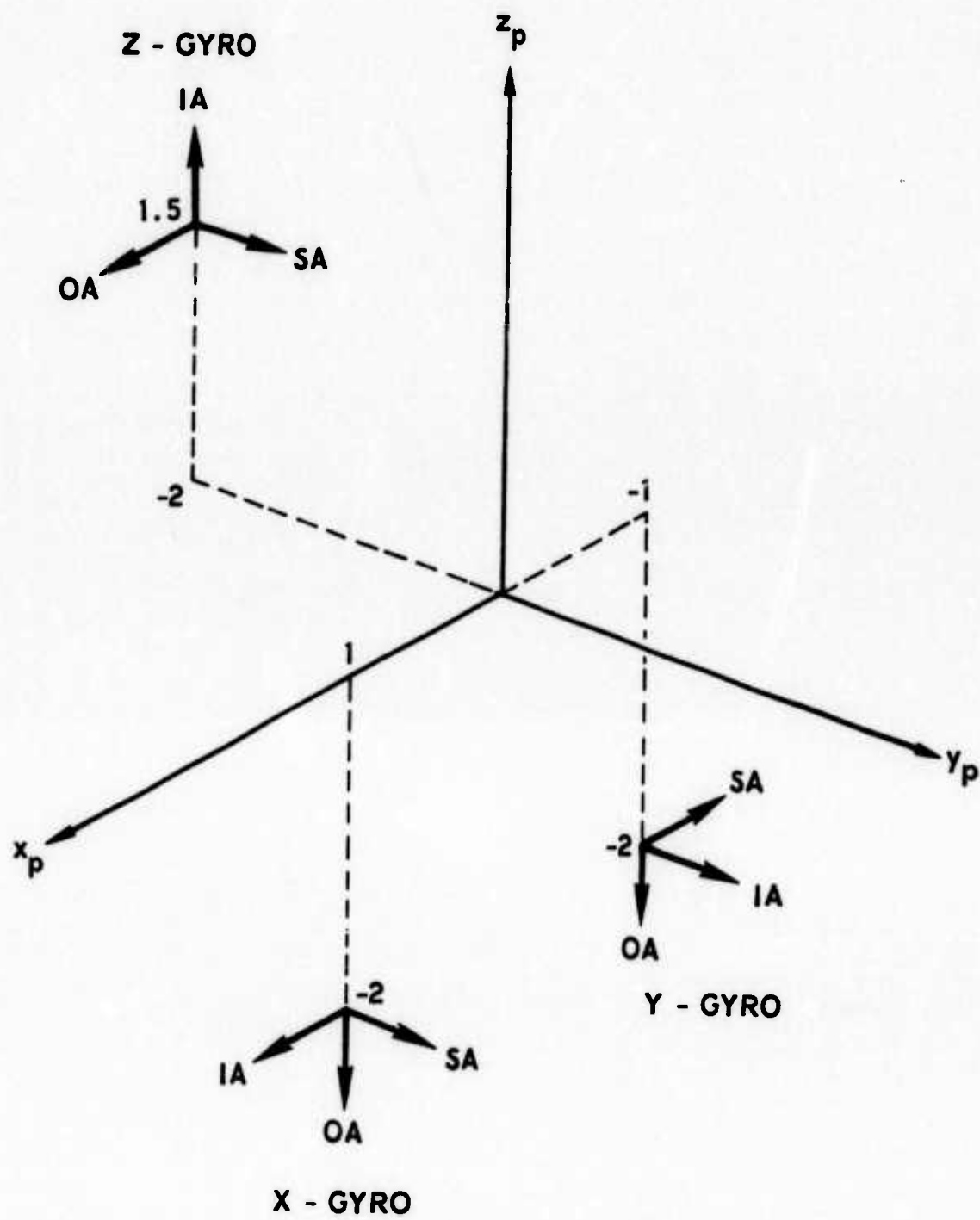


Figure 3.8. Gyro Case Axis System

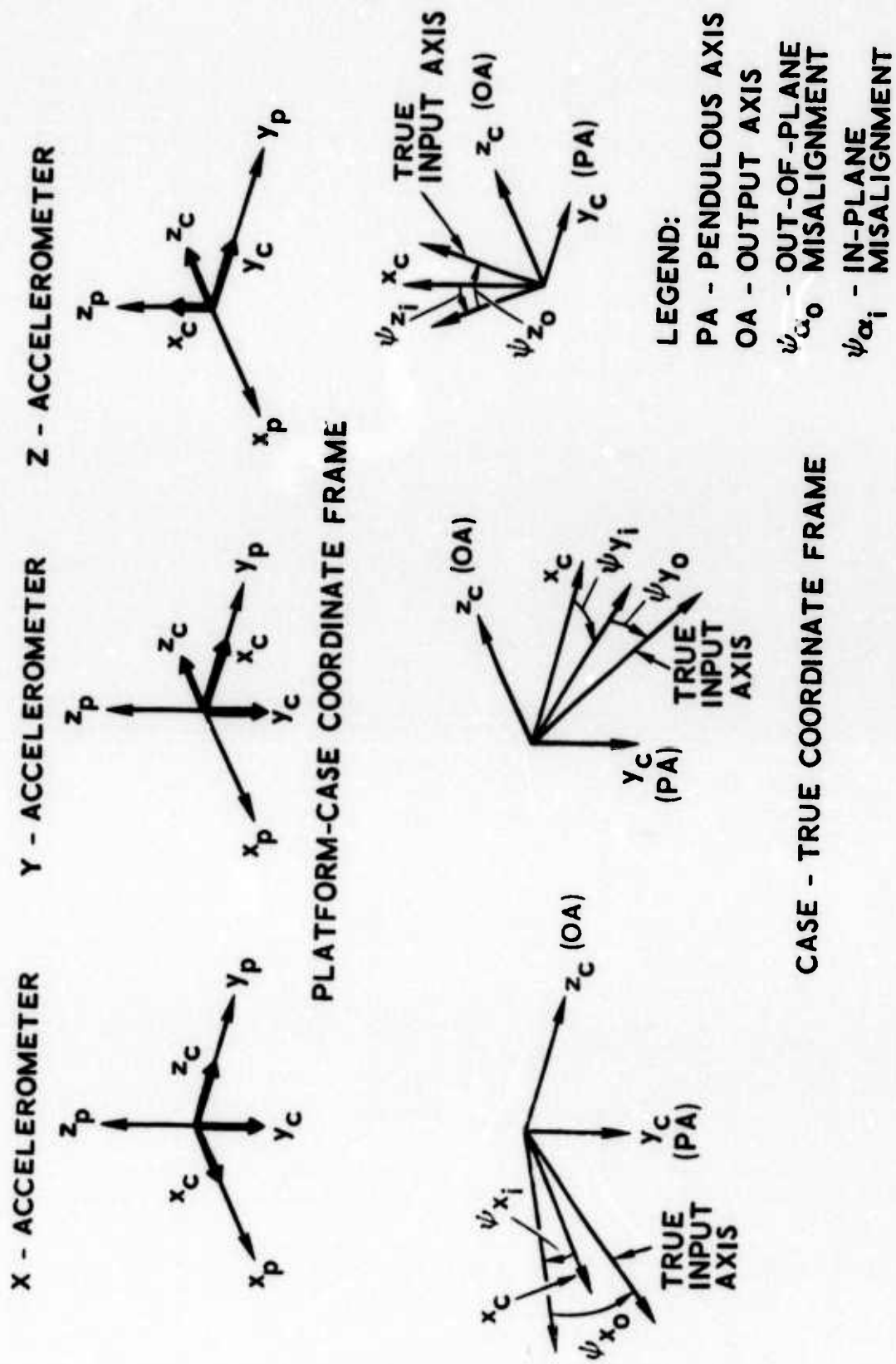
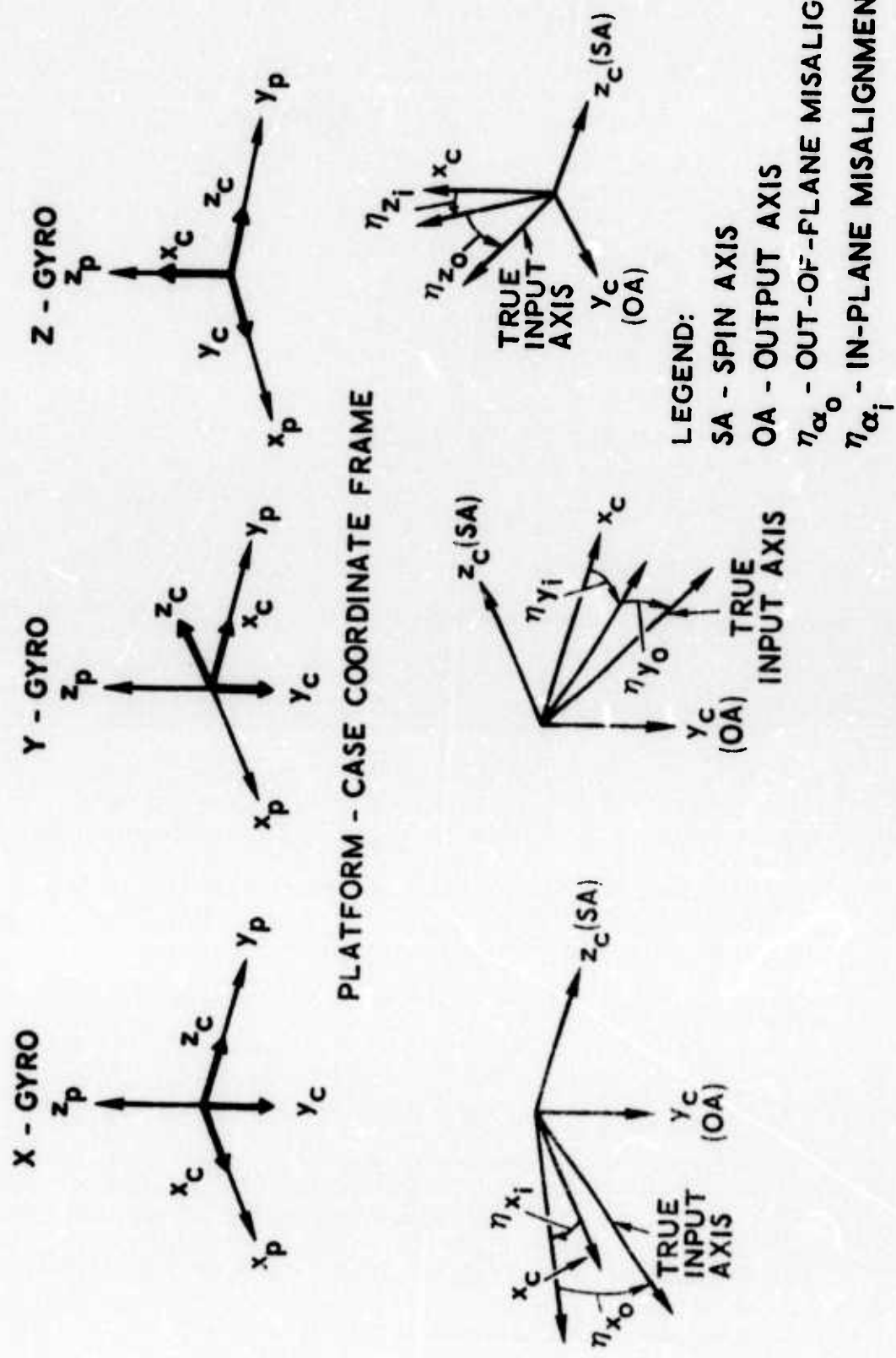


Figure 3.9. Platform - Accelerometer Coordinate Frames

$$\begin{aligned}
C_p^{SAX} &= \begin{bmatrix} 1 & -\psi_{x_i} & -\psi_{x_o} \\ -\psi_{x_o} & 0 & -1 \\ \psi_{x_i} & 1 & 0 \end{bmatrix} \\
C_p^{SAY} &= \begin{bmatrix} \psi_{y_i} & 1 & -\psi_{y_o} \\ 0 & -\psi_{y_o} & -1 \\ -1 & \psi_{y_i} & 0 \end{bmatrix} \\
C_p^{SAZ} &= \begin{bmatrix} \psi_{z_i} & \psi_{z_o} & 1 \\ 0 & 1 & -\psi_{z_o} \\ -1 & 0 & \psi_{z_i} \end{bmatrix}
\end{aligned} \tag{3.19}$$

The same applies to the gyro whose true input axis is based on the gyro gimbal element structure. Figure 3.10 illustrates the inner platform-to-sensor transformations for the X, Y, and Z gyros.

$$\begin{aligned}
C_p^{SGX} &= \begin{bmatrix} 1 & -\eta_{x_i} & -\eta_{x_o} \\ -\eta_{x_o} & 0 & -1 \\ \eta_{x_i} & 1 & 0 \end{bmatrix} \\
C_p^{SGY} &= \begin{bmatrix} \eta_{y_i} & 1 & -\eta_{y_o} \\ 0 & -\eta_{y_o} & -1 \\ -1 & \eta_{y_i} & 0 \end{bmatrix}
\end{aligned}$$



CASE - TRUE COORDINATE FRAME

Figure 3.10. Platform - Gyro Coordinate Frames

$$C_p^{SGZ} = \begin{bmatrix} \eta_{z_o} & -\eta_{z_i} & 1 \\ 1 & 0 & -\eta_{z_o} \\ 0 & 1 & \eta_{z_i} \end{bmatrix} \quad (3.20)$$

Since the instruments are mounted to the inner platform, there is no rotation between the inner platform and sensor frames. This completes the coordinate transformations.

3.3 APPLIED ACCELERATION EQUATION

The acceleration applied to the sensors is a combination of the local gravitational and kinematic accelerations. A general equation for the kinematic acceleration of the sensor frame with respect to the inertial frame is developed in Appendix A and the results contained in Eq. (A.31). Based on the coordinate frames and transformations defined in Section 3.2, in conjunction with Eqs. (A.1) and (A.2) for differentiation of a vector, the following simplifications can be made to Eq. (A.31) for application to the centrifuge environment:

- (a) $\dot{\underline{\omega}}_{ie}^i = 0$, since earth rate is constant
- (b) $\ddot{\underline{R}}_{ie}^i = \underline{\omega}_{ie} \times (\underline{\omega}_{ie} \times \underline{R}_{ie})$, which can be combined with the $\underline{\omega}_{ie} \times (\underline{\omega}_{ie} \times \underline{R}_{es})$ term in Eq. (A.31) to give $\underline{\omega}_{ie} \times (\underline{\omega}_{ie} \times \underline{R}_{is})$
- (c) $\ddot{\underline{R}}_{ec}^e = \dot{\underline{R}}_{ec}^e = \underline{R}_{ec} = 0$, since the earth and centrifuge main arm frame have a common origin
- (d) $\ddot{\underline{R}}_{cr}^c = \dot{\underline{R}}_{cr}^c = 0$, since the centrifuge radius is assumed constant at an operating g-level and the origin of the CRP frame rotates with the centrifuge main arm

- (e) $\ddot{\underline{R}}_{rp}^r = \dot{\underline{R}}_{rp}^r = \underline{R}_{rp} = 0$, since, by alignment of the mounting fixture, the CRP frame origin is coincident with the inner platform frame origin
- (f) $\ddot{\underline{R}}_{ps}^p = \dot{\underline{R}}_{ps}^p = 0$, since the distance to each sensor is a constant and the sensors are fixed to the inner platform

Equation (A. 31) reduces to

$$\begin{aligned}
 \ddot{\underline{R}}_{is}^i &= \underline{\omega}_{ec}^e \times \underline{R}_{cs} + \underline{\omega}_{cr}^c \times \underline{R}_{ps} + \underline{\omega}_{rp}^r \times \underline{R}_{ps} \\
 &+ 2\underline{\omega}_{ie} \times (\underline{\omega}_{ec} \times \underline{R}_{cs} + \underline{\omega}_{cr} \times \underline{R}_{ps} + \underline{\omega}_{rp} \times \underline{R}_{ps}) \\
 &+ 2\underline{\omega}_{ec} \times (\underline{\omega}_{cr} \times \underline{R}_{ps} + \underline{\omega}_{rp} \times \underline{R}_{ps}) \\
 &+ 2\underline{\omega}_{cr} \times (\underline{\omega}_{rp} \times \underline{R}_{ps}) + \underline{\omega}_{ie} \times (\underline{\omega}_{ie} \times \underline{R}_{is}) \\
 &+ \underline{\omega}_{ec} \times (\underline{\omega}_{ec} \times \underline{R}_{cs}) + \underline{\omega}_{cr} \times (\underline{\omega}_{cr} \times \underline{R}_{ps}) \\
 &+ \underline{\omega}_{rp} \times (\underline{\omega}_{rp} \times \underline{R}_{ps})
 \end{aligned} \tag{3.21}$$

The mass attraction term taken with respect to the sensor frame is $\frac{1}{R_{is}} \frac{G_e M_e}{R_{is}^2}$; and, adding the $\underline{\omega}_{ie} \times (\underline{\omega}_{ie} \times \underline{R}_{is})$ term from Eq. (3.21), we arrive at the local-gravity vector with respect to the sensor frame [Reference Eq. (3.5)].

$$\underline{g}^s = \underline{\omega}_{ie} \times (\underline{\omega}_{ie} \times \underline{R}_{is}) + \frac{1}{R_{is}} \frac{G_e M_e}{R_{is}^2} \tag{3.22}$$

Define

$$\underline{\omega}_{cr} = -\underline{\omega}_{ec} + \Delta \underline{\omega} \quad (3.23)$$

where

$\Delta \underline{\omega}$ = uncertainty in the counter-rotation rate due to misalignment between the two spindles and/or variations in either the main or CRP drive system

Combining Eqs. (3.21), (3.22), and (3.23); expanding the vector cross-products; and simplifying leads to the following vector expression for the total acceleration applied at the sensor frame with respect to the inertial frame \underline{A}_{is}^i .

$$\begin{aligned} \underline{A}_{is}^i = & \dot{\underline{\omega}}_{ec}^e \times \underline{R}_{cs} + \dot{\underline{\omega}}_{cr}^c \times \underline{R}_{ps} + \dot{\underline{\omega}}_{rp}^r \times \underline{R}_{ps} \\ & + 2\underline{\omega}_{ie} \times (\underline{\omega}_{ec} \times \underline{R}_{cr}) + 2\underline{\omega}_{ie} \times (\Delta \underline{\omega} \times \underline{R}_{ps}) \\ & + 2\underline{\omega}_{ie} \times (\underline{\omega}_{rp} \times \underline{R}_{ps}) + 2\Delta \underline{\omega} \times (\underline{\omega}_{rp} \times \underline{R}_{ps}) \\ & + \underline{\omega}_{ec} \times (\underline{\omega}_{ec} \times \underline{R}_{cr}) + \underline{\omega}_{ec} \times (\Delta \underline{\omega} \times \underline{R}_{ps}) \\ & - \Delta \underline{\omega} \times (\underline{\omega}_{ec} \times \underline{R}_{ps}) + \Delta \underline{\omega} \times (\Delta \underline{\omega} \times \underline{R}_{ps}) \\ & + \underline{\omega}_{rp} \times (\underline{\omega}_{rp} \times \underline{R}_{ps}) + \underline{g}^s \end{aligned} \quad (3.24)$$

Since the platform rate and platform acceleration equations [Eqs. (2.33) and (2.34), respectively] use the components of applied acceleration in

the sensor frame, we require the matrix form of Eq. (3.24) coordinatized in the sensor frame.

$$\begin{aligned}
 A_{is}^s = C_p^s C_r^p \left\{ C_c^r C_e^c \left[2W_{ie}^{ek} C_c^e W_{ec}^{ck} R_{cr}^c \right. \right. \\
 \left. \left. + 2W_{ie}^{ek} C_c^e C_r^c \Delta W_{cr}^{rk} C_p^r R_{ps}^p + G^e \right] \right. \\
 \left. + C_c^r \left[\dot{W}_{ec}^{ck} R_{cs}^c + W_{ec}^{ck} W_{ec}^{ck} R_{cr}^c \right. \right. \\
 \left. \left. + W_{ec}^{ck} C_r^c \Delta W_{cr}^{rk} C_p^r R_{ps}^p \right] \right. \\
 \left. + \left[\dot{W}_{cr}^{rk} C_p^r R_{ps}^p - \Delta W_{cr}^{rk} C_c^r W_{ec}^{ck} C_r^c C_p^r R_{ps}^p \right. \right. \\
 \left. \left. + \Delta W_{cr}^{rk} \Delta W_{cr}^{rk} C_p^r R_{ps}^p \right] \right\} \quad (1) \\
 + C_p^s C_r^p \left\{ C_c^r C_e^c \left[2W_{ie}^{ek} C_c^e C_r^c C_p^r W_{rp}^{pk} R_{ps}^p \right] \right. \\
 \left. + C_p^r \left[\dot{W}_{rp}^{pk} R_{ps}^p + W_{rp}^{pk} W_{rp}^{pk} R_{ps}^p \right] \right. \\
 \left. + \left[2\Delta W_{cr}^{rk} C_p^r W_{rp}^{pk} R_{ps}^p \right] \right\} \quad (2)
 \end{aligned} \tag{3.25}$$

① indicates Group 1

② indicates Group 2

where

W_{ie}^{ek} - is given by Eq. (3.3)

W_{ec}^{ck} - is given by Eq. (3.11)

W_{cr}^{rk} - is given by Eq. (3.15) with $\omega_r = \omega_c = \omega_{CO}$, since the $\delta\omega_r$ and $\delta\omega_c$ effects are now accounted for in the $\Delta\omega_{cr}^{rk}$ term

$$\Delta W_{cr}^{rk} = \begin{bmatrix} 0 & -(\delta\omega_r + \delta\omega_c) & 0 \\ (\delta\omega_r + \delta\omega_c) & 0 & 0 \\ 0 & 0 & 0 \end{bmatrix} \quad [\text{Reference Eq. (3.13)}]$$

$$W_{rp}^{pk} = \begin{bmatrix} 0 & -\omega_{zp} & \omega_{yp} \\ \omega_{zp} & 0 & -\omega_{xp} \\ -\omega_{yp} & \omega_{xp} & 0 \end{bmatrix} \quad [\text{Reference Eq. (2.33)}]$$

\dot{W}_{ec}^{ck} , \dot{W}_{cr}^{rk} , \dot{W}_{rp}^{pk} - are the cross-product form of the angular accelerations for the centrifuge, CRP, and platform, respectively

$G^e = \{0, 0, g\}$ is the gravitational acceleration in the earth frame, where g is the magnitude of Eq. (3.5)

$R_{cr}^c = \{r_o + \delta r, 0, 0\}$ [Reference Eq. (3.16)]

R_{ps}^p - is given by Eq. (3.18) for the specific sensor for which the applied acceleration is being determined

$$R_{cs}^c = R_{cr}^c + C_r^c C_p^r R_{ps}^p$$

C_e^c - is given by Eq. (3.9)

C_c^r - is given by Eq. (3.14)

C_r^p - will be given in Section 4

C_p^s - is given by Eq. (3.19) for the accelerometers and Eq. (3.20) for the gyros

$C_b^a = [C_a^b]^{-1} \equiv [C_a^b]^T$ for $a, b = e, c, r, p, s$. In other words, for all the C transformations between any two of the coordinate frames, the transformations are orthogonal, and, therefore, the matrix inverse is equal to the transpose [7].

Group 1 and Group 2 terms are defined as the desirable and undesirable terms, respectively, and will be discussed later in the text.

The applied acceleration equation provides the sensor component accelerations for the platform rate equation, Eq. (2.33), and the platform indicated acceleration equation, Eq. (2.34). The procedure for the platform rate equation is to obtain a solution of the applied acceleration for each of the three gyros.

$A_{i,SGX}^{SGX} = \{a_{IX}, a_{OX}, a_{SX}\}$ is obtained from Eq. (3.25) with
 $R_{ps}^p = R_{p,GX}^p$, reference Eq. (3.18),
 and $C_p^s = C_p^{SGX}$, reference Eq. (3.20).

$A_{i,SGY}^{SGY} = \{a_{IY}, a_{OY}, a_{SY}\}$ is obtained from Eq. (3.25) with
 $R_{ps}^p = R_{p,GY}^p$ and $C_p^s = C_p^{SGY}$.

$A_{i,SGZ}^{SGZ} = \{a_{IZ}, a_{OZ}, a_{SZ}\}$ is obtained from Eq. (3.25) with
 $R_{ps}^p = R_{p,GZ}^p$ and $C_p^s = C_p^{SGZ}$.

The procedure for the platform indicated acceleration equation is to obtain a solution of Eq. (3.25) for each of the three accelerometers.

$A_{i, \text{SAX}}^{\text{SAX}} = \{a_{\text{IAX}}, a_{\text{PX}}, a_{\text{OAX}}\}$ is obtained from Eq. (3.25) with
 $R_{\text{ps}}^{\text{P}} = R_{\text{p, AX}}^{\text{P}}$ and $C_{\text{p}}^{\text{S}} = C_{\text{p}}^{\text{SAX}}$,
reference Eq. (3.19).

$A_{i, \text{SAY}}^{\text{SAY}} = \{a_{\text{IAY}}, a_{\text{PY}}, a_{\text{OAY}}\}$ is obtained from Eq. (3.25) with
 $R_{\text{ps}}^{\text{P}} = R_{\text{p, AY}}^{\text{P}}$ and $C_{\text{p}}^{\text{S}} = C_{\text{p}}^{\text{SAY}}$.

$A_{i, \text{SAZ}}^{\text{SAZ}} = \{a_{\text{IAZ}}, a_{\text{PZ}}, a_{\text{OAZ}}\}$ is obtained from Eq. (3.25) with
 $R_{\text{ps}}^{\text{P}} = R_{\text{p, AZ}}^{\text{P}}$ and $C_{\text{p}}^{\text{S}} = C_{\text{p}}^{\text{SAZ}}$.

Note that the a_{OZ} terms are not used in Eq. (2.34); therefore, only the a_{IA} and a_{P} terms need to be determined.

Because the component solutions of the applied acceleration equation are embedded in the platform rate equations, a careful observation of the terms in Group 2 will show why this group is undesirable. The terms in Group 2 consist of platform rate, rate of change of platform rate (i.e., platform acceleration), and higher-order products and cross-products of the platform rate. Embedding these terms implies that the set of equations in Eq. (2.33) will be nonlinear, coupled, differential equations. These equations would have to be solved at least each cycle of the filtering process to obtain values for the platform rates. Fortunately, it will be shown in Sections 5 and 6 that these terms can be made negligible by limiting the magnitude of the commanded angular rate and/or using the commanded angular rate to decrease the platform rate contribution of the drift terms. Note that if all the inertial sensors were located precisely at the center of the inner platform, R_{ps}^{P} would be zero and all the

Group 2 terms would vanish; in fact, five terms in Group 1 would also vanish. However, since it is physically impossible to do this, the Group 2 terms must be evaluated to determine if their contribution can be neglected without affecting the accuracy of the error model coefficient estimates.

In the next section, the platform rate and indicated acceleration equations will be related to the state and measurement dynamic equations, followed by the development of the extended Kalman filter equations.

SECTION 4

EXTENDED KALMAN FILTER EQUATIONS

The platform rate and indicated acceleration equations developed over the last two sections will now be used to define the state and measurement equations. Once these equations are defined, the recursive filtering algorithm, which formulates the basis for the data reduction technique, will be developed from the extended Kalman filter equations.

Unfortunately, the rather laborious development of the platform Eqs. (2.33) and (2.34) was necessary to understand how one can obtain a prediction of the platform velocity to compare with the actual platform velocity measurement. As will be shown later, the difference between the actual and predicted measurement, called the measurement residual, is used to correct the filter in such a fashion that the estimates of the defined state variables will be "improved," assuming the actual measurements provide the best information available. A brief review of the development to this point will show which variables constitute the "state" of the calibration problem.

4.1 STATE VARIABLES

As mentioned in Section 1, the objective is to obtain estimates of inertial sensor error model coefficients. In the gyro performance model equation, Eq. (2.20), the bracketed term contains an expansion of the internal gyro error sources. This expansion is actually a mathematical error model that represents a general expression for those typical errors found during 14 years of gyro testing at Holloman AFB.

Preceding page blank

Which terms apply to a specific gyro depends on the physical structure and assembly of the gyro. Therefore, the first task is to identify the terms of the error model that represent the physical gyro error drifts. The second task is obviously to obtain estimates of the coefficients for those terms that are identified.

Sage [15] discusses one method of identifying parameters of a system, assuming you know the general structure of the system dynamic equations containing the parameters. It consists of defining the parameters as state variables and reformulating the problem as a state estimation problem. The form of the state estimation problem considered in this dissertation is shown in Figure 4.1. The system dynamic model contains the unknown error coefficients defined as state variables. The output $z(t)$ is a corrupted version of the state $x(t)$ due to the measurement noise $v(t)$. Assuming the statistics of the system disturbance $w(t)$ and measurement noise are known, we desire to determine a "best" estimate $\hat{x}(t)$ of the true system state $x(t)$ from a knowledge of $z(t)$.

Based on the above, the error model coefficients for all three gyros represented in Eq. (2.33) are designated as state variables. The commanded angular rate term of Eq. (2.20) is comprised of an unknown torquer scale factor times a known command torque t_g , shown in Eq. (2.33). The torquer scale factor of each gyro is defined as a state variable. The final gyro parameters defined as state variables are the misalignment angles given in Eq. (3.20) and represented explicitly in the platform rate equation and implicitly via the applied acceleration terms of Eq. (3.25), which are embedded in the platform

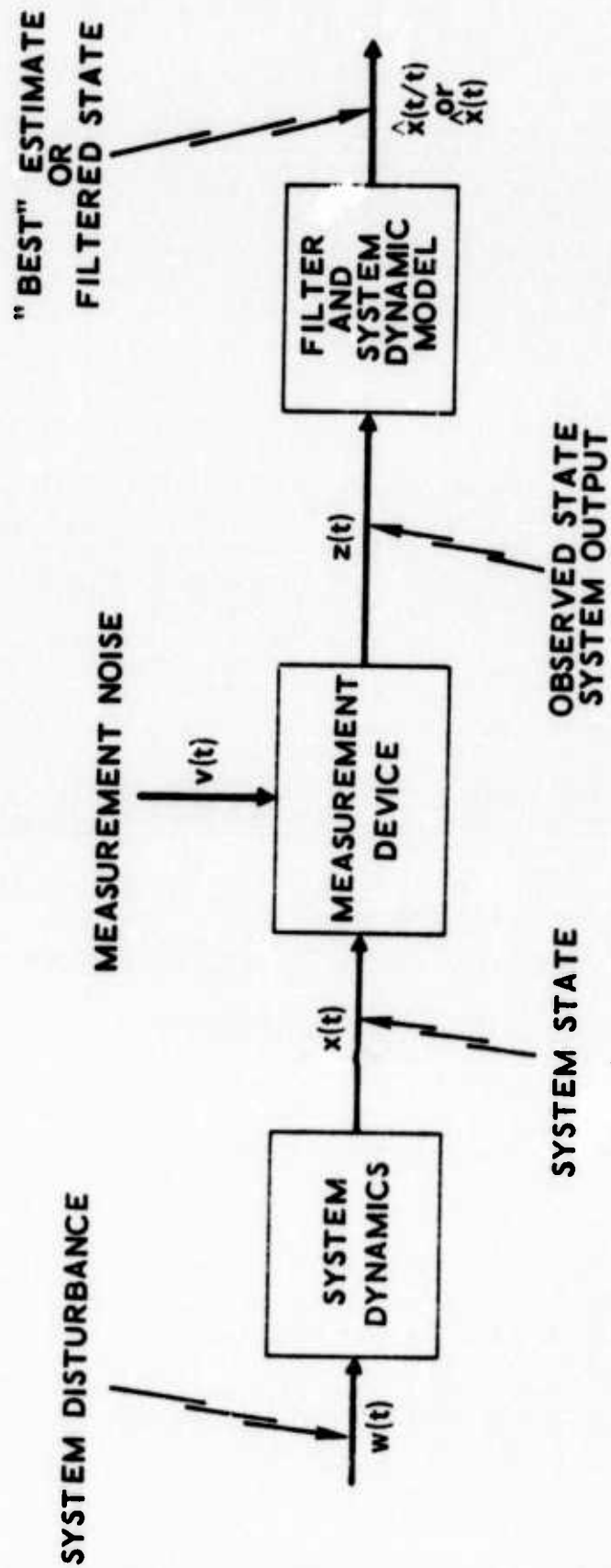


Figure 4.1. State Estimation Problem

rate equation. This implies that the platform rate equations are nonlinear functions of the state variables.

The same philosophy is used in designating accelerometer parameters as state variables. Equation (2.25) is a mathematical error model that represents 12 years of testing experience at Holloman AFB. Except for the a_I term, it is identical to the performance model given in Eq. (2.26). Consequently, the K coefficients for all three accelerometers represented in Eq. (2.34) are defined as state variables. In addition, the accelerometer misalignment angles defined in Eq. (3.19) and represented implicitly in Eq. (2.34) via the applied acceleration terms are designated state variables. Therefore, the platform acceleration equation is also a nonlinear function of the state variables.

To obtain a prediction of the platform velocity profile requires the knowledge of the inner platform angular position as a function of time. Since the platform rate equations are a function of the estimated states, the best we can do is to obtain an estimate of the platform angular position. Therefore, the last three state variables are the Euler angles α , β , and γ that track the inner platform motion with respect to the platform base (which was shown in Section 3.2.3 to be identical to the CRP frame). A list of the 63 states of the calibration process is given in Table 4.1.

Table 4.1. States of the Calibration Process

$X_1 = D_{FX}$	$X_{17} = D_{OOY}$	$X_{33} = TSF_Z$	$X_{49} = K_{3X}$
$X_2 = D_{FY}$	$X_{18} = D_{OOZ}$	$X_{34} = \eta_{x_i}$	$X_{50} = K_{3Y}$
$X_3 = D_{FZ}$	$X_{19} = D_{SSX}$	$X_{35} = \eta_{x_o}$	$X_{51} = K_{3Z}$
$X_4 = D_{IX}$	$X_{20} = D_{SSY}$	$X_{36} = \eta_{y_i}$	$X_{52} = K_{IPX}$
$X_5 = D_{IY}$	$X_{21} = D_{SSZ}$	$X_{37} = \eta_{y_o}$	$X_{53} = K_{IPY}$
$X_6 = D_{IZ}$	$X_{22} = D_{IOX}$	$X_{38} = \eta_{z_i}$	$X_{54} = K_{IPZ}$
$X_7 = D_{OX}$	$X_{23} = D_{IOY}$	$X_{39} = \eta_{z_o}$	$X_{55} = \psi_{x_i}$
$X_8 = D_{OY}$	$X_{24} = D_{IOZ}$	$X_{40} = K_{OX}$	$X_{56} = \psi_{x_o}$
$X_9 = D_{OZ}$	$X_{25} = D_{ISX}$	$X_{41} = K_{OY}$	$X_{57} = \psi_{y_i}$
$X_{10} = D_{SX}$	$X_{26} = D_{ISY}$	$X_{42} = K_{OZ}$	$X_{58} = \psi_{y_o}$
$X_{11} = D_{SY}$	$X_{27} = D_{ISZ}$	$X_{43} = K_{1X}$	$X_{59} = \psi_{z_i}$
$X_{12} = D_{SZ}$	$X_{28} = D_{OSX}$	$X_{44} = K_{1Y}$	$X_{60} = \psi_{z_o}$
$X_{13} = D_{IIX}$	$X_{29} = D_{OSY}$	$X_{45} = K_{1Z}$	$X_{61} = \alpha$
$X_{14} = D_{IIY}$	$X_{30} = D_{OSZ}$	$X_{46} = K_{2X}$	$X_{62} = \beta$
$X_{15} = D_{IIZ}$	$X_{31} = TSF_X$	$X_{47} = K_{2Y}$	$X_{63} = \gamma$
$X_{16} = D_{OOX}$	$X_{32} = TSF_Y$	$X_{48} = K_{2Z}$	

4.2 SYSTEM DYNAMIC MODEL

The system dynamic model consists of a set of Euler rate equations that describe the motion of the inner platform during the calibration process. Since the motion of the platform is unconstrained, large angle transformations are involved, which implies that the order of rotation must be specified. The sequence of rotations, shown in Figure 4.2, which give the orientation of the inner platform frame p with respect to the CRP frame r , is (α, β, γ) about the moving frame (x, z, y) axes respectively. From Figure 4.2, the orthogonal Euler transformation from the r to p frame is

$$C_r^p = \begin{bmatrix} E_{11} & E_{12} & E_{13} \\ E_{21} & E_{22} & E_{23} \\ E_{31} & E_{32} & E_{33} \end{bmatrix} \quad (4.1)$$

where

$$E_{11} = \cos \gamma \cos \beta$$

$$E_{12} = \cos \gamma \sin \beta \cos \alpha + \sin \gamma \sin \alpha$$

$$E_{13} = \cos \gamma \sin \beta \sin \alpha - \sin \gamma \cos \alpha$$

$$E_{21} = -\sin \beta$$

$$E_{22} = \cos \beta \cos \alpha$$

$$E_{23} = \cos \beta \sin \alpha$$

$$E_{31} = \sin \gamma \cos \beta$$

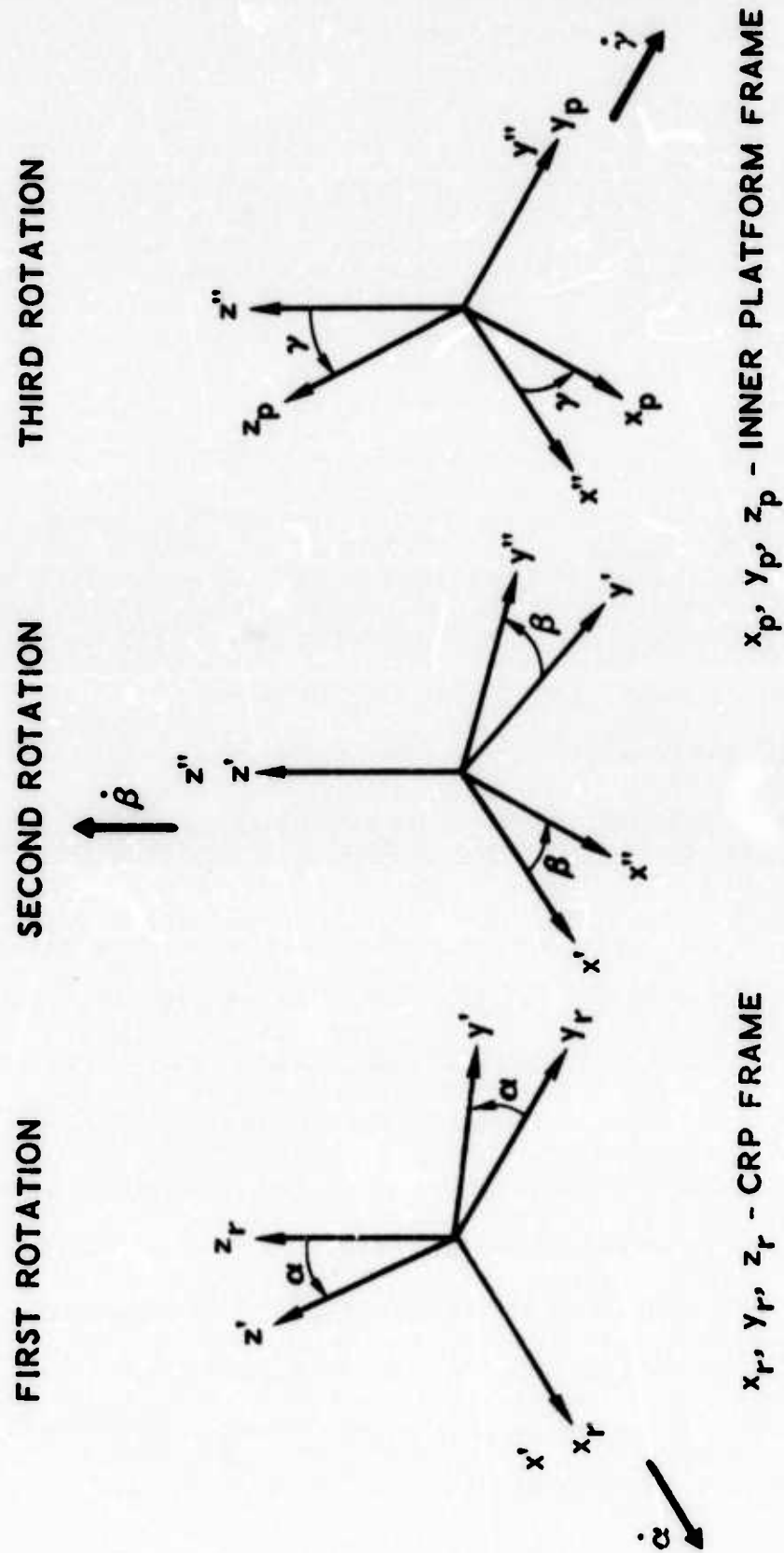


Figure 4.2. Euler Transformation

$$E_{32} = \sin \gamma \sin \beta \cos \alpha - \cos \gamma \sin \alpha$$

$$E_{33} = \sin \gamma \sin \beta \sin \alpha + \cos \gamma \cos \alpha$$

The platform rates are a function of the gyro states, reference Eq. (2.33), implying that, if the Euler rate equations are a function of the platform rate, then the Euler angles will represent the drift generated by the gyro states at any point in time. Now the applied acceleration terms contained in Eq. (2.34) are a function of the Euler angles via the C_r^P transformation in Eq. (3.25). Consequently, the gyro states are represented in the measurement process. As shown by Figure 4.1, the system output $z(t)$, which is the measurement equation, must be a function of the system states as a minimum criterion for the system to be observable [16]. However, just because the states are represented in the measurement process does not imply that the system will be observable. If the measurement information is such that the filtering process has difficulty distinguishing between the states, then we say that the states (which will be shown to be random variables in the next section) are highly correlated and therefore the system by definition is unobservable [16]. Because of the concern for this observability problem, a careful evaluation was made of the filtering process during the simulations that are described in Sections 5 and 6. One significant discovery that was made during the simulations was that the system observability could be monitored quite effectively by determining the level of correlation that existed between the Euler angle states. It was found that command torquing was very effective in offsetting the effect of the unobservability condition.

Based on the above, we now seek an expression for the Euler rate as a function of platform rate. Referring to Figure 4.2, we resolve the Euler rates into the inner platform frame p. The matrix form of the resulting resolution is

$$\begin{bmatrix} \omega_{xp} \\ \omega_{yp} \\ \omega_{zp} \end{bmatrix} = \begin{bmatrix} \cos \gamma \cos \beta & -\sin \gamma & 0 \\ -\sin \beta & 0 & 1 \\ \sin \gamma \cos \beta & \cos \gamma & 0 \end{bmatrix} \begin{bmatrix} \dot{\alpha} \\ \dot{\beta} \\ \dot{\gamma} \end{bmatrix} \quad (4.2)$$

Solving the matrix expression for the Euler rate equations gives

$$\begin{aligned} \dot{\alpha} &= (\omega_{xp} \cos \gamma + \omega_{zp} \sin \gamma) / \cos \beta \\ \dot{\beta} &= \omega_{zp} \cos \gamma - \omega_{xp} \sin \gamma \\ \dot{\gamma} &= (\omega_{xp} \cos \gamma \sin \beta + \omega_{zp} \sin \gamma \sin \beta) / \cos \beta + \omega_{yp} \end{aligned} \quad (4.3)$$

where the Euler angles are limited to the following ranges to avoid the singularity that occurs when $\beta = \pm 90^\circ$.

$$0 \leq \alpha < 2\pi$$

$$-\frac{\pi}{2} < \beta < \frac{\pi}{2}$$

$$0 \leq \gamma < 2\pi$$

Since the initial value of the Euler angles (i. e., at $t = 0$) represents the small misalignments of the inner platform with respect to the CRP frame, a Euler rotation sequence that provided a cosine term in the

denominator of Eq. (4.3), rather than a sine term, was selected. We can see that another reason for command torquing the platform is to prevent β from reaching the singularity condition. We now have all the equations necessary to define the state and measurement equations for the calibration process.

4.3 STATE AND MEASUREMENT EQUATIONS

A "technical battle" is presently being waged in the literature concerning the proper choice of a statistical model or models for gyro and accelerometer error coefficients [4, 5, 6]. Unfortunately, the classical Gauss-least-squares approach, which has no probabilistic meaning, was used for a number of years to obtain data from inertial sensors. As discussed by Jazwinski [17], there is no need to make any assumptions about the system noise, since the problem is one of minimizing deterministic errors in the least-squares approach. With the advent of Kalman filter applications, a statistical description was required for the system disturbance and measurement noise (Reference Figure 4.1) in addition to the initial value of the state $x(t_0)$. Consequently, for the last 6 years, a major effort has been made to determine a proper choice for the error coefficient models.

Since the objective of this report is to provide a general data reduction algorithm for testing an Inertial Navigation System on the centrifuge, a general statistical model was selected for the first 60 states shown in Table 4.1. The important point is that to properly apply the data reduction algorithm, an analysis of component test data should be made so that the general statistical model employed in this report can be modified to represent the actual platform

sensors being tested. Sutherland and Gelb [4] found that a random constant in combination with a random walk provided a good description of gyro drift and an adequate description for the accelerometer terms. A random constant is represented by the following stochastic differential equation

$$\dot{\mathbf{x}}(t) = 0 \quad (4.4)$$

where $\mathbf{x}(t_0)$ is a random variable. A random walk is represented by

$$\dot{\mathbf{x}}(t) = \mathbf{w}(t) \quad (4.5)$$

where $\mathbf{w}(t)$ is a random process and $\mathbf{x}(t_0) \equiv 0$. Combining Eqs. (4.4) and (4.5), the statistical model assumed for the first 60 states is represented by the following scalar, stochastic differential equation:

$$\dot{x}_i(t) = w_i(t) \quad [i = 1, 2, \dots, 60] \quad (4.6)$$

where

$x_i(t_0)$ - is a gaussian random variable representing the initial value of the i th state with mean $\bar{x}_i(t_0) \equiv x_{0i} = E \{x_i(t_0)\}$ and variance $\sigma_{x_{0i}}^2 = p_{0i} = E \{[x_i(t_0) - x_{0i}]^2\}$

$E \{ \}$ - is the expectation operator

$\{w_i(t), t \geq t_0\}$ - is a zero mean, gaussian white process (i.e., time uncorrelated) representing the i th state disturbance with covariance

$$c_{w_i}(t, \tau) = E \{w_i(t)w_i(\tau)\} = \sigma_{w_i}^2 \delta(t - \tau)$$

$\delta(t - \tau)$ - is the Dirac delta function

$$E \left\{ \left[x_i(t_0) - x_{0i} \right] \left[w_i(t) \right] \right\} = 0 \quad \left[\text{i.e., the initial state, } x_i(t_0) \text{ is independent of the disturbance process } w_i(t) \right]$$

The scalar equations for the last three states of Table 4.1 (representing the Euler angles) contain the system dynamic expressions of Eq. (4.3). The statistical model for these states is represented by the following set of nonlinear, stochastic differential equations.

$$\begin{aligned} \dot{x}_{61}(t) &= \left[\left\{ \omega_{xp}(x) \cos [x_{63}(t)] + \omega_{zp}(x) \sin [x_{63}(t)] \right\} / \right. \\ &\quad \left. \cos [x_{62}(t)] \right] + w_{61}(t) \\ \dot{x}_{62}(t) &= \left\{ \omega_{zp}(x) \cos [x_{63}(t)] - \omega_{xp}(x) \sin [x_{63}(t)] \right\} \\ &\quad + w_{62}(t) \end{aligned} \quad (4.7)$$

$$\begin{aligned} \dot{x}_{63}(t) &= \left[\left\{ \omega_{xp}(x) \cos [x_{63}(t)] \sin [x_{62}(t)] \right. \right. \\ &\quad \left. \left. + \omega_{zp}(x) \sin [x_{63}(t)] \sin [x_{62}(t)] \right\} / \right. \\ &\quad \left. \cos [x_{62}(t)] + \omega_{yp}(x) \right] + w_{63}(t) \end{aligned}$$

where

$\omega_{xp}(x)$, $\omega_{yp}(x)$, $\omega_{zp}(x)$ - are obtained from Eq. (2.33) with the variables of Table 4.1 replaced by their associated state variable designations (i.e., $D_{FX} = x_1$ etc.)

$x_{61}(t_0), x_{62}(t_0), x_{63}(t_0)$ - are gaussian random variables representing the initial values of the Euler angles with mean x_{0j} and variance $\sigma_{x_{0j}}^2$ ($j = 61, 62, 63$)

$w_{61}(t), w_{62}(t), w_{63}(t)$ - are zero mean, gaussian white processes representing the j th state disturbance with covariance $\sigma_{w_j}^2 \delta(t - \tau)$ ($j = 61, 62, 63$)

$w_j(t)$ and $x_j(t_0)$ are independent

Combining Eqs. (4.6) and (4.7) gives the following state vector equation for the calibration program.

$$\dot{\underline{x}} = \underline{f}(\underline{x}, t) + \underline{w}(t) \quad (4.8)$$

where

$\dot{\underline{x}}$ - is a 63-element vector of the state derivatives

$\underline{w}(t)$ - is a 63-element disturbance vector

$\underline{f}(\underline{x}, t)$ - is a 63-dimensional vector-valued, nonlinear, function of the state

$\{\underline{w}(t), t \geq t_0\}$ - is a zero mean, gaussian white, vector, disturbance process

$$E \left\{ \underline{w}(t) \underline{w}^T(\tau) \right\} = Q(t) \delta(t - \tau)$$

$Q(t)$ - is a (63×63) covariance matrix of the disturbance process containing the $\sigma_{w_i}^2$ elements

$E \{ \underline{x}(t_0) \} = \underline{x}_0$ - is a 63-element mean value initial state vector containing the x_{0i} elements

$$E \left\{ [\underline{x}(t_0) - \underline{x}_0][\underline{x}(t_0) - \underline{x}_0]^T \right\} = P_0$$

P_0 - is a (63×63) covariance matrix of the initial state vector containing the $\sigma_{x_{0i}}^2$ elements

$$E \left\{ \underline{w}(t) [\underline{x}(t_0) - \underline{x}_0]^T \right\} = \underline{0} \text{ for all } t \geq t_0$$

$\underline{0}$ - is a 63-element null vector since the initial state $\underline{x}(t_0)$ is independent of the disturbance process $\underline{w}(t)$

The first 60 elements of $\underline{f}(\underline{x}, t)$ are zero, as can be seen from Eq. (4.6); the last 3 elements are the dynamic expressions on the right-hand side of the set of equations given in Eq. (4.7).

It is important to understand the relationship between the selected state statistical model and the physical parameters of the Inertial Navigation System. The first 60 initial state random elements, $x_i(t_0)$, usually represent the variations that occur in the sensor error coefficients, the sensor true input axis location, and the sensor torquer scale factor between the time that the sensor is turned off and the time it is turned back on. These random changes in the values of the sensor variables between turn off and turn on are referred to as the sensor's repeatability. In other words, it has been determined from sensor tests that the values of the error coefficients, input axis misalignment angles, and torquer scale factor are different each time the sensor is activated. An analysis of large amounts of sensor test data at the Holloman facility reveals that this lack of repeatability can be adequately described by a gaussian probability law. Once the sensor is operating, random changes in the internal mechanism of the sensor and the sensor feedback loop, which are believed to come from sources independent of those causing the repeatability problem, are represented by the gaussian white

disturbance process, $w(t)$. The assumption of a gaussian distribution for the random operating changes is again based on an analysis of sensor data. The assumptions that the disturbance is white (uncorrelated in time) and independent of the repeatability sources are difficult to justify physically, simply because not enough is known about the complex internal and external mechanisms that generate the disturbances. This is one subject presently under technical debate. The importance of these assumptions will be shown later. This is one area that a careful analysis of the sensor data should be made to determine, if possible, whether the statistical model as proposed is an adequate approximation for the physical sensors being tested. For example, if the disturbance process is determined to be time-correlated, there are techniques discussed by Meditch [16] and Jazwinski [17] that resolve the problem by augmenting the state vector. Augmenting the state vector (which already contains 63 elements), for each sensor variable found to have a time-correlated disturbance, could increase the complexity of the problem tremendously. The questions now are how much improvement in filter performance will be obtained and does the improvement warrant the increased complexity? As is the case in many physical problems, a simulation may show that the simpler model is an adequate approximation for the level of accuracy desired in the state estimates.

In the calibration problem, the first 60 initial state elements represent a slightly different initial condition; since in the calibration procedure, the system has been operating for quite some time prior to the start of the system calibration at time $t = t_0$. For instance, in

the centrifuge test, the initial condition does not occur until the centrifuge is stabilized at a selected g-level, and a new initial condition is established for each additional g-level specified as part of the total test sequence. Hence, the initial condition state for the calibration problem is actually a combination of the repeatability effect plus the operating disturbance input up to the time when $t = t_0$. Equation (4.6) shows that the state process $x(t)$ is a linear combination of two gaussian variables. Since the mean value of $w(t)$ is zero, the mean value of $x(t)$ at any point in time will be equal to the mean value generated by the repeatability effect. The variance of $x(t)$ is simply the sum of the variance due to the repeatability effect plus the operating disturbance, since the variance of a sum of two independent random variables equals the sum of their respective variances [18].

$$\sigma_x^2 = \sigma_{x_0}^2 + \sigma_w^2 \quad (4.9)$$

Consequently, for the calibration problem, the statistical model can represent the initial condition states of the first 60 state variables simply by adjusting the variance to include the input disturbance up to the time when $t = t_0$. The importance of the independence and gaussian white assumptions can now be realized, since correlation in the disturbance process or between the two variables would complicate the modeling effort.

The initial value of the last three Euler states described in Eq. (4.7) represents the inner platform misalignments with respect to the CRP frame. These can be described by a gaussian distribution about a mean initial value, since the normal procedure for the system

calibration is to align and level the platform via a standard gyrocompass technique [2, 10]. The mean value represents the nominal misalignments that occur at the conclusion of the gyrocompass procedure, and the variation occurs due to the system mechanization uncertainties. In the case of the centrifuge operating test, the platform alignment is maintained and reestablished at each g-level by caging the platform gimbals [10]. Caging is accomplished by switching the input to the stabilization loops from the gyros to the gimbal synchros and resolvers. The stabilization loops use the signals from the resolvers to drive the gimbals until the synchros reach their electrical null positions, which correspond roughly, through physical alignment of the synchros, to an alignment with the platform base mounting frame. The mean value and variations occur via the caging procedure. The operating disturbance represents the random variations associated with the noise generated over the small operating range of the driver amplifiers contained in the stabilization loops.

Before proceeding to the measurement equation, one final comment is required concerning the formality of Eq. (4.8). In Chapter 3 of Jazwinski [17], an outstanding discussion is given, showing that, since the sample functions of $\underline{w}(t)$ are a function of the Dirac delta function [i. e., $\underline{w}(t)$ is delta-correlated], $\underline{w}(t)$ is not Riemann integrable in the mean square sense. Therefore, Eq. (4.8) has no mathematical meaning as it is presently defined, since the equation can not be integrated to obtain a solution for $\underline{x}(t)$. However, as shown by Jazwinski, gaussian white noise is the formal derivative of independent Brownian motions. A formal representation of the stochastic

differential equation is

$$d\underline{x}(t) = \underline{f}(\underline{x}, t)dt + d\underline{\lambda}(t) \quad (4.10)$$

where

$\{\underline{\lambda}(t), t \geq t_0\}$ - is a vector process of independent Brownian motions

The first term on the right-hand side of Eq. (4.10) can be integrated in the mean square sense or via an ordinary integral for the sample functions of $\underline{x}(t)$. Integration of the second term can not be defined for the sample functions because of the erratic properties of Brownian motion. However, integration of the second term has been defined in a mean square sense by Itô and is called the Itô stochastic integral. Hence, a solution of $\underline{x}(t)$ can be obtained in the mean square sense with the formal equation. So that equations that contain gaussian white processes are integrable, the gaussian white process is always assumed formally related to the independent Brownian motion process $\{\underline{\lambda}(t), t \geq t_0\}$. In other words, $\underline{w}(t)$ is formally related to the Brownian process as:

$$\underline{w}(t) \sim \frac{d\underline{\lambda}(t)}{dt} \quad (4.11)$$

The measurement equation is based on the platform acceleration model, Eq. (2.34).

$$\underline{a}_{\text{IND}} = \underline{h}(\underline{x}, t) + \underline{m}(t) \quad (4.12)$$

where

$\underline{a}_{\text{IND}}$ - is a 3-element indicated acceleration vector

$\underline{h}(\underline{x}, t)$ - is a 3-dimensional vector-valued, nonlinear, function of the state

$\underline{m}(t)$ - is a 3-element measurement noise vector

The function $\underline{h}(\underline{x}, t)$ is obtained from Eq. (2.34) with the variables of Table 4.1 replaced by their associated state variable designations. The actual INS measurements are the velocity change over the interval between measurements. A first-order approximation of the vector velocity, using Eq. (4.12) as the rate of change in velocity, gives:

$$\underline{v}(t + \Delta t) - \underline{v}(t) = \Delta \underline{v} = \underline{h}(\underline{x}, t) \Delta t + \underline{m}(t) \Delta t \quad (4.13)$$

where

Δt - is the time interval between measurements

$\Delta \underline{v}$ - is the 3 element vector velocity change over the measurement interval

Since the measurements are obtained at discrete time points (t_n , $n = 1, 2, 3, \dots$), the discrete form of Eq. (4.13) gives the final version of the measurement equation for the calibration problem.

$$\Delta \underline{v}(t_n) = \underline{h}[\underline{x}(t_n), t_n] \Delta t + \underline{m}(t_n) \Delta t \quad (4.14)$$

where

Δt - is the time between the $(n-1)$ th and n th measurements,
 $\Delta t = t_n - t_{n-1}$

$\{\underline{m}(t_n), n = 1, 2, 3, \dots\}$ - is a zero mean, gaussian white,
 vector, measurement noise sequence

$E \{\underline{m}(t_n) \Delta t\} = \underline{0}$ for all values of $n = 1, 2, 3, \dots$, since $\underline{m}(t_n)$
 is a zero mean sequence

$E \left\{ \underline{m}(t_j) \Delta t \underline{m}^T(t_n) \Delta t \right\} = (\Delta t)^2 R(t_n) \delta_{jn}$ for all $j, n = 1, 2, 3, \dots$

$R(t_n)$ - is the (3×3) covariance matrix for the measurement
 noise sequence

$\delta_{jn} = \begin{cases} 0 & \text{for } j \neq n \\ 1 & \text{for } j = n \end{cases}$ is the Kronecker delta

$E \left\{ [\underline{x}(t_0) - \underline{x}_0] [\underline{m}(t_n)]^T \right\} = \underline{0}$ for all $n = 1, 2, 3, \dots$ since $\underline{m}(t_n)$
 is assumed independent of $\underline{x}(t_0)$

$E \left\{ [\underline{w}(t_j)] [\underline{m}(t_n)]^T \right\} = \underline{0}$ for all $j, n = 1, 2, 3, \dots$ since $\underline{m}(t_n)$ is
 assumed independent of $\underline{w}(t_j)$

The accelerometers in the system have their own feedback loops, referred to as "capture loops," since they "capture" the pendulous element and prevent it from rotating too far from the null position. The initial state and state disturbance variations, discussed in conjunction with the state equation, are generated in the internal mechanisms of the accelerometer and its capture loop. The output of the accelerometer is a series of Δv pulses that are processed and counted in the system computer circuitry. The measurement noise sequence is related to the electronic noise generated in the system processing loop that eventually becomes the system output velocity change.

Consequently, the assumption that the noise sequence is independent of the disturbance and initial state variations is justified, since there is no physical dependence between the gyro and accelerometer circuitry and the system output processing circuitry. The assumption of zero mean gaussian noise is based on an analysis of system output data. The assumption of white noise is based on the reasoning that there should not be any relationship between random electronic noise and the sequence of measurements being processed through the circuitry.

The past reference to the measurement "dynamic" equations can now be understood, since the function $\underline{h}(\underline{x}, t)$ contains the dynamics of the velocity measurement trajectory. It will be shown in the next section, that the rather rough first-order approximation used to obtain the Δv form of the measurement equation has a minimal impact on the filtering process since the only area where the approximation is used is in the computation of the filter gain matrix.

With the state and measurement equations defined, we can now proceed to develop the extended Kalman filter equations that constitute the filtering algorithm, which in turn completes the requirements for the data reduction problem.

4.4 EXTENDED KALMAN FILTER EQUATIONS AND FILTERING ALGORITHM

We start the development of the filter equations with the given nonlinear state equation, which is repeated below.

$$\dot{\underline{x}}(t) = \underline{f}(\underline{x}, t) + \underline{w}(t) \quad (4.8)$$

Keeping in mind that the following equations are vector expressions, we will drop the sub-bar notation, \underline{x} , as a matter of notational convenience. We linearize Eq. (4.8) about a reference or nominal trajectory, where the nominal value of the state is set equal to the filtered estimate. The filtered estimate, $\hat{x}(t|t)$, is defined as the "best" estimate of the state $x(t)$ based on measurements taken up to time "t". In the case of a linear state equation, it is well known [16] that the filtered estimate is an optimal estimate, since the Kalman filter process, which generates the estimate, minimizes the variance of the filtering error. The filtering error, $\tilde{x}(t|t)$, is the difference between the true value of the state and the filtered estimate.

$$\tilde{x}(t|t) = x(t) - \hat{x}(t|t) \quad (4.15)$$

In the case of a nonlinear state equation, the filtered estimate is optimal only with respect to the linearized equation. Whether the estimate is good or "best" with respect to the nonlinear state equation depends on the validity of the linearization.

The reference trajectory is a deterministic trajectory obtained by setting $w(t)$ to zero in Eq. (4.8) and the nominal value of the state, $x_{\text{nom}} = \hat{x}(t|t)$. Therefore,

$$\frac{d\hat{x}(t|t)}{dt} = f[\hat{x}(t|t), t] \quad t \geq t_0 \quad (4.16)$$

is the equation of the reference trajectory. We define the deviation from the reference trajectory as

$$\delta x(t) \triangleq x(t) - \hat{x}(t|t) \quad (4.17)$$

Comparing Eqs. (4.15) and (4.17), we see that the deviation is equivalent to the filtering error.

Differentiating Eq. (4.17) and substituting the expressions contained in Eqs. (4.8) and (4.16) gives

$$\frac{d\delta x}{dt} = f(x,t) - f[\hat{x}(t|t),t] + w(t) \quad (4.18)$$

If the deviations from the reference trajectory are small so that the higher-order terms can be neglected, a Taylor series expansion about the nominal filtered estimate gives

$$f(x,t) - f[\hat{x}(t|t),t] \cong F[\hat{x}(t|t),t] \delta x(t) \quad (4.19)$$

where

$$F[\hat{x}(t|t),t] \triangleq \left[\frac{\partial f_i[\hat{x}(t|t),t]}{\partial x_j} \right] \quad i, j, = 1, 2, \dots, 63$$

is a (63×63) matrix of partial derivatives of the elements of $\underline{f}(x,t)$, evaluated at $\hat{x}(t|t)$, with respect to each state variable x_j . Substituting the approximation of Eq. (4.19) into Eq. (4.18), we obtain a linear

perturbation equation that is valid for "small" deviations about the reference trajectory.

$$\frac{d\delta x}{dt} = F[\hat{x}(t|t), t] \delta x(t) + w(t) \quad (4.20)$$

Since the measurements are discrete, we discretize Eq. (4.20) so that we can develop the filter equations using the discrete form of the Kalman filter. It is a personal preference to compute the solution via the state transition matrix, rather than solving the matrix Riccati equation to obtain the filtering error covariance matrix as required in the continuous filter procedure [16]. Therefore, discretizing and integrating Eq. (4.20) over the time interval $[t_{n-1}, t_n]$ gives the following discrete solution to the perturbation equation.

$$\delta x(t_n) = \Phi[t_n, t_{n-1}; \hat{x}(t_{n-1} | t_{n-1})] \delta x(t_{n-1}) + D(t_{n-1}) \quad (4.21)$$

where

$$D(t_{n-1}) = \int_{t_{n-1}}^{t_n} \Phi[t_n, \tau; \hat{x}(t_{n-1} | t_{n-1})] w(\tau) d\tau$$

$\Phi[t_n, t_{n-1}, \hat{x}]$ - is the state transition matrix [16]

The state transition matrix is obtained by solving the following matrix differential equation.

$$\dot{\Phi}[t, t_{n-1}; \hat{x}(t_{n-1} | t_{n-1})] = F[\hat{x}(t_{n-1} | t_{n-1}), t] \Phi[t, t_{n-1}; \hat{x}(t_{n-1} | t_{n-1})] \quad (4.22)$$

$$t_{n-1} \leq t \leq t_n$$

The initial condition for the matrix differential equation is

$$\Phi(t_{n-1}, t_{n-1}; \hat{x}(t_{n-1} | t_{n-1})) = I \quad (4.23)$$

where

I — is a (63 x 63) identity matrix

The relationship between Eqs. (4.22) and (4.21) should be clearly understood. The purpose of the transition matrix is to transform the perturbation states, $\delta x(t_{n-1})$, along the reference trajectory from time point t_{n-1} to time point t_n . Hence, as shown by Eq. (4.23), the transition matrix would logically be the identity matrix at time t_{n-1} . In the perturbation solution equation, Eq. (4.21), we see that the value of Φ is at the final time t_n , since getting a solution requires that the previous value of the perturbation states $\delta x(t_{n-1})$ be transformed along with the system disturbance to the solution point at time t_n . Transforming the perturbation states along the reference trajectory implies that Φ must be a function of the perturbation dynamics; Eq. (4.22) verifies this by the F matrix of partials. Equation (4.22) represents the set of dynamic equations that permit each element of the transition matrix to be determined at any time t over the closed interval $[t_{n-1}, t_n]$. Therefore, Eq. (4.22) is used to obtain the elements of Φ , evaluated at time t_n , for solving Eq. (4.21).

Solving Eq. (4.22) appears to be a formidable task, since Φ contains 3969 elements. Fortunately, this is not the case, since the maximum number of differential equations will be 189. The reason is

that the first 60 elements of $\underline{f}(\underline{x}, t)$ are zero; therefore, the first 60 rows of F will be zero. Assuming each element of the last three rows of F will contain nonzero partials, the maximum number of equations would be 3 times 63 or 189.

It will be shown in Section 6 that the reason F , and therefore Φ , is a function of time is due to the applied acceleration being a function of time for the operating centrifuge test. In the case of the 1-g calibration in the local gravitational field, the F matrix is constant since g is constant. Meditch [16] shows that for a constant F matrix, Φ can be determined using the matrix exponential.

$$\begin{aligned}\Phi[t_n, t_{n-1}; \hat{x}(t_{n-1} | t_{n-1})] &= \exp\{F(t_n - t_{n-1})\} \\ &= I + F(t_n - t_{n-1}) + \dots + \frac{F^m(t_n - t_{n-1})^m}{m!} + \dots\end{aligned}$$

but $t_n - t_{n-1} \equiv \Delta t$, so

$$\Phi[t_n, t_{n-1}; \hat{x}(t_{n-1} | t_{n-1})] = I + F \Delta t + F^2 \frac{(\Delta t)^2}{2!} + \dots + \frac{F^m (\Delta t)^m}{m!} + \dots \quad (4.24)$$

where

I - is a (63×63) identity matrix

$F = F[\hat{x}(t_{n-1} | t_{n-1})]$ is a constant matrix

$\exp\{x\} \equiv e^x$ is the exponential function

The number of terms in the Φ series is obviously a function of the time between measurements Δt and the desired accuracy of Φ . A computer solution of Eq. (4.24) is definitely computationally more efficient than solving the set of differential equations of Eq. (4.22) for the time-varying Φ case. The centrifuge simulation of Section 6 reveals that the filtered estimates obtained by assuming that F was constant over Δt , and thereby permitting Eq. (4.24) to be used, were just as good as those obtained by determining Φ via Eq. (4.22).

The disturbance sequence $w(t_{n-1})$ of Eq. (4.21) can be considered as a piecewise constant function of time for the measurement intervals (which range from 0.02 to 1.0 second) of the calibration problem. Therefore, the $D(t_{n-1})$ term can be simplified to

$$D(t_{n-1}) = \Gamma[t_n, t_{n-1}; \hat{x}(t_{n-1} | t_{n-1})] w(t_{n-1}) \quad (4.25)$$

where Γ is defined as

$$\Gamma[t_n, t_{n-1}; \hat{x}(t_{n-1} | t_{n-1})] \triangleq \int_{t_{n-1}}^{t_n} \Phi[t_n, \tau; \hat{x}(t_{n-1} | t_{n-1})] d\tau \quad (4.26)$$

Note that the right-hand side of Eq. (4.26) reveals that we need to solve for Φ from t_n back to t_{n-1} . In other words, Φ must be solved backward in time. Hsu and Meyer [19] show that a solution of Φ backward in time can be obtained using the adjoint system equation. Hence, Φ from t_n back to t_{n-1} is obtained from the following adjoint, matrix differential equation.

$$\Phi[t_n, t; \hat{x}(t_{n-1}|t_{n-1})] = \Phi[t_n, t; \hat{x}(t_{n-1}|t_{n-1})] F[t, \hat{x}(t_{n-1}|t_{n-1})] \quad (4.27)$$

The initial condition for the adjoint equation is

$$\Phi[t_n, t_n; \hat{x}(t_{n-1}|t_{n-1})] = I \quad (63 \times 63) \text{ identity matrix} \quad (4.28)$$

With $\Phi(t_n, t, \hat{x})$ determined from Eq. (4.27), we substitute Φ into Eq. (4.26) to get Γ .

Equation (4.27) reveals that since Φ premultiplies F , the fact that F has 60 rows of zero elements does not help reduce the number of differential equations. Assuming the last three rows of F contain nonzero partials, Eq. (4.27) will generate 3969 equations. Fortunately, the assumption that F is constant over Δt (based on the centrifuge simulation results of Section 6) permits Γ to be determined by substituting the exponential series of Φ , from Eq. (4.24), into Eq. (4.26). The substitution results in the following series expression for Γ , when F is a constant matrix.

$$\Gamma[t_n, t_{n-1}, \hat{x}(t_{n-1}|t_{n-1})] = I \Delta t + F \frac{(\Delta t)^2}{2!} + \dots + F^m \frac{(\Delta t)^{m+1}}{(m+1)!} + \dots \quad (4.29)$$

The discrete solution to the linear perturbation equation, Eq. (4.21), can now be written as

$$\begin{aligned} \delta x(t_n) = & \Phi[t_n, t_{n-1}; \hat{x}(t_{n-1}|t_{n-1})] \delta x(t_{n-1}) + \Gamma[t_n, t_{n-1}; \hat{x}(t_{n-1}|t_{n-1})] \\ & \times w(t_{n-1}) \end{aligned} \quad (4.30)$$

where \times represents the matrix product of Γ and w .

We now develop the linear perturbation equation for the nonlinear measurement equation, repeated below.

$$\Delta v(t_n) = h[x(t_n), t_n] \Delta t + m(t_n) \Delta t \quad (4.14)$$

The approach is similar to that used for the nonlinear state equation except that slight modifications must be made, since Eq. (4.14) is an approximation. As with the state equation, we first need an expression for the nominal or reference measurement trajectory. Since it is a deterministic trajectory, we set the measurement noise sequence $m(t_n)$ to zero and select a nominal value for the state $x_{nom}(t_n)$.

$$\Delta v(t_n) = h[x_{nom}(t_n), t_n] \Delta t \quad (4.31)$$

The question now is: what should the nominal state be for the reference measurement trajectory?

To help answer this question, let us regress in order to understand the selection that was made for the state equation. Expressing Eq. (4.16) as a general form of the reference state trajectory gives

$$\frac{d x_{nom}(t)}{dt} = f[x_{nom}(t), t] \quad (4.32)$$

Any solution to the nonlinear differential equation could be used as a reference trajectory. In the case of an arbitrary nonlinear differential equation, the existence and uniqueness of solutions remain open questions. When the structure of the function $f[x(t), t]$ satisfies a Lipschitz condition, then there exists a unique trajectory through each

point in state space. Assume that we select $x_{nom}(t)$ as the solution through the initial a priori estimate $\hat{x}(t_0)$. Then, at later times it is possible that the perturbations

$$\delta x(t) = x(t) - x_{nom}(t) \quad (4.33)$$

could get excessively large. Since the linearized equations that form the basis for the Kalman filtering process are only valid for small perturbations about the $x_{nom}(t)$ we have chosen, the filtering process for the actual system would be at best inefficient, assuming it was stable. More than likely, the nonlinearities that were neglected during linearization would cause the filter to diverge.

It now becomes obvious that the best selection would be to base the value of $x_{nom}(t)$ on the measurement data; so that the reference trajectory is actually being constructed, as the problem develops, based on the latest measurement information available. What we have just described is the estimate produced by a Kalman filter. The filtered estimate $\hat{x}(t_{n-1} | t_{n-1})$ is the "best" estimate of the state at time t_{n-1} , based on measurements taken up to time t_{n-1} .

In the case of the measurement equation, Eq. (4.14), we see that we need the state at the end time, t_n , or the time of the next measurement. Hence, we need to project our best knowledge of the state forward in time. The best "predicted" estimate would be the value of the state at time t_n that lies on the reference trajectory. We use the state reference trajectory equation, Eq. (4.32), to determine the predicted estimate of the state at time t_n based on the measurements

up to time t_{n-1} ; in other words, $x_{nom}(t) \triangleq \hat{x}(t_n | t_{n-1})$. $\hat{x}(t_n | t_{n-1})$ is obtained by integrating Eq. (4.32) from t_{n-1} to t_n .

$$\int_{\hat{x}_{n-1}}^{\hat{x}_n} d\hat{x}(t | t_{n-1}) = \int_{t_{n-1}}^{t_n} f[\hat{x}(t | t_{n-1}), t] dt$$

The solution is the nominal value we will use for the measurement equation.

$$x_{nom}(t) \triangleq \hat{x}(t_n | t_{n-1}) = \hat{x}(t_{n-1} | t_{n-1}) + \int_{t_{n-1}}^{t_n} f[\hat{x}(t | t_{n-1}), t] dt \quad (4.34)$$

Equation (4.34) shows that the predicted state estimate is obtained by adding the integral of the undisturbed, nonlinear state equation to the filtered estimate.

Similarly, the best predicted measurement, $\Delta \hat{v}(t_n | t_{n-1})$, can be obtained from integrating the exact nonlinear measurement equation, Eq. (4.12), with the measurement noise set to zero and the state equal to the predicted state estimate.

$$\int_{t_{n-1}}^{t_n} \hat{v} dt = \int_{t_{n-1}}^{t_n} h[\hat{x}(t | t_{n-1}), t] dt$$

Hence, the best predicted measurement is

$$\Delta \hat{v}(t_n | t_{n-1}) = \int_{t_{n-1}}^{t_n} h[\hat{x}(t | t_{n-1}), t] dt \quad (4.35)$$

Note again, that Eq. (4.35) is exact and not an approximation of the measurement equation. This is the predicted value of the measurement that will be used in the extended Kalman filter to compare with the actual measurements from the Inertial Navigation System.

Now, for the perturbation equation, the reference measurement trajectory is the approximation given by Eq. (4.31). The predicted measurement estimate for the perturbation equation $\Delta \hat{v}_p$ is the following approximation with the nominal value of the state equal to the predicted state estimate.

$$\Delta \hat{v}_p(t_n | t_{n-1}) \triangleq h[\hat{x}(t_n | t_{n-1}), t_n] \Delta t \quad (4.36)$$

The deviation from the reference measurement trajectory is defined as

$$\delta v(t_n) \triangleq \Delta v(t_n) - \Delta \hat{v}_p(t_n | t_{n-1}) \quad (4.37)$$

Substituting Eqs. (4.14) and (4.36) into Eq. (4.37) gives

$$\delta v(t_n) = h[x(t_n), t_n] \Delta t - h[\hat{x}(t_n | t_{n-1}), t_n] \Delta t + m(t_n) \Delta t \quad (4.38)$$

If the deviations from the reference measurement trajectory are small, so that the higher-order terms can be neglected, a Taylor series expansion of $h(x, t) \Delta t$ about the predicted state estimate gives

$$h[x(t_n), t_n] \Delta t \cong h[\hat{x}(t_n | t_{n-1}), t_n] \Delta t + H[\hat{x}(t_n | t_{n-1}), t_n] \{x(t_n) - \hat{x}(t_n | t_{n-1})\} \quad (4.39)$$

where

$$H[\hat{x}(t_n | t_{n-1}), t_n] \triangleq \left[\frac{\partial h_i[\hat{x}(t_n | t_{n-1}), t_n]}{\partial x_j} \right] \Delta t$$

$i = 1, 2, 3 \quad j = 1, 2, \dots, 63$

is a (3×63) matrix of partial derivatives of the elements of $h[x(t_n), t_n]$, evaluated at $\hat{x}(t_n | t_{n-1})$, with respect to each state variable x_j , and finally multiplied by Δt . Now Eq. (4.17) evaluated at $t = t_n$ and with measurements up to time t_{n-1} gives

$$\delta x(t_n) = x(t_n) - \hat{x}(t_n | t_{n-1}) \quad (4.40)$$

Substituting Eqs. (4.40) and (4.39) into Eq. (4.38) gives the following discrete solution to the measurement perturbation.

$$\delta v(t_n) = H[\hat{x}(t_n | t_{n-1}), t_n] \delta x(t_n) + m(t_n) \Delta t \quad (4.41)$$

Equations (4.30) and (4.41) give us the following linearized discrete system

$$\begin{aligned} \delta x(t_n) = & \Phi[t_n, t_{n-1}; \hat{x}(t_{n-1}|t_{n-1})] \delta x(t_{n-1}) + \Gamma[t_n, t_{n-1}; \hat{x}(t_{n-1}|t_{n-1})] \\ & \times w(t_{n-1}) \end{aligned} \quad (4.42)$$

$$\delta v(t_n) = H[\hat{x}(t_n|t_{n-1}), t_n] \delta x(t_n) + m(t_n) \Delta t$$

with the following stochastic description

$\{w(t_k), k = 0, 1, 2, \dots\}$ - is a zero mean, gaussian white, vector, disturbance sequence

$E\{w(t_k) w^T(t_j)\} = Q(t_k) \delta_{jk}$ for all $j, k = 0, 1, 2, \dots$ is the disturbance covariance

$\{m(t_n), n = 1, 2, 3, \dots\}$ is described in Eq. (4.14)

$w(t_k)$ and $m(t_n)$ are independent for all k and n

From Eq. (4.17), with $t = t_0$

$$\delta x(t_0) = x(t_0) - \hat{x}(t_0|t_0) \quad (4.43)$$

For the case of linear dynamics and linear measurements, it is well known [16] that $\hat{x}(t|t)$ is obtained by a linear operation on the measurements, and is therefore a gaussian random vector. Also, by definition

$$\hat{x}(t_0|t_0) \triangleq E\{x(t_0)\} = x_0 \quad (4.44)$$

Since $x(t_0)$ is gaussian with a mean value of x_0 , Eqs. (4.44) and (4.43) reveal that $\delta x(t_0)$ is gaussian with the following values for its mean and covariance.

$$E\{\delta x(t_0)\} = 0$$

$$\begin{aligned} E\{\delta x(t_0) \delta x^T(t_0)\} &= E\{[x(t_0) - x_0][x(t_0) - x_0]^T\} \\ &= P_0 \text{ [Reference Eq. (4.8)]} \end{aligned} \quad (4.45)$$

Finally, $\delta x(t_0)$ is independent of $w(t_{n-1})$ and $m(t_n)$ for all values of n .

Equation (4.42) and the associated stochastic description meet all the requirements of Theorem 5.5 of Meditch [16]. Therefore, the theorem shows that the best filtered estimates of the perturbation states are generated by the linear Kalman filter,

$$\delta \hat{x}(t_n | t_n) = \delta \hat{x}(t_n | t_{n-1}) + A(t_n)[\delta v(t_n) - H(\hat{x}, t_n) \delta \hat{x}(t_n | t_{n-1})] \quad (4.46)$$

where

$$\delta \hat{x}(t_n | t_{n-1}) = \Phi[t_n, t_{n-1}; \hat{x}(t_{n-1} | t_{n-1})] \delta \hat{x}(t_{n-1} | t_{n-1})$$

$$H(\hat{x}, t_n) \equiv H[\hat{x}(t_n | t_{n-1}), t_n]$$

$A(t_n)$ - is the Kalman gain, whose equations will be given later in the text

We are not directly interested in the perturbation states, except for the equations to compute the Kalman gain $A(t_n)$, which will be given later. We are interested in obtaining an expression for $\hat{x}(t_n | t_n)$. If

we take the conditional expectation of Eq. (4.17), with respect to the measurements up to time t_{n-1} , and let the state be at time $t = t_{n-1}$, we find that

$$\delta \hat{x}(t_{n-1} | t_{n-1}) = \hat{x}(t_{n-1} | t_{n-1}) - \hat{x}(t_{n-1} | t_{n-1}) \equiv 0 \quad (4.47)$$

Therefore, $\delta \hat{x}(t_n | t_{n-1})$ of Eq. (4.46) is also zero, so Eq. (4.46) reduces to

$$\delta \hat{x}(t_n | t_n) = A(t_n) \delta v(t_n) \quad (4.48)$$

Now, if we take the conditional expectation of Eq. (4.40), with respect to the measurements up to time t_n , and let the state be at time $t = t_n$, we find that

$$\delta \hat{x}(t_n | t_n) = \hat{x}(t_n | t_n) - \hat{x}(t_n | t_{n-1}) \quad (4.49)$$

Note that in Eq. (4.49) the predicted state estimate is independent of the measurement at time $t = t_n$; in other words, you do not change the predicted state estimate that was projected from time t_{n-1} based on later knowledge of the measurement at time t_n . Therefore, the last term of Eq. (4.40) does not change because of the conditional expectation operation. Since we are interested in using the best predicted measurement defined by Eq. (4.35) in the extended Kalman filter, rather than the approximation of Eq. (4.36), the deviation from the reference measurement trajectory can be redefined to be

$$\delta v(t_n) \triangleq \Delta v(t_n) - \Delta \hat{v}(t_n | t_{n-1}) \quad (4.50)$$

Substituting Eqs. (4.49) and (4.50) into Eq. (4.48) gives an expression for the "best" estimate of the state at time t_n .

$$\hat{\mathbf{x}}(t_n | t_n) = \hat{\mathbf{x}}(t_n | t_{n-1}) + A(t_n)[\Delta \mathbf{v}(t_n) - \Delta \hat{\mathbf{v}}(t_n | t_{n-1})] \quad (4.51)$$

where

$\hat{\mathbf{x}}(t_n | t_n)$ - is the filtered estimate at time t_n and therefore provides the "best" estimate of the state $\mathbf{x}(t_n)$ based on measurements taken up to time t_n .

$$\hat{\mathbf{x}}(t_n | t_{n-1}) = \hat{\mathbf{x}}(t_{n-1} | t_{n-1}) + \int_{t_{n-1}}^{t_n} \mathbf{f}[\hat{\mathbf{x}}(t | t_{n-1}), t] dt -$$

is the predicted state estimate [Reference Eq. (4.34)]

$A(t_n)$ - is the Kalman filter gain

$\Delta \mathbf{v}(t_n)$ - is the actual INS velocity measurements

$$\Delta \hat{\mathbf{v}}(t_n | t_{n-1}) = \int_{t_{n-1}}^{t_n} \mathbf{h}[\hat{\mathbf{x}}(t | t_{n-1}), t] dt - \text{ is the predicted}$$

measurement [Reference Eq. (4.35)]

$[\Delta \mathbf{v}(t_n) - \Delta \hat{\mathbf{v}}(t_n | t_{n-1})]$ - is the measurement residual mentioned at the beginning of Section 4

The equations for computing the Kalman gain $A(t_n)$ are also from Theorem 5.5 of Meditch [16]

$$A(t_n) = P(t_n | t_{n-1}) H^T [H P(t_n | t_{n-1}) H^T + R^*]^{-1}$$

$$P(t_n | t_{n-1}) = \Phi P(t_{n-1} | t_{n-1}) \Phi^T + \Gamma Q \Gamma^T \quad (4.52)$$

$$P(t_n | t_n) = [I - A(t_n) H] P(t_n | t_{n-1}) [I - A(t_n) H]^T + A(t_n) R^* A^T(t_n)$$

where

$$H = H[\hat{x}(t_n | t_{n-1}), t_n] \quad [\text{Reference Eq. (4.39)}]$$

$$R^* = (\Delta t)^2 R(t_n) \quad [\text{Reference Eq. (4.14)}]$$

$$\Phi = \Phi[t_n, t_{n-1}; \hat{x}(t_{n-1} | t_{n-1})] \quad [\text{Reference Eq. (4.22) or (4.24)}]$$

$$\Gamma = \Gamma[t_n, t_{n-1}; \hat{x}(t_{n-1} | t_{n-1})] \quad [\text{Reference Eq. (4.26) or (4.29)}]$$

$$Q = Q(t_{n-1}) \quad [\text{Reference Eq. (4.42)}]$$

I - (63×63) identity matrix

$P(t_{n-1} | t_{n-1})$ and $P(t_n | t_n)$ - are the filtering error covariance matrices at time t_{n-1} and t_n respectively

$P(t_n | t_{n-1})$ - is the prediction error covariance matrix

$\delta x(t_n) = \tilde{x}(t_n | t_{n-1}) \triangleq x(t_n) - \hat{x}(t_n | t_{n-1})$ is the prediction error
[Reference Eq. (4.40)]

$\delta x(t_{n-1}) = \tilde{x}(t_{n-1} | t_{n-1}) \triangleq x(t_{n-1}) - \hat{x}(t_{n-1} | t_{n-1})$ is the filtering error [Reference Eq. (4.17)]

Equation (4.51) is known as the extended Kalman filter, since it applies to the nonlinear state and measurement equations. In other words, it extends the filtering process beyond the linear perturbation equations of Eq. (4.42). It is important to note, however, that the Kalman gain is based on the linear perturbation equations. Therefore, the requirement that the state and measurement deviations must remain small is still a constraint on the filtering process. This can be seen in the second term of Eq. (4.51). The second term, consisting of the Kalman gain multiplying the measurement residual, is called the correction term, since it corrects the predicted estimate $\hat{x}(t_n | t_{n-1})$ based on the measurement data. If the linearization is invalid, the Kalman gain will apply an "invalid" correction that will degrade the filtered estimate. Note that the approximation of the Δv equation, Eq. (4.13), is contained only in the Kalman gain computation, as was mentioned in Section 4.3. The simulation results show that the effect of this approximation is negligible, as long as Δt is maintained reasonably small. The most important point to understand is that Eq. (4.51) is the solution to the calibration problem. It formulates the data reduction method to obtain the best estimate of the states in Table 4.1. A schematic of the extended Kalman filter algorithm is shown in Figure 4.3. The algorithm simply implements Eq. (4.51).

The simulations described in Sections 5 and 6 will provide answers to most of the questions raised in this section. The questions answered by the simulations are:

- (a) Is the linearization and therefore the filtering process valid?

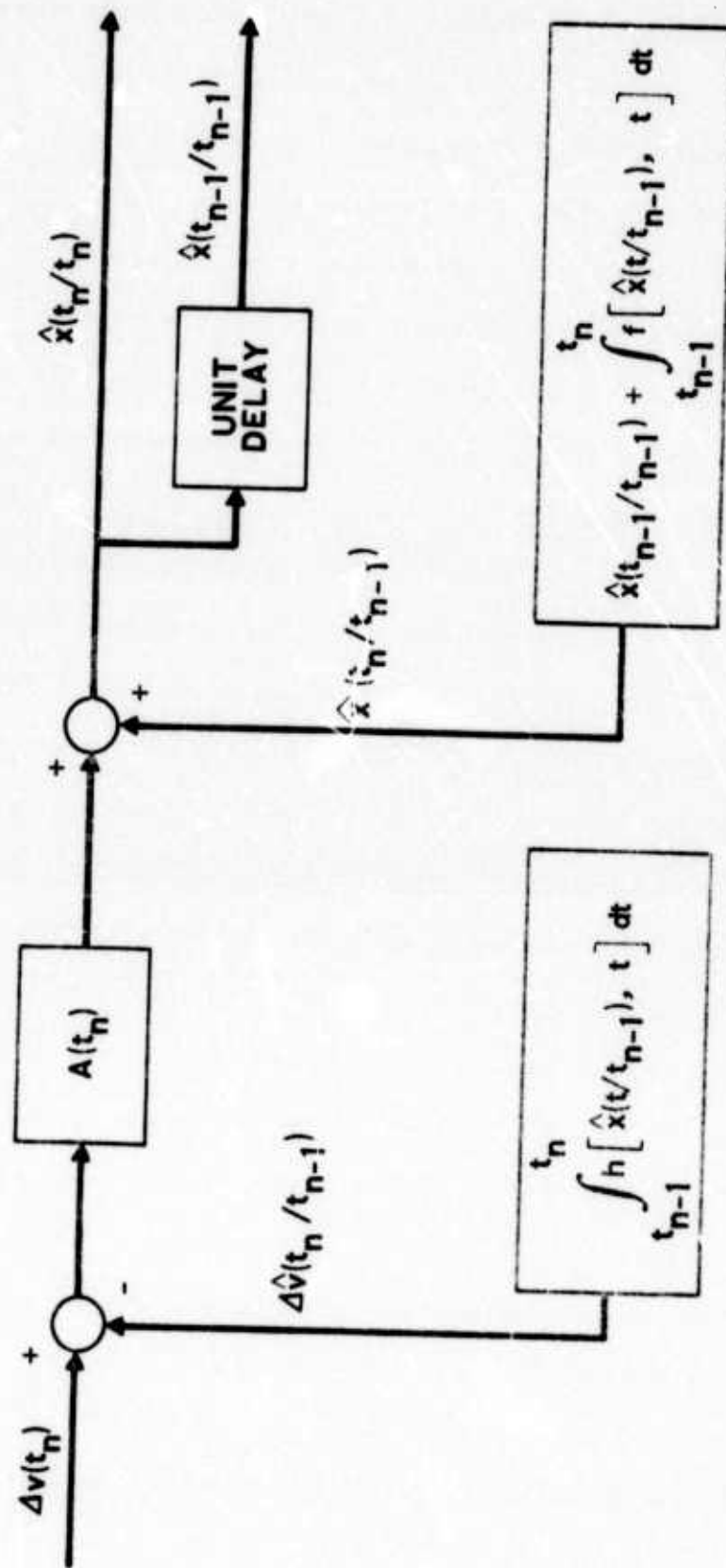


Figure 4.3. Schematic of the Extended Kalman Filter Algorithm

- (b) Is there an observability problem, and, if so, can the data reduction technique resolve it?
- (c) Does the Δv approximation prevent filter convergence?
- (d) Can the computation of the filter be simplified by assuming $F[\hat{x}, t]$ is constant over the measurement interval, and thereby permit ϕ and Γ to be determined by the simple power series forms of Eqs. (4.24) and (4.29) respectively?

The only question that remains is the impact on the assumed statistical model if the disturbance process is found to be correlated. Bucy and Joseph [20] show that correlated noise can be approximated quite well by uncorrelated noise having the same low frequency spectral density as the correlated process. They claim that the approximation is valid, provided that the time constant of the noise is small with respect to the total filtering time. In those cases where a correlated model was assumed for gyro drift, the time constant was specified to be in a range of 20 to 50 seconds. Sections 5 and 6 will show that the total filtering time will be 10 to 15 minutes per g-level for the centrifuge calibration and 2 to 3 hours for the 1-g calibration. Therefore, the assumed statistical model with the adjusted variance proposed by Bucy and Joseph may be an excellent alternative to augmenting the state vector.

SECTION 5

SIMULATION OF A 1-g CALIBRATION

A centrifuge test program normally consists of a 1-g calibration in the local gravitational field prior to and immediately following the operating centrifuge test. The purpose of this test is to determine the overall effect of the centrifuge environment on the fixed and first-order error coefficients. The results of a 17-state simulation, using the same techniques proposed for the operating centrifuge test, are contained in this section. Measurement data was generated by simulating the platform motion due to error drift, earth-rate input, and a prespecified command-torquing profile. The measurement data was input to the extended Kalman filter algorithm, defined in Section 4, to obtain estimates of 14 inertial sensor parameters and the three Euler angle states used to track the platform motion. The simulations described here and in Section 6 were developed and operated, over a 6-month time period, on a Control Data Corporation 7600 scientific computer located at The Aerospace Corporation, El Segundo, California.

5.1 SIMULATION STATES AND EQUATIONS

Since the applied acceleration is limited to 1 g, only the fixed and first-order sensor coefficients contribute significantly to the gyro drift and accelerometer output uncertainty. As will be shown in Section 6, the higher-order accelerometer coefficients range from 5 to 12 $\mu\text{g}/\text{g}^2$ for the second-order terms and 3 $\mu\text{g}/\text{g}^3$ for the third-order terms, where $1 \mu\text{g} = 1 \times 10^{-6}$ g's. The gyro higher-order

Preceding page blank

compliance terms range from 3 to 4 meru/g², where a meru is a rate unit defined by

$$1 \text{ earth-rate-unit (eru)} = 7.292116 \times 10^{-5} \text{ rad/sec} \approx 15 \text{ deg/hour}$$

$$1 \text{ milli-earth-rate unit (meru)} = 10^{-3} \text{ eru}$$

and is obviously based on the earth's rotational speed ω_{ie} .

The 14 sensor parameters and three Euler angles are defined in Table 5.1. All the fixed and first-order accelerometer terms normally considered in a platform calibration have been included. In the case of the gyro, the mass unbalance was limited to the input axis term. One misalignment angle for each type of sensor was included to evaluate the ability of the filtering process to estimate sensor misalignments. Since the purpose of the simulation was to validate the data reduction method, a sufficient number of states were included to represent all the basic types of fixed and first-order terms usually determined from a physical calibration process; however, the total number of states was limited to keep the complex task of structuring and analyzing the filter tractable.

Prior to an Inertial Navigation System test, a sequence of component tests is performed during the development phase of the platform. This implies that the basic structure of the sensor models should be fairly well defined before the platform tests are conducted. Since one of the main purposes of the simulation was to validate the linearization and determine the effect of the Δv approximation contained in the Φ and H terms of the gain computation, Eq. (4.52), no additional modeling errors were considered elsewhere in the filter.

Table 5.1. States of the 1-g Simulation

Symbol	Description	Units	State Designation
D_{FX}	X - gyro fixed drift	meru	x_1
D_{FY}	Y - gyro fixed drift	meru	x_2
D_{FZ}	Z - gyro fixed drift	meru	x_3
D_{IX}	X - gyro input axis unbalance	meru/g	x_4
D_{IY}	Y - gyro input axis unbalance	meru/g	x_5
D_{IZ}	Z - gyro input axis unbalance	meru/g	x_6
K_{0X}	X - accelerometer bias	μg	x_7
K_{0Y}	Y - accelerometer bias	μg	x_8
K_{0Z}	Z - accelerometer bias	μg	x_9
K_{1X}	X - accelerometer scale factor	$\mu g/g$	x_{10}
K_{1Y}	Y - accelerometer scale factor	$\mu g/g$	x_{11}
K_{1Z}	Z - accelerometer scale factor	$\mu g/g$	x_{12}
η_{x_0}	X - gyro out-of-plane misalignment	arc-sec	x_{13}
ψ_{x_i}	X - accelerometer in-plane misalignment	arc-sec	x_{14}
α	Euler angle about X platform axis	arc-sec	x_{15}
β	Euler angle about Z platform axis	arc-sec	x_{16}
γ	Euler angle about Y platform axis	arc-sec	x_{17}

In other words, it was assumed that the model used to generate the measurement data and the model contained in the state and measurement dynamics of the predicted filter loops (reference Figure 4.3) were identical. This does not imply that model inaccuracies will not exist in the physical application of the algorithm. In fact, as discussed by Jazwinski in Chapters 7 through 10 of Reference [17], model inaccuracies can cause serious degradation or divergence of the filtering process. An example of the degradation caused by including the Δv approximation in the measurement prediction loop, rather than the gain computation, is shown in the simulation results. However, additional investigations of the effects of modeling error are recommended for future study.

Two additional simplifying assumptions were made with respect to the platform rate equation, Eq. (2.33). The internal gyro torquer scale factors were assumed to be unity, to limit the number of states in the simulation, and, finally, the servo error term was assumed to be zero. The servo error term is considered to be a deterministic quantity, whose value is obtained from a servo analysis and test of the platform stabilization loop.

The simulation equations are obtained from a combination of Eqs. (3.25), (2.33), and (2.34). Section B.1 of Appendix B shows that the contribution of the Group 2 terms of Eq. (3.25) can be neglected, and, since the centrifuge is nonoperating for the 1-g calibration, the applied acceleration equation reduces to

$$A_{is}^s = C_p^s C_r^p G^e \quad (5.1)$$

where

C_r^P - is the Euler transformation matrix given by Eq. (4.1)

C_p^s - is obtained from Eqs. (3.19) and (3.20) with the misalignment angles defined in Table 5.1

G^e - is defined by Eq. (3.25) with $g = 1$

Equation (5.1) gives the acceleration applied to each gyro, which is used, along with the states designated in Table 5.1, to obtain the following set of platform rate equations from Eq. (2.33):

$$\begin{aligned}\omega_{xp} &= -x_1 - x_4 E_{13} + x_4 x_{13} E_{33} - TGX \\ &\quad - E_{12} WEC - E_{13} WES \\ \omega_{yp} &= -x_2 - x_5 E_{23} - TGY - E_{22} WEC - E_{23} WES \\ \omega_{zp} &= x_1 x_{13} + x_{13} x_4 E_{13} + x_{13} TGX - x_3 \\ &\quad - x_6 E_{33} - TGZ - E_{32} WEC - E_{33} WES\end{aligned}\quad (5.2)$$

where

$$E_{12} = cx_{17} sx_{16} cx_{15} + sx_{17} sx_{15}$$

$$E_{13} = cx_{17} sx_{16} sx_{15} - sx_{17} cx_{15}$$

$$E_{22} = cx_{16} cx_{15}$$

$$E_{23} = cx_{16} sx_{15}$$

$$E_{32} = sx_{17} sx_{16} cx_{15} - cx_{17} sx_{15}$$

[Reference Eq. (4.1)]

$$E_{33} = s x_{17} s x_{16} s x_{15} + c x_{17} c x_{15}$$

WEC, WES - are the earth rate components defined in Eq. (3.3) and represented in ω_{1r}^r [See Eq. (3.17)]

TGX, TGY, TGZ - are the gyro command torque values of Eq. (2.33)

With the platform rates defined by Eq. (5.2), we can define the state vector equation directly from Eq. (4.8).

$$\dot{\underline{x}} = \underline{f}(\underline{x}) + \underline{w}(t) \quad (5.3)$$

where

$\dot{\underline{x}}$ and \underline{w} are 17-element vectors

$\underline{f}(\underline{x})$ - is a 17-dimensional vector-valued function

The only difference between Eq. (5.3) and Eq. (4.8) is the dimensionality of the equation and the fact that \underline{f} is not an explicit function of time. We know from Section 4 that the first 14 elements of \underline{f} are zero, and the last three elements contain the dynamics of the system platform rates.

$$\begin{aligned} f_{15} &= (\omega_{xp} \cos x_{17} + \omega_{zp} \sin x_{17}) / \cos x_{16} \\ f_{16} &= \omega_{zp} \cos x_{17} - \omega_{xp} \sin x_{17} \end{aligned} \quad (5.4)$$

$$f_{17} = (\omega_{xp} \cos x_{17} \sin x_{16} + \omega_{zp} \sin x_{17} \sin x_{16}) / \cos x_{16} + \omega_{yp}$$

The statistical description of Eq. (5.3) is identical to Eq. (4.8) with the dimensionality adjusted from 63 to 17.

The measurement equation is obtained in a similar manner as the state equation. Starting with Eq. (5.1), we obtain the acceleration applied to each accelerometer, which is used in conjunction with the states designated in Table 5.1 to obtain the following set of equations for the elements of $\underline{h}[\underline{x}(t_n)]$ from Eq. (2.34):

$$\begin{aligned} h_1 &= x_7(t_n) + x_{10}(t_n) E_{13}(t_n) - x_{10}(t_n) x_{14}(t_n) E_{23}(t_n) \\ h_2 &= x_8(t_n) + x_{11}(t_n) E_{23}(t_n) \\ h_3 &= x_9(t_n) + x_{12}(t_n) E_{33}(t_n) \end{aligned} \quad (5.5)$$

The measurement equation is identical to Eq. (4.14) with $\underline{h}[\underline{x}(t_n)]$ defined by Eq. (5.5). Note that \underline{h} is not an explicit function of time t_n .

5.2 MEASUREMENT SIMULATION

This section contains a description of the part of the simulation program that generated the measurement data. Table 5.2 contains a list of the mean values x_{0i} , and standard deviations $\sigma_{x_{0i}}$, used in the gaussian subroutine program to formulate the initial state vector $\underline{x}(t_0)$. Since the simulation values are considered the true state values, we will define $\underline{x}(t)$ to be

$$\underline{x}(t) \stackrel{\Delta}{=} \underline{x}_{\text{true}} \equiv \underline{x}_{\text{sim}} \quad (5.6)$$

Table 5.2. Initial State Means and Standard Deviations

State	Symbol	Mean Value (x_0)	Standard Deviation (σ_{x_0})	Units
x_1	D_{FX}	490.0	6.0	meru
x_2	D_{FY}	520.0	5.0	meru
x_3	D_{FZ}	110.0	4.0	meru
x_4	D_{IX}	72.0	4.0	meru/g
x_5	D_{IY}	68.0	5.0	meru/g
x_6	D_{IZ}	62.0	6.0	meru/g
x_7	K_{0X}	3500.0	30.0	μg
x_8	K_{0Y}	4250.0	40.0	μg
x_9	K_{0Z}	6310.0	60.0	μg
x_{10}	K_{1X}	999840.0	30.0	$\mu g/g$
x_{11}	K_{1Y}	999900.0	27.0	$\mu g/g$
x_{12}	K_{1Z}	998900.0	70.0	$\mu g/g$
x_{13}	r_{x_0}	260.0	15.0	arc-sec
x_{14}	ψ_{x_i}	305.0	10.0	arc-sec
x_{15}	α	180.0	5.0	arc-sec
x_{16}	β	110.0	5.0	arc-sec
x_{17}	γ	120.0	5.0	arc-sec

The mean values are representative of the sensor coefficients and misalignment magnitudes obtained from actual calibrations performed on the Carousel VB Inertial Measurement Unit. The standard deviations were chosen to be representative of the Carousel VB 1-sigma error budget [10] given in Table 5.3. The error budget represents measured uncertainty from a combination of sensor and platform calibration data taken over 90-day intervals. Since the error budget uncertainty represents changes from the last calibration, in addition to calibration uncertainties, both the repeatability effect and operating random changes discussed in Section 4.3 of Section 4 are included in the error budget. Comparing Tables 5.2 and 5.3, we see that the major portion of the error budget was included in the initial state deviations, which represent the lack of repeatability from turn-off to turn-on, plus the operating disturbance input up to the start of the calibration at $t = t_0$, as described in Section 4.3. From experience, the repeatability effect is usually the major portion of the error budget. It should be noted that the mean value of the Euler angles represents the initial alignment error of the platform with respect to (east, north, up); this corresponds to the (x_p, y_p, z_p) platform axes, which, in turn, correspond to the (α, γ, β) Euler angles. The Euler angle standard deviation, in conjunction with the disturbance process deviation, to be given later, represents the uncertainty associated with the platform stabilization loop.

Table 5.4 contains a list of the standard deviations for the zero mean, gaussian white, disturbance process $\underline{w}(t)$ of Eq. (4.8) and the zero mean, gaussian white, measurement noise sequence $\underline{m}(t_n)$ of

Table 5.3. Carousel VB 1-Sigma Error Budget

<u>Error Sources</u>	<u>1-Sigma Uncertainty</u>
Initial Attitude	
Azimuth (z - axis)	25 arc-sec
Level (x & y axes)	5 arc-sec
Accelerometer (each sensor)	
Bias	25 - 86.6 μ g
Scale factor	25 - 86.6 μ g/g
Input axis alignment	13 arc-sec
Gyro (each sensor)	
Fixed drift	2.0 - 6.93 meru
Unbalance drift	2.25 - 7.80 meru/g
In-axis compliance	0.208 meru/g ²
Cross-axis compliance	0.087 meru/g ²
Input axis alignment	17.3 arc-sec

Table 5.4. Standard Deviations of Disturbance and Measurement Noise

Disturbance (w) No.	Standard Deviation (σ_w)		Units	Measurement Noise (m) No.	Standard Deviation (σ_m)		Units
1	0.6		meru	1	13.0		$\mu\text{g-sec}$
2	0.5		meru	2	13.0		$\mu\text{g-sec}$
3	0.4		meru	3	13.0		$\mu\text{g-sec}$
4	0.4		meru/g				
5	0.5		meru/g				
6	0.6		meru/g				
7	3.0		μg				
8	4.0		μg				
9	6.0		μg				
10	3.0		$\mu\text{g/g}$				
11	2.7		$\mu\text{g/g}$				
12	7.0		$\mu\text{g/g}$				
13	1.5		arc-sec				
14	1.0		arc-sec				
15	5.0		arc-sec				
16	5.0		arc-sec				
17	5.0		arc-sec				

Eq. (4.14). From test experience, a good approximation of the magnitude of the operating random uncertainty in sensor parameters is 10 percent of the repeatability uncertainty. Therefore, the values of σ_{w_1} through $\sigma_{w_{14}}$ are 10 percent of the associated σ_{x_i} given in Table 5.2. The deviations associated with the Euler angle disturbances (w_{15} thru w_{17}) were set equal to the initial state deviation values ($\sigma_{x_{15}}$ thru $\sigma_{x_{17}}$), since they are both associated with the stabilization loop uncertainty. The Carousel VB error budget disturbance represents the measured uncertainty over a 24- to 48-hour continuous test program. The assumption made for the simulation was that the disturbance represents the uncertainty over the calibration test time, which is established by the length of time the command torquing is applied. The prespecified command torque profile time was 3 hours and 39 minutes or 13,140 seconds. Since the measurements were generated at discrete time points, t_n , the disturbance added each Δt measurement cycle was obtained by scaling the total disturbance standard deviation by

$$\sigma'_{w_i} = \sqrt{k} \sigma_{w_i} \quad i = 1, 2, \dots, 17 \quad (5.7)$$

where

σ'_{w_i} - is the standard deviation of the disturbance added each measurement cycle

$$k = \Delta t / 13140$$

σ_{w_i} - is the total disturbance deviation and are the values listed in Table 5.4

Equation (5.7) holds, since $\underline{w}(t)$ is gaussian white and therefore time independent. Independence implies that the sum of the variances of each measurement cycle equals the total disturbance variance. The number of measurement cycles is $13140/\Delta t$ or $1/k$. Therefore,

$$\sigma_{w_i}^2 = \frac{(\sigma'_{w_i})^2}{k} \equiv (\sigma'_{w_i})^2 + (\sigma'_{w_i})^2 + \dots \left(\frac{1}{k} \text{ terms}\right) \quad (5.8)$$

and Eq. (5.7) follows. The equations of the first 14 sensor parameters are in discrete form in the measurement simulation and are represented by the following example of the first parameter D_{FX} .

$$\begin{aligned} D_{FX}(t_n) &= D_{FX}(t_{n-1}) + w'_1(t_n) \\ n &= 1, 2, 3, \dots, 13141 \end{aligned} \quad (5.9)$$

where $w'_1(t_n)$ - is the scaled disturbance.

For the Euler angles, the disturbance is added after the dynamic equations of Eq. (5.4) are integrated. For example,

$$\alpha(t_n) = \alpha'(t_n) + w'_{15}(t_n) \quad (5.10)$$

where

$$\alpha'(t_n) = \alpha(t_{n-1}) + \int_{t_{n-1}}^{t_n} \dot{\alpha} dt$$

$$\dot{\alpha} \equiv f_{15}$$

[Reference Eq. (5.4)]

$w'_{15}(t_n)$ - is the scaled disturbance

The measurement noise is based on the fact that the output of the accelerometers is a series of Δv pulses that are counted by the platform computer over each measurement cycle. The pulse weight for the Carousel VB is 0.002569 ft/sec/pulse. Converting this value to local gravity units gives a pulse weight of 80.28 $\mu\text{g-sec/pulse}$, where $g = 32.124 \text{ ft/sec}^2$. The total Δv for a measurement cycle will be some integral number of pulses plus some residual value of velocity. If the residual value is greater than 1/2 of a pulse (i.e., greater than 40.14 $\mu\text{g-sec}$), then another pulse will be generated. If the residual is less than 40.14 $\mu\text{g-sec}$, then no pulse will be added. Therefore, the error in Δv will be somewhere in the range of 0 to 40.14 $\mu\text{g-sec}$. The assumption is that the maximum error of 40.14 $\mu\text{g-sec}$ is a 3-sigma value; hence, a 1-sigma deviation for each measurement cycle would be 13 $\mu\text{g-sec}$, which is the value shown in Table 5.4. Note that, since the uncertainty in Δv occurs each cycle, there is no scaling of the measurement noise. The discrete form of the measurement equation used in the measurement simulation is

$$\Delta \underline{v}(t_n) = \Delta \underline{v}'(t_n) + \underline{m}(t_n) \quad (5.11)$$

where

$$\Delta \underline{v}'(t_n) = \int_{t_{n-1}}^{t_n} \underline{h} dt$$

h - is defined by Eq. (5.5)

We now see that the units given in Table 5.4 are compatible with the measurement simulation discrete equations.

After some preliminary runs of the simulation, a measurement cycle of $\Delta t = 1.0$ second was selected in conjunction with an integration step-size of 0.25 second. The method of integrating the state and measurement dynamics was 4th-order Runge-Kutta. It was found that increasing Δt degraded the Euler angle estimates, and decreasing it showed little improvement compared to the increase in measurement processing. Based on a nominal platform rate of 4.7×10^{-4} rad/sec (see Section B.1 of Appendix B) implies that measurements were taken every 1.62 arc-minutes of platform angle.

Figure 5.1 contains a flow diagram of the measurement simulation program. Block 1A sets up the initial state vector $\underline{x}(t_0)$ for the measurement simulation using the values of Table 5.2. The filter initial conditions brought in at Connector 3 are covered in the next section. The do-loop to Statement 499, located at the end of the flow diagram, is the major simulation loop that establishes the number of measurements N the filter will process. The first measurement occurs at time t_1 , where $t_1 - t_0 = \Delta t = 1.0$ second, implying that zero measurements will be processed when $M = 1$ and 13,140 will be processed when $M = 13,141$. Therefore, the maximum value of M permits the filter to process measurements over the entire torque profile time of 13,140 seconds. The results will show that filter convergence was occurring around 6200 cycles. The command torque generation block is given in detail in Figure 5.2. Initially, the

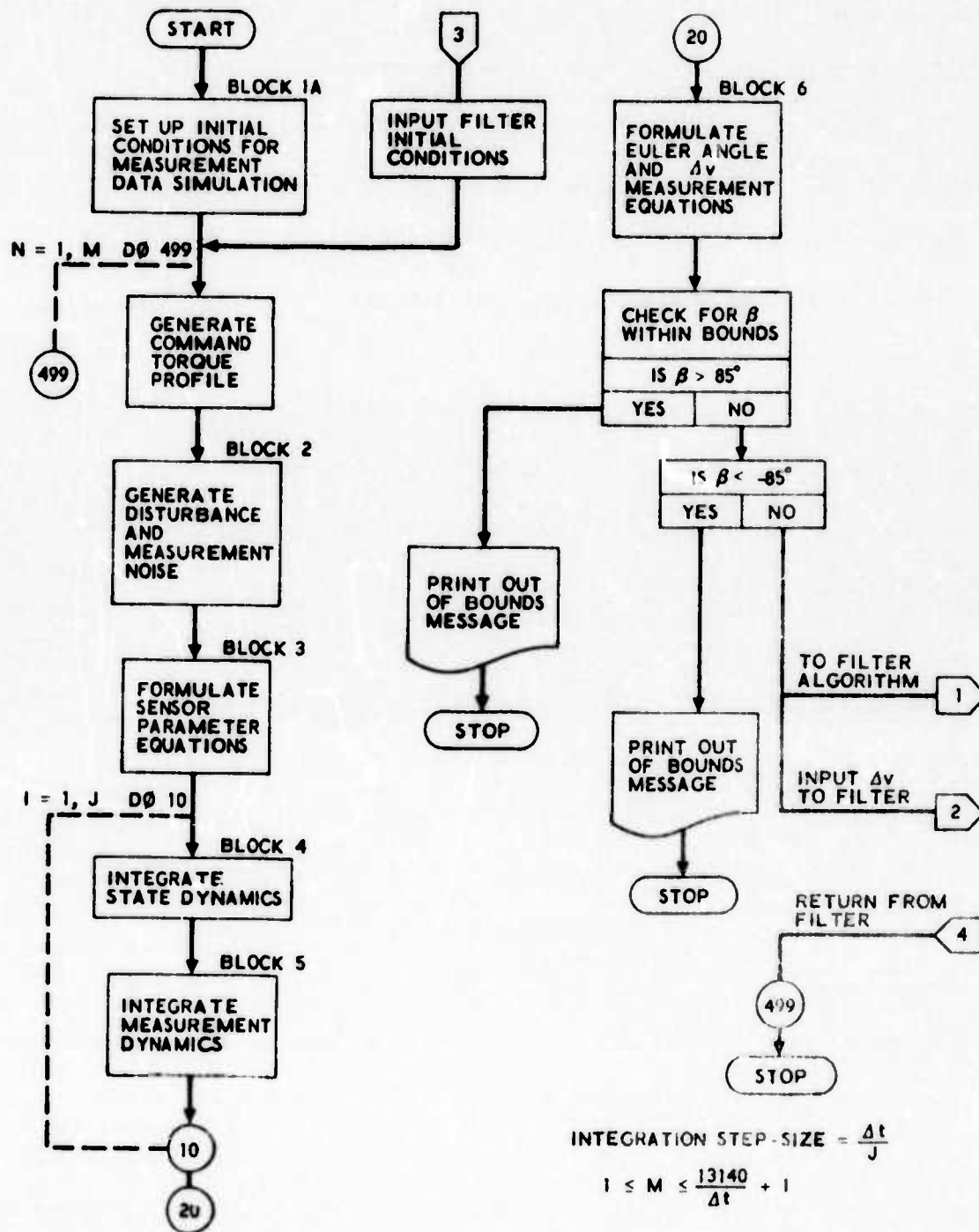


Figure 5.1. Flow Diagram of Measurement Simulation Program

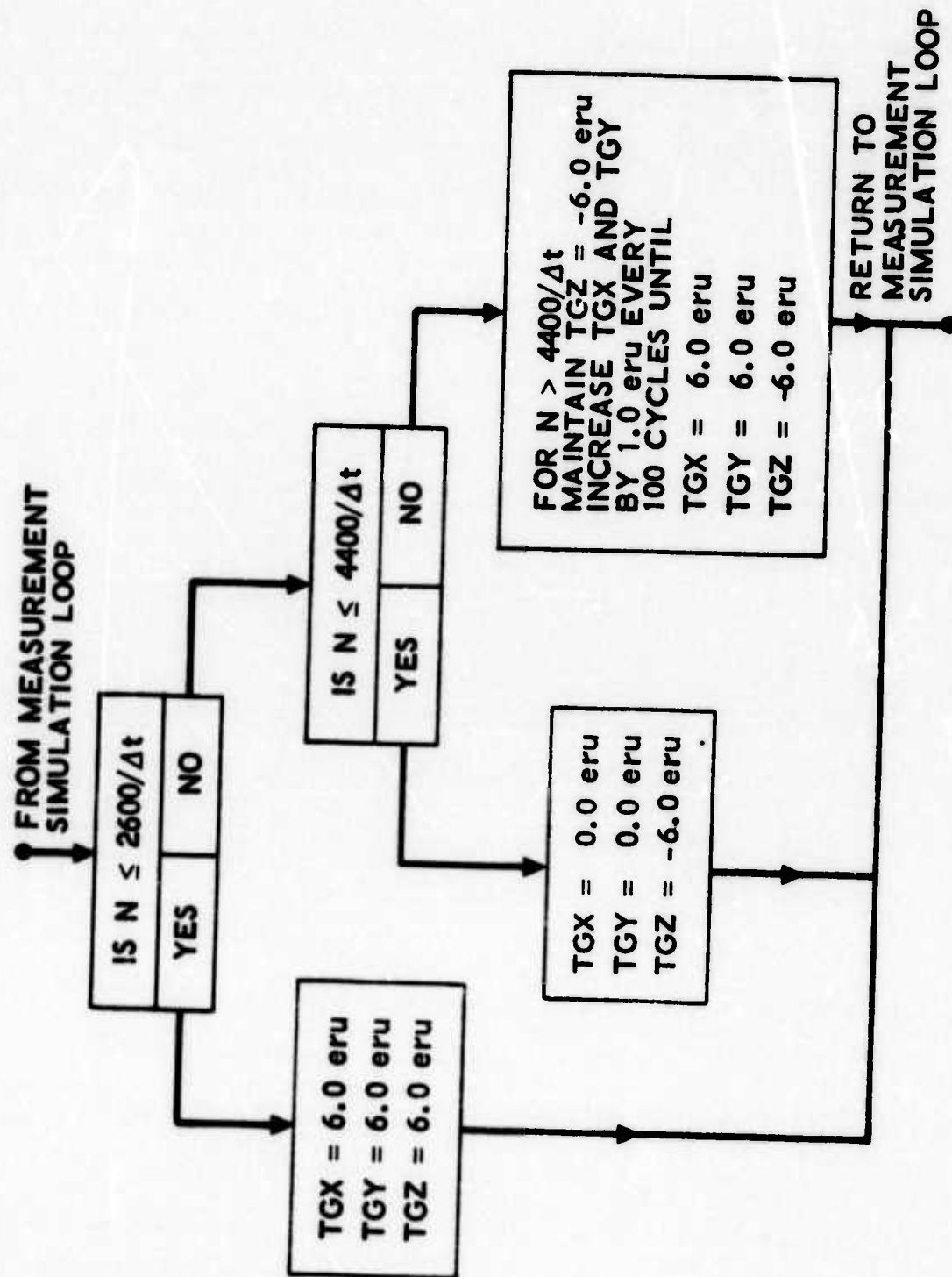


Figure 5.2. Command Torque Generation Block

command torque profile consisted of a sequence of maneuvers that placed each axis of the platform either vertically up or down, so that the maximum 1-g acceleration would be applied to each sensor. The torquing sequence required 13,140 seconds to complete the total profile. Since the filter was converging in less than one-half the torque profile time, the profile was modified to see the effect of applying a step-type torque program prior to filter convergence. Figure 5.2 shows the final form of the torque program. It should be understood that no attempt was made to optimize the torque program with respect to filter performance. Optimization of the torque profile will be discussed in Section 7 and is recommended for future study. Maximum command torquing of platforms ranges from 6 to 10 eru (earth-rate-units), since the basic use is to provide precise torquing during gyrocompass alignment procedures. In the case of the Carousel VB, the maximum command torque rate is 6 eru. Neglecting platform motion due to error drift and earth rate input, the first loop ($N \leq 2600$ with $\Delta t = 1$) applies 6 eru along the negative x_p and y_p axes [note the sign convention of Eq. (5.2)], which drives the platform from the initial (east, north, up) alignment to an orientation where the z_p axis is horizontal, the x_p axis is 45 deg above the horizontal, and the y_p axis is 45 deg below the horizontal. The second loop, $2600 < N \leq 4400$, applies 6 eru along the positive z_p axis to drive the y_p axis to a position of vertically down. The remaining loops maintain 6 eru along the positive z_p axis and step 1 eru of torque rate into both the negative x_p and y_p axes every 100 cycles, until a maximum of 6 eru is applied. The maximum torquing

along the three axes is maintained for the remaining measurement cycles.

Block 2 generates $\underline{w}(t)$ and $\underline{m}(t)$ using the values in Table 5.4. Block 3 formulates the sensor parameter equations represented by Eq. (5.9). Blocks 4 and 5 are 4th-order Runge-Kutta integration of Eqs. (5.4) and (5.5), respectively. As mentioned previously, the integration step-size was 0.25 second, implying that $J = 4$ in the integration do-loop. Block 6 formulates the Euler angle and Δv equations represented by Eqs. (5.10) and (5.11), respectively. The check for β within bounds stops the simulation if β is approaching the singularity condition. The filter is first entered at Connector 1. The Δv measurements are input to the filter algorithm at Connector 2. The return from the filter for the next measurement data cycle is accomplished at Connector 4. Statement 499 completes the major do-loop cycle. The iterations are complete when N equals the preset M value.

5.3 FILTER ALGORITHM

A flow diagram of the filter algorithm is contained in Figure 5.3. The filter equations of Section 4 are reformulated into a function of the measurement cycle variable N ; where the N th cycle occurs at time t_n , the $N-1$ st cycle occurs at time t_{n-1} and $t_n - t_{n-1} = \Delta t = 1$ second.

Define

$$\hat{x}(N-1) = \hat{x}(t_{n-1} | t_{n-1}) \quad (17 \times 1) \text{ filtered state vector at time } t_{n-1}$$

$$\hat{x}(N) = \hat{x}(t_n | t_n) \quad (17 \times 1) \text{ filtered state vector at time } t_n$$

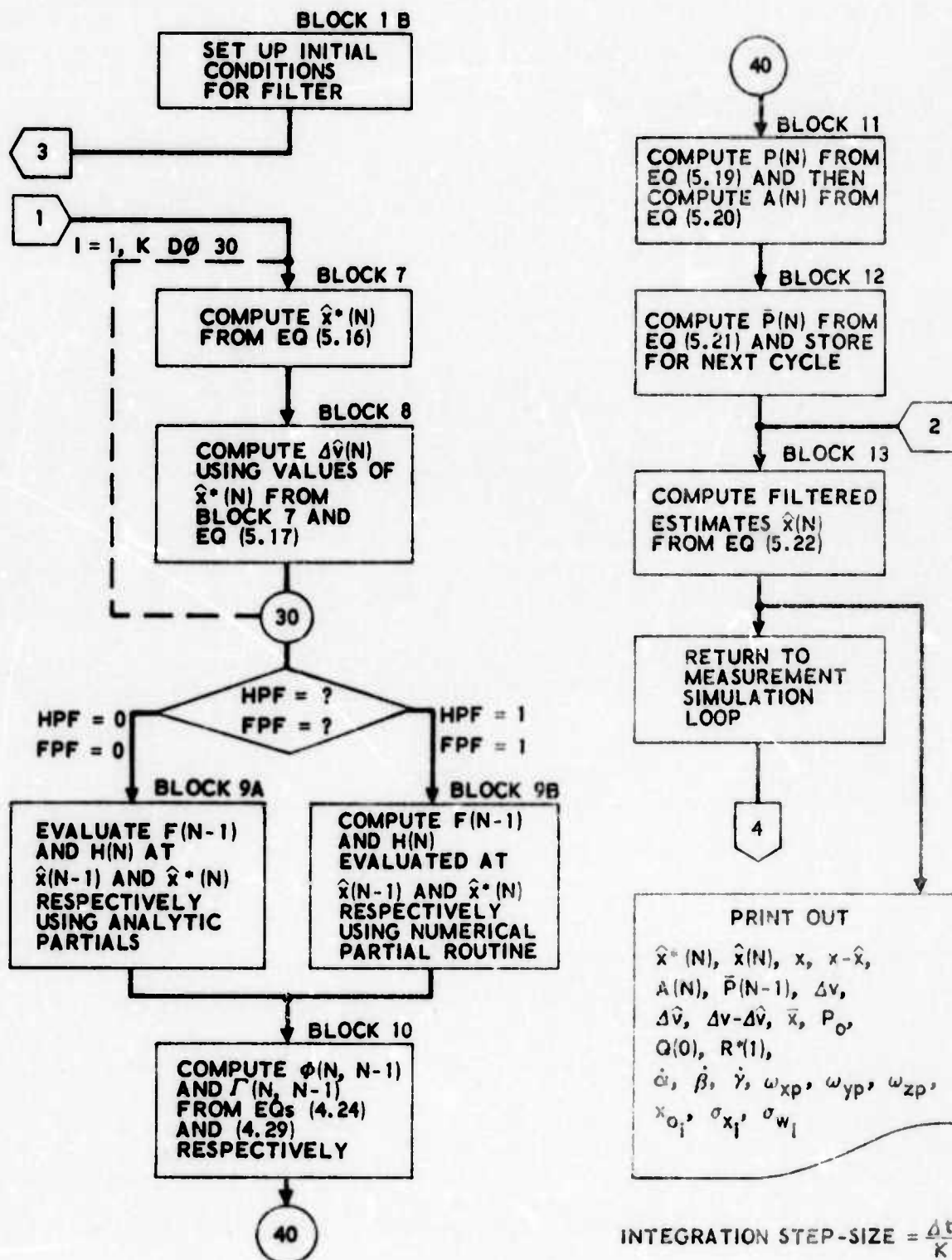


Figure 5.3. Flow Diagram of Filter Algorithm

$\hat{\mathbf{x}}^*(N) = \hat{\mathbf{x}}(t_n | t_{n-1})$ (17 × 1) predicted state vector

$\Delta \mathbf{v}(N)$ - (3 × 1) measurement data vector from measurement simulation program

$\Delta \hat{\mathbf{v}}(N)$ - (3 × 1) predicted measurement vector

$\mathbf{A}(N)$ - (17 × 3) Kalman gain matrix

$\mathbf{F}(N-1) = \mathbf{F}[\hat{\mathbf{x}}(t_{n-1} | t_{n-1})]$ (17 × 17) matrix of state dynamic partials

$\mathbf{H}(N) = \mathbf{H}[\hat{\mathbf{x}}(t_n | t_{n-1})]$ (3 × 17) matrix of measurement dynamic partials

$\Phi(N, N-1) = \Phi[t_n, t_{n-1}; \hat{\mathbf{x}}(t_{n-1} | t_{n-1})]$ (17 × 17) state transition matrix

$\Gamma(N, N-1) = \Gamma[t_n, t_{n-1}; \hat{\mathbf{x}}(t_{n-1} | t_{n-1})]$ (17 × 17) disturbance transition matrix

$\bar{\mathbf{P}}(N-1) = \mathbf{P}(t_{n-1} | t_{n-1})$ (17 × 17) filtering error covariance matrix at time t_{n-1}

$\bar{\mathbf{P}}(N) = \mathbf{P}(t_n | t_n)$ (17 × 17) filtering error covariance matrix at time t_n

$\mathbf{P}(N) = \mathbf{P}(t_n | t_{n-1})$ (17 × 17) prediction error covariance matrix

$\mathbf{Q}(N-1)$ - given (17 × 17) disturbance covariance matrix

$\mathbf{R}^*(N)$ - given (3 × 3) measurement error covariance matrix

$\bar{\mathbf{x}}_0$ - given mean value initial state vector (17 × 1)

\mathbf{P}_0 - given initial state covariance matrix (17 × 17)

Block 1B of Figure 5.3 establishes the initial conditions for the filter. The initial filtered estimate is $\hat{\mathbf{x}}(0) \equiv \bar{\mathbf{x}}_0$. Since we assume that we do not know the mean value of the initial state vector, $\bar{\mathbf{x}}_0$ represents our "best guess". How far off the "best guess" can be from the true mean value (given in Table 5.2) and still have the filter converge to its steady-state condition, indicates the stability of the calibration filtering process with respect to the initial state condition.

A number of values of \bar{x}_0 were used in the simulation and are given in the next section. The initial value of the filtering error covariance matrix is $\bar{P}(0) \equiv P_0$. P_0 is the initial state covariance matrix defined in Eq. (4.8). Again we assume we do not know P_0 . Examining Eq. (4.52) shows that, since Q is usually much smaller than \bar{P} , \bar{P} is the predominate factor in determining the initial gain of the filter. If $\bar{P}(0)$ is too large, then the gain level is placing too much weight on the initial "poor" estimates. This causes the filter to operate inefficiently. If $\bar{P}(0)$ is too small and the initial state uncertainty is large, then there is insufficient gain to make the necessary corrections which can cause the filter to diverge, since the linearization is no longer valid. In the case of Q , Eq. (4.52) shows that, when the filter is near convergence and, therefore, \bar{P} is close to zero (since the Kalman filter is a minimum variance filter), Q becomes the predominate factor in determining the filter gain. If Q is too small, then the gain is essentially zero, and this, in effect, decouples the filtered estimates from the measurement data, as can be seen from Figure 4.3, when $A(t_n) = 0$. If Q is too large, then the uncertainty level of the steady-state filtered estimates will be too high. The easiest initial factor to determine is $R^*(1)$, since it is directly related to the accelerometer output uncertainty.

A common practice in applying a filter is to assume $\bar{P}(0)$, $Q(0)$, and $R^*(1)$ are diagonal matrices, because of the difficulty in guessing initial off-diagonal covariance elements. The second assumption is that Q and R^* are stationary. In other words,

$$\begin{aligned} Q(N-1) &\equiv Q(0) \\ R^*(N) &\equiv R^*(1) \end{aligned} \quad \text{for all } N > 1 \quad (5.12)$$

Some preliminary simulations were performed to establish initial values for \bar{P} , Q , and R^* based on the general filter performance. The value of $\bar{P}(0)$ selected was a diagonal matrix whose elements are

$$p_{ii} = 2 \sigma_{x_{0i}}^2 \quad i = 1, 2, \dots, 17 \quad (5.13)$$

where

$\sigma_{x_{0i}}$ - are given in Table 5.2

The value of $Q(0)$ selected was a diagonal matrix whose elements are

$$q_{ii} = 2 \sigma_{w_i}^2 \quad i = 1, 2, \dots, 17 \quad (5.14)$$

where

σ_{w_i} - are given in Table 5.4

And, finally, the elements of $R^*(1)$ are

$$r_{jj} = \sigma_{m_j}^2 \quad j = 1, 2, 3 \quad (5.15)$$

where

σ_{mj} - are given in Table 5.4

No attempt was made to optimize filter performance by varying $\bar{P}(0)$, $Q(0)$, and $R^*(1)$. This is also recommended for future study.

In Blocks 7 and 8 of Figure 5.3, 4th-order Runge-Kutta integration was used with a step-size of 0.25 second. The integrals for $\hat{x}^*(N)$ and $\Delta\hat{v}(N)$ are both from Eq. (4.51).

$$\hat{x}^*(N) = \hat{x}(N-1) + \int_{t_{n-1}}^{t_n} f[\hat{x}(t|t_{n-1})] dt \quad (5.16)$$

$$\Delta\hat{v}(N) = \int_{t_{n-1}}^{t_n} h[\hat{x}(t|t_{n-1})] dt \quad (5.17)$$

Note that, in Eq. (5.16), there are only three elements of f that require integration. The elements of f are defined in Eq. (5.4). Since the first 14 elements of f are zero,

$$\hat{x}_i^*(N) \equiv \hat{x}_i(N) \quad i = 1, 2, \dots, 14 \quad (5.18)$$

In other words, the filtered estimates of the first 14 states are identically equal to their predicted estimates. Therefore, in Eq. (5.2), which defines the platform rates for Eq. (5.4), the first 14 states are evaluated at their filtered estimates. The Euler angle states are the only variables in Eq. (5.16) that are integrated forward

in time. Since the predicted states $\hat{x}^*(N)$ are obtained from Eq. (5.16), Eq. (5.17) is simplified, since the h function is now a constant function over the integration step-size interval and is obtained by evaluating the elements of h [reference Eq. (5.5)] at the predicted state values obtained from Eq. (5.16). Therefore, Blocks 7 and 8 are integrated simultaneously.

Block 9A is simply an evaluation of the partials of $F(N-1)$ and $H(N)$ at $\hat{x}(N-1)$ and $\hat{x}^*(N)$ respectively. The analytic partials are contained in Section C.1 of Appendix C. Block 9B is a standard numerical partial subroutine. The elements of f and h are evaluated at $\hat{x}(N-1)$ and $\hat{x}^*(N)$, respectively, which establishes the nominal value of the f and h elements. The value of each state is varied by some specified increment and the perturbation of the f and h elements about their nominal values is numerically equivalent to the value of the partial of that element with respect to the incremented state.

Since $F(N-1)$ is not an explicit function of time, the power series solution of Eq. (4.24) can be used to obtain Φ . Likewise, Γ can be obtained from its power series solution of Eq. (4.29). A value of $m = 4$ was used in both power series solutions.

The equations for Blocks 11, 12, and 13 are from Eq. (4.52). Expressing them in terms of N gives

$$P(N) = \Phi(N, N-1)\bar{P}(N-1)\Phi^T(N, N-1) + \Gamma(N, N-1)Q(N-1)\Gamma^T(N, N-1) \quad (5.19)$$

$$A(N) = P(N)H^T(N)[H(N)P(N)H^T(N) + R^*(N)]^{-1} \quad (5.20)$$

$$\begin{aligned} \bar{P}(N) &= [I - A(N) H(N)] P(N) [I - A(N) H(N)]^T \\ &+ A(N) R^*(N) A^T(N) \end{aligned} \quad (5.21)$$

$$\hat{x}(N) = \hat{x}^*(N) + A(N) [\Delta v(N) - \Delta \hat{v}(N)] \quad (5.22)$$

Note that $\Delta v(N)$ is input to the filter at Connector 2.

In order to evaluate the effect of the Δv approximation, an alternate filter, shown in Figure 5.4, was used. The alternate filter contains the Δv approximation in the predicted measurement loop. The measurements from the simulation were averaged over the measurement cycle to give an average acceleration value. This permits the \hat{h} equation evaluated at $\hat{x}(t_n | t_{n-1})$, which is equal to $\hat{A}V(t_n | t_{n-1})$, to be compared directly with the average acceleration measurement, $AV(t_n)$. Note that, for this filter, the R^* and H terms of Eq. (4.52) no longer contain the Δt expressions.

5.4 SIMULATION RESULTS

There were two basic evaluations of the 1-g simulation performed. The first evaluation consisted of four simulation runs to determine the filter performance with respect to the initial state estimate $\hat{x}(0) = \bar{x}_0$. In each case, the vector difference between the initial guess \bar{x}_0 and the true value of the initial state mean x_0 , given in Table 5.2, was increased. The second evaluation was a comparison of the results obtained from the basic filter of Figure 4.3 and the alternate filter of Figure 5.4. The comparison was made to show the effect of the Δv approximation on filter performance.

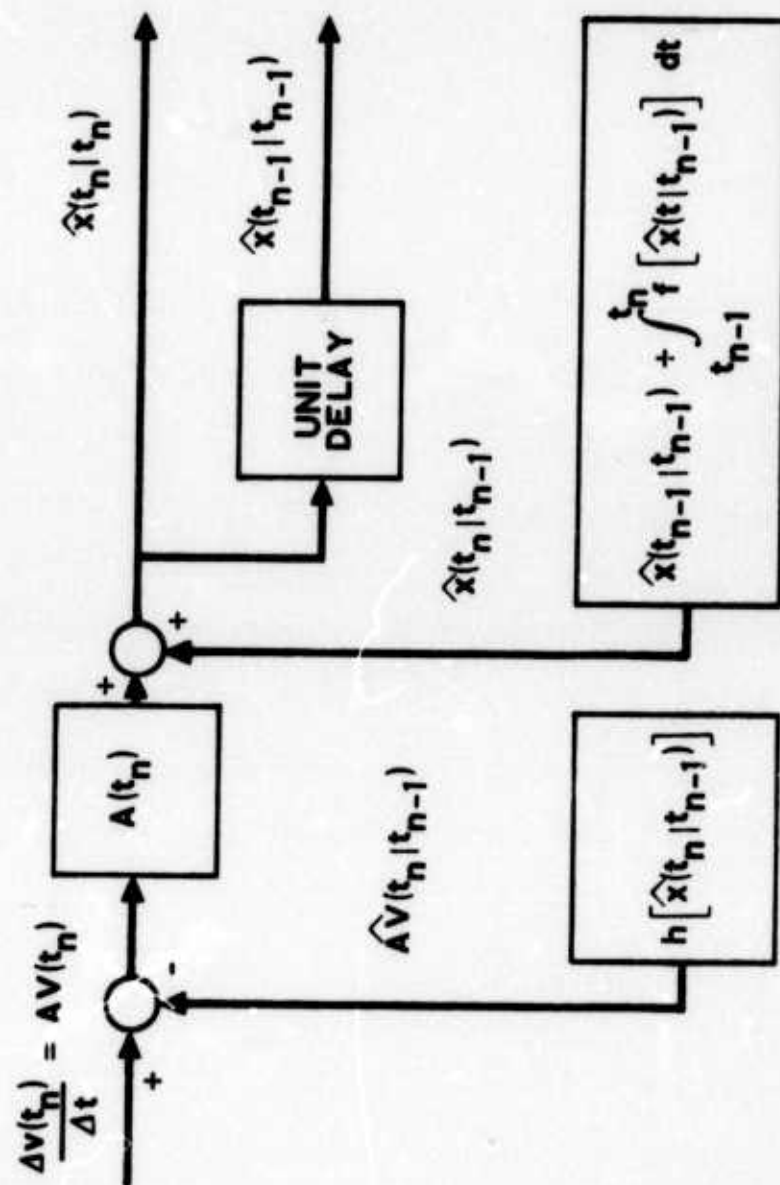


Figure 5.4. Schematic of the Alternate Extended Kalman Filter Algorithm

For the first evaluation, Table 5.5 shows the value of the initial guess \bar{x}_0 for each state variable. Except for the accelerometer scale factors, which were assumed to be $1 \times 10^6 \mu\text{g/g}$ for each simulation run, the other 14 elements of \bar{x}_0 were varied by a percentage of x_0 . Determining whether the percent variation would be above or below the true value of x_0 was done by random choice (i.e., a flip of a coin), except for the 100-percent case, where all values except the scale factors were set to zero.

The results of the 10-percent case are given in Table 5.6. \hat{x} is the filtered estimate and x is the true or simulated value of the state associated with the 6200th measurement cycle. The estimation error $\tilde{x} = x - \hat{x}$ is either below or approximately midway in the Carousel VB error budget range for every sensor parameter. The standard deviation column σ is the square root of the diagonal elements in the filtering error covariance matrix \bar{P} . From Eqs. (4.42) and (4.46), we see that \bar{P} is associated with the state perturbation sequence $\delta x(t_n)$. Therefore, an expression for the filtering error is

$$\delta \tilde{x}(t_n | t_n) = \delta x(t_n) - \delta \hat{x}(t_n | t_n) \quad (5.23)$$

If the perturbations are "small", then, from Eqs. (4.40) and (4.49), we see that

$$\begin{aligned} \delta x(t_n) &= x(t_n) - \hat{x}(t_n | t_{n-1}) \\ \delta \hat{x}(t_n | t_n) &= \hat{x}(t_n | t_n) - \hat{x}(t_n | t_{n-1}) \end{aligned} \quad (5.24)$$

Table 5.5. Values of Initial State Estimate for 1-g Simulation

State Variable	True x_0	\bar{x}_0 10% of x_0	\bar{x}_0 30% of x_0	\bar{x}_0 60% of x_0	\bar{x}_0 100% of x_0	Units
DFX	490.0	441.0	343.0	784.0	0.0	meru
DFY	520.0	572.0	364.0	208.0	0.0	meru
DFZ	110.0	99.0	77.0	44.0	0.0	meru
DIX	72.0	79.2	50.4	115.2	0.0	meru/g
DIY	68.0	61.2	88.4	27.2	0.0	meru/g
DIZ	62.0	55.8	80.6	24.8	0.0	meru/g
K0X	3500.0	3150.0	2450.0	5600.0	0.0	μg
K0Y	4250.0	4675.0	5525.0	6800.0	0.0	μg
K0Z	6310.0	5679.0	8203.0	2524.0	0.0	μg
K1X	999840.0	1000000.0	1000000.0	1000000.0	1000000.0	$\mu\text{g/g}$
K1Y	999900.0	1000000.0	1000000.0	1000000.0	1000000.0	$\mu\text{g/g}$
K1Z	998900.0	1000000.0	1000000.0	1000000.0	1000000.0	$\mu\text{g/g}$
η_{x_0}	260.0	286.0	182.0	416.0	0.0	arc-sec
ψ_{x_i}	305.0	274.0	396.0	122.0	0.0	arc-sec
α	180.0	162.0	126.0	72.0	0.0	arc-sec
β	110.0	99.0	143.0	44.0	0.0	arc-sec
γ	120.0	108.0	84.0	192.0	0.0	arc-sec

Table 5.6. Results of 10-Percent Case for 1-g Simulation *

State Variable	\hat{x}	σ	x	$x - \hat{x}$	Error Budget	Units
DFX	496.773	0.516	497.633	0.859	2.0 - 6.93	meru
DFY	513.773	0.368	514.110	0.337	2.0 - 6.93	meru
DFZ	111.850	0.383	111.448	-0.402	2.0 - 6.93	meru
DX	79.111	1.730	79.310	0.200	2.25 - 7.80	meru/g
DIY	71.280	1.800	71.826	0.545	2.25 - 7.80	meru/g
DIZ	59.402	2.082	60.219	0.818	2.25 - 7.80	meru/g
K _{0X}	3516.932	6.335	3504.268	-12.664	25.0 - 86.6	μ g
K _{0Y}	4239.670	13.400	4191.698	-47.972	25.0 - 86.6	μ g
K _{0Z}	6243.403	5.198	6242.021	-1.382	25.0 - 86.6	μ g
K _{1X}	999889.55	7.12	999873.51	-16.04	25.0 - 86.6	μ g/g
K _{1Y}	999957.72	14.15	999905.84	-51.87	25.0 - 86.6	μ g/g
K _{1Z}	998969.16	7.47	998953.54	-15.62	25.0 - 86.6	μ g/g
η_{x_0}	257.454	7.443	245.356	-12.099	17.3	arc-sec
ψ_{x_1}	310.528	2.514	315.715	5.187	13.0	arc-sec
α	-609446.50	9.44	-609458.58	-12.08		arc-sec
β	-57158.61	168.98	-57091.14	67.46		arc-sec
γ	-169021.82	33.31	-169004.95	16.87		arc-sec

N = 6200 cycles

Time = 1 hr 43 min 20 sec

* The 10-percent case means that the initial state estimates are in error by 10% of the actual values. Similar interpretations apply to Tables 5.8, 5.9 and 5.10.

Substituting the equations of Eq. (5.24) into Eq. (5.23) gives

$$\delta\tilde{x}(t_n | t_n) = x(t_n) - \hat{x}(t_n | t_n) \equiv \tilde{x} \quad (5.25)$$

Since the mean value of \hat{x} is identical to the mean value of x , taking the expectation of Eq. (5.25) would show that the filtering error and therefore the estimation error sequences have zero means. Hence, a comparison of \tilde{x} (i. e., $x - \hat{x}$) with σ should give an indication of how well the filter is performing with respect to the validity of the linearization and the effect of the Δv approximation. A comparison of \tilde{x} and σ in Table 5.6 shows that, except for K_{0Y} and K_{1Y} , the filter appears to be performing quite well. This question still remains, however: what is causing the degradation in the above parameters? One logical conclusion is that either the Δv approximation or linearization is affecting the estimates of K_{0Y} and K_{1Y} or possibly the value of Q is too high for these terms, as discussed in the last section.

Most textbooks on estimation theory discuss the value of the diagonal terms of \overline{P} (which are equal to σ^2) in assessing the filter performance. If the variance terms are getting smaller with time, the estimates will approach an optimal value for a linear application. A question arises as to whether the off-diagonal terms contain any information in regard to filter performance for linear or nonlinear applications. As mentioned in Section 4, one concern of the calibration problem was observability. Because of this, the computer

printout of the \bar{P} matrix was restructured to give the standard deviation along the diagonal and the correlation coefficient ρ of each estimation error state, with respect to every other state, in the off-diagonal terms. The correlation coefficient ρ_{ij} between two random variables x_i and x_j is [18]

$$\rho_{ij} = \frac{\text{cov}(x_i, x_j)}{\sigma_i \sigma_j} \quad (5.26)$$

where

$\text{cov}(x_i, x_j)$ - is the covariance of x_i and x_j

$$0 \leq |\rho_{ij}| \leq 1.0$$

The result of restructuring \bar{P} provided an excellent basis for studying the interrelationships and influence patterns that exist between each estimation error state.

Table 5.7 gives the accelerometer parameter correlation pattern for the three sensors. The correlation coefficient values are from the restructured \bar{P} matrix for the 6200th measurement cycle. The reason for the degradation of K_{0Y} and K_{1Y} now becomes apparent from the value of 0.94 for their correlation coefficient. In other words, the filter is having difficulty distinguishing between them. Since they are both gaussian random variables their associated \tilde{x}_i are gaussian, and hence correlation implies dependence [16]. An examination of Eq.

Table 5.7. Accelerometer Parameter Correlation Pattern for 1-g Simulation

	K_{0X}	K_{0Y}	K_{0Z}	K_{1X}	K_{1Y}	K_{1Z}	ψ_{x_i}
K_{0X}	*	0.64	0.46	0.32	0.57	0.45	0.59
K_{0Y}	0.64	*	0.29	0.39	0.94	0.54	0.39
K_{0Z}	0.46	0.29	*	0.36	0.096	0.082	0.12
K_{1X}	0.32	0.39	0.36	*	0.57	0.22	0.75
K_{1Y}	0.57	0.94	0.096	0.57	*	0.39	0.53
K_{1Z}	0.45	0.54	0.082	0.22	0.39	*	0.12
ψ_{x_i}	0.59	0.39	0.12	0.75	0.53	0.12	*

(5.5) confirms this fact. The relationship of $K_{0Y}(x_8)$ and $K_{1Y}(x_{11})$ is contained in the h_2 equation. The torque profile is driving the y_p axis of the platform from horizontal to -90 deg. As the y_p axis gets close to -90 deg, the change in the contribution of the E_{23} term (which represents the amount of applied g) becomes very small, because of the $\sin \alpha$ ($\alpha = x_{15}$) term. This means that the $K_{0Y} + K_{1Y} E_{23}$ term "looks like" a single bias term, in other words, a linear combination of two constant terms. It is not until α is of such magnitude that y_p is close to the horizontal that the change in E_{23} becomes large enough for the filter to distinguish between the two terms, which implies a decrease in ρ . Note that $\beta = x_{16}$ is usually less than 20 deg, so that $\cos \beta$ is close to 1.0 . The following list of α versus ρ (for K_{0Y} and K_{1Y}) taken from simulation data shows the change in correlation as a function of the torque profile.

α	ρ
0°	0.0033
-78°	0.52
-90°	0.79
-106°	0.97
-169°	0.94 (N = 6200)
-223° (43° above horizontal)	0.71

We now see how command torquing can be used to offset the observability problem.

Based on the above, it is concluded that the degradation of the estimates of K_{0Y} and K_{1Y} is due to the observability effect, rather than the linearization or Δv approximation. Hence, the results show that the linearization is valid and the effect of the Δv approximation in the gain computation is minimal. The important point is that the off-diagonal terms have provided a new dimension in assessing filter performance.

Table 5.8 contains the results of the 30-percent case. Since the correlation pattern of Table 5.7 also holds in this case, we see how the observability effect has again degraded the estimates of K_{0Y} and K_{1Y} . It is interesting to note the improvement in the estimates of η_{x_0} and ψ_{x_i} for the 30-percent case compared to the 10-percent case.

Comparing the \tilde{x} results of Tables 5.6 and 5.8, we see that the estimates for K_{1X} are essentially the same, but the estimate for K_{0X} has improved \tilde{x} by approximately two-thirds. The improvement in K_{0X} has an effect on ψ_{x_i} , as shown by h_1 of Eq. (5.5), and therefore the estimate of ψ_{x_i} should improve. The same holds true for η_{x_0} , which is related to D_{FX} and D_{IX} . The \tilde{x} results show that the estimates of D_{FX} are essentially the same, but the estimate for D_{IX} has improved \tilde{x} by a factor of four. Equation (5.2) shows that an improvement in D_{IX} should improve the estimate of η_{x_0} .

The results of Table 5.8 show, once again, that the linearization is valid and the effect of the Δv approximation is minimal. Even with the slight degradation in the estimates of K_{0Y} and K_{1Y} , the estimation

Table 5.8. Results of 30-Percent Case for 1-g Simulation

State Variable	\hat{x}	σ	x	$x - \hat{x}$	Error Budget	Units
DFX	496.635	0.516	497.633	0.998	2.0 - 6.93	meru
DFY	513.557	0.368	514.110	0.553	2.0 - 6.93	meru
DFZ	111.683	0.383	111.448	-0.235	2.0 - 6.93	meru
DX	79.253	1.727	79.310	0.058	2.25 - 7.80	meru/g
DY	71.160	1.797	71.826	0.665	2.25 - 7.80	meru/g
DZ	59.359	2.077	60.219	0.860	2.25 - 7.80	meru/g
K0X	3508.775	6.335	3504.268	-4.506	25.0 - 86.6	μg
K0Y	4260.383	13.408	4191.698	-68.685	25.0 - 86.6	μg
K0Z	6245.022	5.198	6242.021	-3.001	25.0 - 86.6	μg
K1X	999890.08	7.12	999873.51	-16.57	25.0 - 86.6	$\mu g/g$
K1Y	999979.94	14.16	999905.84	-74.09	25.0 - 86.6	$\mu g/g$
K1Z	998975.52	7.47	998953.54	-21.98	25.0 - 86.6	$\mu g/g$
η_{x_0}	245.112	7.445	245.356	0.244	17.3	arc-sec
η_{x_1}	314.863	2.515	315.715	0.852	13.0	arc-sec
α	-609440.88	9.43	-609438.58	-17.70		arc-sec
β	-57193.37	168.56	-57091.14	102.22		arc-sec
γ	-169029.41	33.24	-169004.95	24.46		arc-sec

N = 6200 cycles

Time = 1 hr 43 min 20 sec

error of each sensor parameter is below or within the Carousel VB error budget. Component tests are conducted, in addition to preliminary platform checkout tests, prior to the 1-g calibration, implying that knowledge of the sensor parameter magnitudes should be within 30 percent for establishing an initial guess \bar{x}_0 . Therefore, the 30-percent case should be quite representative of an actual laboratory calibration program. It should be noted that for both the 30-percent and 10-percent cases, the total filtering time was slightly over 1 hour and 43 minutes. Platform calibrations being performed for industrial and military applications require 24 to 48 hours to obtain sensor parameters. Keeping in mind that the results given here are based on simulated measurement data, the reduction in calibration time still appears significant.

Table 5.9 contains the results of the 60-percent case. Since we know from the last case that the filter converges to within the error budget from an initial condition of 30 percent of x_0 , our only concern here is that the estimates are at least within 30 percent of x . Hence, instead of the error budget column, a "% of x " is shown. We see that all the parameters, except the misalignment angles, are within 10 percent. The angles are within 28 percent. As indicated by the asterisk, eight of the 14 parameters are within the error budget. Notice that the filtering time is only 7 minutes longer than the 10-percent and 30-percent cases. The \bar{P} variances indicated that the filter was still converging at the final cycle.

The results of the 100-percent case are in Table 5.10. The filtering time was increased by approximately 17 minutes over the

Table 5.9. Results of 60-Percent Case for 1-g Simulation

State Variable	\bar{x}	σ	N	$x - \bar{x}$	% of x	Units
DFX	495.466	0.527	497.681	2.215*	0.4	meru
DFY	514.717	0.283	514.109	-0.608*	0.1	meru
DFZ	113.644	0.391	111.485	-2.159*	1.9	meru
DIX	80.365	1.640	79.249	-1.116*	1.4	meru/g
DIY	71.319	1.746	71.990	0.671*	0.9	meru/g
DIZ	59.279	2.018	60.244	0.965*	1.6	meru/g
KOX	3650.730	6.179	3503.438	-147.292	4.2	μ g
KOY	4498.232	12.183	4192.156	-306.076	7.3	μ g
KOZ	6195.416	5.401	6241.252	45.836*	0.7	μ g
K1X	999940.03	6.85	999873.30	-66.73*	0.007	μ g/g
K1Y	1000209.24	12.80	999905.98	-303.26	0.03	μ g/g
K1Z	99902.60	7.63	998953.02	-109.59	0.01	μ g/g
τ_{X_0}	312.307	7.375	245.152	-67.155	27.4	arc-sec
ϕ_{X_1}	278.137	2.493	315.543	37.406	11.9	arc-sec
α	-665368.96	5.28	-665437.69	-68.73		arc-sec
β	-60458.96	173.58	-60369.18	69.78		arc-sec
γ	-187580.62	15.55	-187534.86	45.76		arc-sec

N = 6600 cycles

Time = 1 hr 50 min

* Indicates $x - \bar{x}$ (\bar{x}) is within error budget

Table 5.10. Results of 100-Percent Case for 1-g Simulation

State Variable	\bar{x}	σ	x	$x - \bar{x}$	% of x	Units
DFX	494.927	0.442	497.508	2.580*	0.5	meru
DFY	512.597	0.237	514.138	1.541*	0.3	meru
DFZ	112.255	0.418	111.747	-0.508*	0.4	meru
DI _X	67.379	1.049	79.280	11.901	15.0	meru/g
DI _Y	60.095	1.111	71.645	11.550	16.2	meru/g
DI _Z	46.901	1.219	60.549	13.648	22.5	meru/g
K _{0X}	3436.020	5.298	3503.198	67.177*	1.9	μg
K _{0Y}	4111.232	6.570	4192.535	81.302*	1.9	μg
K _{0Z}	6288.163	5.881	6242.950	-45.213*	0.7	μg
K _{1X}	999852.38	6.67	999872.76	20.38*	0.002	μg/g
K _{1Y}	999837.07	7.00	999906.32	69.25*	0.007	μg/g
K _{1Z}	998927.07	7.28	998954.23	27.16*	0.003	μg/g
η_{x_c}	187.508	7.193	245.279	57.771	23.5	arc-sec
ψ_{x_i}	330.994	2.365	315.684	-15.310	4.8	arc-sec
α	-802561.57	36.24	-802154.33	407.24		arc-sec
β	-84749.28	88.35	-83832.86	916.41		arc-sec
γ	-231740.46	89.92	-232708.19	-967.72		arc-sec

N = 7600 cycles

Time = 2 hr 6 min 40 sec

* Indicates $x - \bar{x}$ (\bar{x}) is within error budget

60-percent case. The results show that nine of the 14 parameters are within the error budget and four of the last five are very close to the error budget. All parameters are within 23 percent of x . The important point about the 100-percent case is that it truly represents a worst case condition, since we assume no knowledge of the sensor parameters for the initial condition. The results of the 100-percent case indicate that the 1-g calibration problem is quite stable with respect to the initial state estimate.

The second evaluation consists of a single simulation run of the alternate filter of Figure 5.4. All the conditions of the 30-percent case of the basic filter were duplicated, so that the only difference was that the Δv approximation was removed from the gain computation and located in the measurement prediction loop, as shown in Figure 5.4. The results of the alternate filter are shown in Table 5.11, along with the results obtained from the basic filter, which were extracted from Table 5.8. A comparison of the estimation error values shows that the Δv approximation in the predicted measurement loop definitely degrades filter performance. Note that five of the alternate filter parameters are within the error budget. It appeared that there was a remote possibility that the alternate filter would converge; however, the loss of filtering efficiency is apparent. Note the difference in the estimation error for the Euler angles. The alternate filter is obviously not tracking the platform nearly as well as the basic filter. This concludes the 1-g simulation results.

Table 5.11. Comparison of Basic and Alternate Filters for Δv Approximation

<u>State Variable</u>	<u>\tilde{x} of Basic Filter</u>	<u>\tilde{x} of Alternate Filter</u>	<u>Units</u>
D_{FX}	0.998	25.877	meru
D_{FY}	0.553	8.079	meru
D_{FZ}	-0.235	-10.311	meru
D_{IX}	0.058	90.223	meru/g
D_{IY}	0.665	89.070	meru/g
D_{IZ}	0.860	110.043	meru/g
K_{0X}	-4.506	-21.171*	μg
K_{0Y}	-68.685	-128.034	μg
K_{0Z}	-3.001	-7.856*	μg
K_{1X}	-16.57	-54.03*	$\mu g/g$
K_{1Y}	-74.09	-155.81	$\mu g/g$
K_{1Z}	-21.98	-18.79*	$\mu g/g$
η_{x_0}	0.244	0.608*	arc-sec
ψ_{x_i}	0.852	15.157	arc-sec
α	-17.70	-634.69	arc-sec
β	102.22	9230.82	arc-sec
γ	24.46	1825.49	arc-sec

N = 6200 cycles

Time = 1 hr 43 min 20 sec

*Indicates parameters of Alternate Filter where \tilde{x} is within error budget.

SECTION 6

SIMULATION OF A CENTRIFUGE CALIBRATION

The results of a 10-state simulation of an operating centrifuge calibration are given in this section. The measurement data was generated by simulating the platform motion due to error drift, earth-rate input, and a prespecified command-torquing profile for the centrifuge operating at the 10-g level. The basic purpose of the centrifuge simulation is to determine the ability of the filtering algorithm to identify and estimate the higher-order error coefficients. In addition to the above, the program was formulated into three different options to permit an evaluation of the various types of fixed and first-order coefficients in combination with the higher-order terms.

6.1 SIMULATION STATES AND EQUATIONS

The nine sensor parameters and three Euler angles considered for the centrifuge simulation are defined in Table 6.1. The first four state variables are fixed and first-order error coefficients that are combined with the higher-order coefficients in three program options to be defined later. These coefficients were included for two reasons: first, to determine how well the data reduction technique obtains estimates of the fixed and first-order coefficients in the centrifuge environment; second, to determine if an observability problem exists between the lower- and higher-order coefficients, which would degrade the estimates. State variables three through nine are the second- and third-order gyro and accelerometer coefficients. Note that representation of both in-axis and cross-axis second-order terms for both sensors

Table 6. 1. States of the Centrifuge Simulation

State Variable Designation	Symbol	Description	Units
x_1	D_{FX}	X-gyro fixed drift	meru
x_2	K_{0X}	X-accelerometer bias	μg
x_3	D_{IX}	X-gyro input axis unbalance	meru/g
x_4	K_{1X}	X-accelerometer scale factor	$\mu g/g$
x_5	D_{OXY}	Y-gyro output axis compliance	meru/g ²
x_6	D_{ISZ}	Z-gyro input/spin cross compliance	meru/g ²
x_7	K_{2Y}	Y-accelerometer squared term	$\mu g/g^2$
x_8	K_{3Z}	Z-accelerometer cubic term	$\mu g/g^3$
x_9	K_{1PX}	X-accelerometer input/pendulous cross term	$\mu g/g^2$
x_{10}	α	Euler angle about X platform axis	arc-sec
x_{11}	β	Euler angle about Z platform axis	arc-sec
x_{12}	γ	Euler angle about Y platform axis	arc-sec

has been included along with the accelerometer cubic coefficient. The last three state variables are the Euler angles required for platform tracking. As was the case for the 1-g simulation, the purpose of the centrifuge simulation was to validate the data reduction method. Therefore, a sufficient number of states were included to represent all the basic types of higher-order coefficients normally determined from a physical centrifuge test; however, the total number of states was limited to keep the complex task of structuring and analyzing the filter tractable.

All the sensor misalignment angles were assumed to be zero and the torquer scale factors were assumed to be unity to limit the number of states. For the reasons given in Section 5.1 of Section 5, the models contained in the state and measurement dynamics of the predicted filter loops were assumed identical to those used to generate the measurement data, and the servo error term of Eq. (2.33) was assumed to be zero.

The state variables for each of the three program options are given in Table 6.2. Since only 10 states were evaluated for each option, the first column of Table 6.2 merely shows the location of the specified state variables in the 10-element state vector $\underline{x}(t)$. In other words, for the Basic Option: x_3 is the first element of the state vector, x_4 is the second element, and so forth. All equations in this section will be in terms of the state variables of Table 6.1. The analytic partials, contained in Section C.2 of Appendix C, are in terms of the same state variables. So that there is no confusion, any time we are referring to the subscripted variable x_i , it will be clearly identified

Table 6.2. State Variables for Three Program Options

Filter State Vector Element No.	Basic Option State Variables	Option 1 State Variables	Option 2 State Variables
1	$x_3(D_{IX})$	$x_1(D_{FX})$	$x_2(K_{OX})$
2	$x_4(K_{IX})$	$x_4(K_{IX})^*$	$x_3(D_{IX})$
3	$x_5(D_{OOY})$	$x_5(D_{OOY})$	$x_5(D_{OOY})^{**}$
4	$x_6(D_{ISZ})$	$x_6(D_{ISZ})$	$x_6(D_{ISZ})$
5	$x_7(K_{2Y})$	$x_7(K_{2Y})$	$x_7(K_{2Y})$
6	$x_8(K_{3Z})$	$x_8(K_{3Z})$	$x_8(K_{3Z})$
7	$x_9(K_{IPX})$	$x_9(K_{IPX})$	$x_9(K_{IPX})$
8	$x_{10}(\alpha)$	$x_{10}(\alpha)$	$x_{10}(\alpha)$
9	$x_{11}(\beta)$	$x_{11}(\beta)$	$x_{11}(\beta)$
10	$x_{12}(\gamma)$	$x_{12}(\gamma)$	$x_{12}(\gamma)$

* Note elements 2 through 10 are same as Basic Option

** Note elements 3 through 10 are same as Basic Option

in the text material whether we are referring to the state variables of Table 6.1 or to an element of a state vector such as $\underline{x}(t)$, $\hat{\underline{x}}(t)$, or $\hat{\underline{x}}^*(t)$. For example, in Section C.2, the analytic partials of the state function F are evaluated at the filtered estimate $\hat{\underline{x}}$. Since the analytic partials are in terms of the state variables, Table 6.2 shows that, when we evaluate F for the Basic Option, we replace the state variable x_3 in the partial equations with the first element of the filtered state vector \hat{x}_1 . This is shown in Appendix C by the defining equation $x_3 \equiv \hat{x}_1$, which means replacing state variable x_3 by the first element of the filtered state vector.

Since the major portion of the platform error drift is due to the contribution from the fixed and first-order terms, those terms that were not designated as state variables were added to the simulation as constant inputs, so that the platform drift is representative of the actual magnitude expected during a centrifuge calibration. The input constants common to all three options are shown in the first column of Table 6.3. Note that D_{OZ} rather than D_{IZ} was arbitrarily chosen to represent the mass unbalance term for the Z gyro. In addition to the above, those state variables not included in a specific program option were also set equal to a constant value, as shown in columns two through four of Table 6.3. In other words, for the Basic Option, state variables x_1 and x_2 are not used in the filter state vector; therefore, they were set equal to the constant values specified in column two. Hence, any time an equation contains the symbolized form of the sensor parameters (i.e., D_{FX} , K_{OX} , etc.), the constant values of Table 6.3 are used. For example, in the expression

Table 6. 3. Input Constants for Centrifuge Simulation

Input Constants Common to All Options	Additional Constants Basic Option	Additional Constants Option 1	Additional Constants Option 2
$D_{FY} = 520.0 \text{ meru}$	$x_1 \equiv D_{FX} = 490.0 \text{ meru}$	$x_2 \equiv K_{0X} = 3500.0 \mu\text{g}$	$x_1 \equiv D_{FX} = 490.0 \text{ meru}$
$D_{FZ} = 110.0 \text{ meru}$	$x_2 \equiv K_{0X} = 3500.0 \mu\text{g}$	$x_3 \equiv D_{IX} = 72.0 \text{ meru/g}$	$x_4 \equiv K_{1X} = 999840.0 \mu\text{g/g}$
$D_{IY} = 68.0 \text{ meru/g}$			
$D_{OZ} = 62.0 \text{ meru/g}$			
$K_{0Y} = 4250.0 \mu\text{g}$			
$K_{0Z} = 6310.0 \mu\text{g}$			
$K_{1Y} = 999900.0 \mu\text{g/g}$			
$K_{1Z} = 998900.0 \mu\text{g/g}$			

$$D_{FX} + x_3 a_{IAX}$$

x_3 refers to the state variable of Table 6. 1, and D_{FX} refers to the constant input value of Table 6. 3.

To obtain the simulation equations, we need to identify the characteristics of the centrifuge coordinate transformations defined in Section 3. The first assumption concerning the centrifuge is that we have perfect counter-rotation such that the system platform is completely isolated from the centrifuge rate. This implies that the misalignment angles and speed variations of both the main and CRP spindles and drive systems, respectively, are zero. Second, we assume that the 1-pulse-per-revolution station is perfectly aligned with the East. Third, we assume perfect alignment of the centrifuge main arm centerline, CRP X_r axis, and the 1-pulse-per-revolution station. Finally, we assume that the static and dynamic change in centrifuge radius from its nominal value is zero.

The assumptions are not as drastic as they appear. As discussed in Section 3, the spindle misalignments, drive system variations, and the arm stretch are all measurable quantities obtained by the various centrifuge systems discussed in Section 3. 1. In the case of the alignment of the centrifuge main arm, 1-pulse-per-revolution station, and the CRP axes, these are also quantities measured during the initial platform installation and alignment phase. Hence, all the above quantities amount to deterministic coordinate transformations. Since our purpose is to validate the data reduction technique, nothing is gained by complicating the platform rate equations with additional

deterministic factors. Keeping in mind that our concern in the calibration problem is not that the system is isolated from the centrifuge rate, but that we are able to determine the amount of centrifuge rate sensed by the system, so that we can account for this rate input in the platform rate equations. The best approach to that problem is to use actual centrifuge performance data to determine if the measurement accuracy of the centrifuge systems is sufficient, and, in some instances, verify that the assumed dynamic centrifuge models and coordinate transformations of Section 3 are valid. The important point is that the above approach is the next logical step to take after having validated the data reduction technique with a tractable simulation.

Based on the above assumptions, the following parameters for the centrifuge coordinate transformations can be defined. Reference Eq. (3.6), the misalignments are zero implying that $\phi_{xc} = \phi_{yc} = 0$. The 1-pulse-per-revolution station is East, implying that the astro-nomic heading $\phi_{ppr} = 90$ deg and therefore $\phi_{zc} = 0$ for Eq. (3.7). Since the main arm is aligned with the ppr station $\phi_o = 0$; and $\delta\omega_c = 0$, since the centrifuge rate ω_c is constant. Therefore, the earth-to-centrifuge transformation, Eq. (3.9), reduces to

$$C_e^c = \begin{bmatrix} \cos \omega_c t & \sin \omega_c t & 0 \\ -\sin \omega_c t & \cos \omega_c t & 0 \\ 0 & 0 & 1 \end{bmatrix} \quad (6.1)$$

Reference Eq. (3.12), $\theta_{xr} = \theta_{yr} = 0$, since the misalignments are zero. Since X_r is aligned with X_c $\theta_o = 0$; and $\delta\omega_r = 0$, since the CRP rate $\omega_r \equiv \omega_c$ is constant. Therefore, the centrifuge to CRP transformation, Eq. (3.14), reduces to

$$C_c^r = \begin{bmatrix} \cos \omega_c t & -\sin \omega_c t & 0 \\ \sin \omega_c t & \cos \omega_c t & 0 \\ 0 & 0 & 1 \end{bmatrix} \quad (6.2)$$

From Eqs. (6.1) and (6.2), we see that

$$C_c^r C_e^c = I \text{ (3} \times \text{3) identity matrix} \quad (6.3)$$

Since the arm stretch is zero, δr of Eq. (3.16) is zero; this implies that the centrifuge radius is equal to the nominal 260-inch value r_o . Finally, since the speed variations are zero and $\omega_{co} = \omega_c$, Eq. (3.17) reduces to

$$\omega_{ir}^r = C_e^r \omega_{ie}^e \quad (6.4)$$

Neglecting for now the variations due to the three program options, we obtain a general expression for the platform rate equations using the state variables of Table 6.1 and the common input constants of Table 6.3.

Combining Eqs. (3.20), (6.4), and (2.33), with the misalignment angles at zero, gives

$$\begin{aligned}
 \omega_{xp} &= -x_1 - x_3 a_{IX} - TGX - E_{12} WEC - E_{13} WES \\
 \omega_{yp} &= -D_{FY} - D_{IY} a_{IY} - x_5 (a_{OY})^2 - TGY - E_{22} WEC - E_{23} WES \\
 \omega_{zp} &= -D_{FZ} - D_{OZ} a_{OZ} - x_6 (a_{IZ})(a_{SZ}) - TGZ \\
 &\quad - E_{32} WEC - E_{33} WES
 \end{aligned}
 \tag{6.5}$$

From Eqs. (3.19) and (2.34), we obtain a general expression for the platform acceleration

$$\begin{aligned}
 A_X &= x_2 + x_4 a_{IAX} + x_9 (a_{IAX})(a_{PX}) \\
 A_Y &= K_{0Y} + K_{1Y} a_{IAY} + x_7 (a_{IAY})^2 \\
 A_Z &= K_{0Z} + K_{1Z} a_{IAZ} + x_8 (a_{IAZ})^3
 \end{aligned}
 \tag{6.6}$$

We now need to obtain expressions for the applied acceleration terms of Eqs. (6.5) and (6.6). Section B.2 of Appendix B shows that the contribution of the Group 2 terms of the applied acceleration equation, Eq. (3.25), can be neglected. From the centrifuge assumptions we know that

$$\Delta W_{cr}^{rk} = \dot{W}_{ec}^{ck} = \dot{W}_{cr}^{rk} \equiv 0
 \tag{6.7}$$

Combining Eqs. (6.3) and (6.7), the applied acceleration equation reduces to

$$A_{is}^s = C_p^s C_r^p \left\{ 2 W_{ie}^{ek} C_c^e W_{ec}^{ck} R_{cr}^c + G^e + C_c^r W_{ec}^{ck} W_{ec}^{ck} R_{cr}^c \right\} \quad (6.8)$$

From Eqs. (3.3), (6.1), (3.11), (6.2), and (3.25), the term in the brackets { } of Eq. (6.8) can be reduced to

$$A_{is}^s = C_p^s C_r^p \begin{pmatrix} r_1 \\ r_2 \\ r_3 \end{pmatrix} \quad (6.9)$$

where

$$r_1 = -\omega_c^2 r_o (\cos \omega_c t) - 2 \omega_c r_o (WES)(\cos \omega_c t)$$

$$r_2 = -\omega_c^2 r_o (\sin \omega_c t) - 2 \omega_c r_o (WES)(\sin \omega_c t)$$

$$r_3 = g + 2 \omega_c r_o (WEC)(\sin \omega_c t)$$

The expressions for r_1 , r_2 , and r_3 can be simplified, since we know the centrifuge angular rate ω_c at the 10-g level and the nominal radius r_o . The components of earth-rate, WEC and WES, are defined by Eq. (3.3).

Given

$$\omega_c = 3.8505954 \text{ rad/sec}$$

$$r_o = 260/12 \text{ ft}$$

$$WES = 3.95990552 \times 10^{-5} \text{ rad/sec}$$

$$WEC = 6.1232531 \times 10^{-5} \text{ rad/sec}$$

$$g = 32.1232531 \text{ ft/sec}^2 = 1 \text{ (g-units)}$$

We convert the constants to g-units and obtain

$$r_1 = -G1(\cos \omega_c t)$$

$$r_2 = -G1(\sin \omega_c t) \quad (6.10)$$

$$r_3 = 1.0 + G2(\sin \omega_c t)$$

where

$$G1 = 10.00020568 \text{ g's}$$

$$G2 = 0.00031805 \text{ g's}$$

Now C_r^p is the Euler transformation matrix and C_p^s is the sensor transformations defined by Eqs. (3.19) and (3.20). Therefore, we can now solve for the components of applied acceleration.

$$a_{IX} = a_{IAX} = a_{OZ} \equiv AX$$

$$a_{IY} = a_{IAY} = a_{SZ} \equiv AY$$

$$a_{IZ} = a_{IAZ} \equiv AZ \quad (6.11)$$

$$a_{OY} = a_{PX} \equiv -AZ$$

where

$$AX = -G1[E_{11}(\cos \omega_c t) + E_{12}(\sin \omega_c t)] + E_{13}[1.0 + G2(\sin \omega_c t)]$$

$$AY = -G1[E_{21}(\cos \omega_c t) + E_{22}(\sin \omega_c t)] + E_{23}[1.0 + G2(\sin \omega_c t)]$$

$$AZ = -G1[E_{31}(\cos \omega_c t) + E_{32}(\sin \omega_c t)] + E_{33}[1.0 + G2(\sin \omega_c t)]$$

E_{ij} ($i, j = 1, 2, 3$) - are from Eq. (4.1) with $\alpha = x_{10}$, $\beta = x_{11}$,

and $\gamma = x_{12}$

From Eqs. (6.5) and (6.11) and Table 6.2, we can obtain the platform rate equations for the various program options.

BASIC AND OPTION 2

$$\omega_{xp} = -D_{FX} - x_3(AX) - TGX - E_{12}WEC - E_{13}WES$$

OPTION 1

$$\omega_{xp} = -x_1 - D_{IX}(AX) - TGX - E_{12}WEC - E_{13}WES \quad (6.12)$$

FOR ALL OPTIONS

$$\omega_{yp} = -D_{FY} - D_{IY}(AY) - x_5(AZ)^2 - TGY - E_{22}WEC - E_{23}WES$$

$$\omega_{zp} = -D_{FZ} - D_{OZ}(AX) - x_6(AZ)(AY) - TGZ - E_{32}WEC - E_{33}WES$$

We see that only ω_{xp} is affected by the program options. With the platform rates defined by Eq. (6.12), we can define the state vector equation directly from Eq. (4.8).

$$\dot{\underline{x}} = \underline{f}(\underline{x}, t) + \underline{w}(t) \quad (6.13)$$

where

$\dot{\underline{x}}$ and \underline{w} - are 10-element vectors constructed according to the options of Table 6.2

$\underline{f}(\underline{x}, t)$ - is a 10-element vector-valued function constructed according to the selected option.

The only difference between Eq. (6.13) and Eq. (4.8) is the dimensionality of the equation. We know from Section 4 that the first seven elements of \underline{f} are zero, and the last three elements contain the dynamics of the system platform rates.

$$\begin{aligned} f_8 &= (\omega_{xp} \cos x_{12} + \omega_{zp} \sin x_{12}) / \cos x_{11} \\ f_9 &= \omega_{zp} \cos x_{12} - \omega_{xp} \sin x_{12} \end{aligned} \quad (6.14)$$

$$f_{10} = (\omega_{xp} \cos x_{12} \sin x_{11} + \omega_{zp} \sin x_{12} \sin x_{11}) / \cos x_{11} + \omega_{yp}$$

The equation for ω_{xp} in Eq. (6.14) is based on the program option as shown in Eq. (6.12). The statistical description of Eq. (6.13) is identical to Eq. (4.8) with the dimensionality adjusted from 63 to 10.

The measurement equation for the various program options is obtained from Eqs. (6.6) and (6.11) and Table 6.2.

BASIC AND OPTION 1

$$h_1 = K_{0X} + x_4(t_n)[AX(t_n)] - x_9(t_n)[AX(t_n) \bullet AZ(t_n)]$$

OPTION 2

$$h_1 = x_2(t_n) + K_{1X}[AX(t_n)] - x_9(t_n)[AX(t_n) \bullet AZ(t_n)] \quad (6.15)$$

FOR ALL OPTIONS

$$h_2 = K_{0Y} + K_{1Y}[AY(t_n)] + x_7(t_n)[AY(t_n)]^2$$

$$h_3 = K_{0Z} + K_{1Z}[AZ(t_n)] + x_8(t_n)[AZ(t_n)]^3$$

We see that only h_1 is affected by the program options. The measurement equation is identical to Eq. (4.14) with $h[\underline{x}(t_n), t_n]$ defined by Eq. (6.15) and the selected program option.

6.2 MEASUREMENT SIMULATION

Except for the elements of the state and measurement equations, the measurement simulation is identical to the 1-g simulation development described in Section 5.2 of Section 5. Table 6.4 contains a list of the means and standard deviations for the state variables. These values were used to construct the 10-element initial state vector $\underline{x}(t_0)$, based on the specified program option. As was the case in Section 5, the values are based on data from the Carousel VB system.

Table 6.5 contains a list of the standard deviations for the zero-mean, gaussian white disturbance process $\underline{w}(t)$ and the zero-mean,

Table 6.4 Initial State Means and Standard Deviations

State Variable	Symbol	Mean Value (x_0)	Standard Deviation (σx_0)	Units
x_1	D_{FX}	490.0	6.0	meru
x_2	K_{0X}	3500.0	30.0	μg
x_3	D_{IX}	72.0	4.0	meru/g
x_4	K_{1X}	999840.0	30.0	$\mu g/g$
x_5	D_{OOY}	4.0	0.2	meru/g ²
x_6	D_{ISZ}	3.0	0.1	meru/g ²
x_7	K_{2Y}	12.0	2.0	$\mu g/g^2$
x_8	K_{3Z}	3.0	0.5	$\mu g/g^3$
x_9	K_{IPX}	5.0	1.0	$\mu g/g^2$
x_{10}	α	180.0	5.0	arc-sec
x_{11}	β	110.0	5.0	arc-sec
x_{12}	γ	120.0	5.0	arc-sec

Table 6.5. Standard Deviations of Disturbance and Measurement Noise

Disturbance (w) Number	Standard Deviation (σ_w)	Units	Measurement Noise (m) Number	Standard Deviation (σ_m)	Units
1	0.6	meru	1	13.0	$\mu\text{g-sec}$
2	3.0	μg	2	13.0	$\mu\text{g-sec}$
3	0.4	meru/g	3	13.0	$\mu\text{g-sec}$
4	3.0	$\mu\text{g/g}$			
5	0.02	meru/g ²			
6	0.01	meru/g ²			
7	0.2	$\mu\text{g/g}^2$			
8	0.05	$\mu\text{g/g}^3$			
9	0.1	$\mu\text{g/g}^2$			
10	5.0	arc-sec			
11	5.0	arc-sec			
12	5.0	arc-sec			

gaussian white, measurement noise sequence $\underline{m}(t_n)$. As was the case in Section 5, the standard deviations for the sensor parameter disturbances are 10 percent of those listed in Table 6.4. Also, since the same torque profile was used, the disturbance added each Δt measurement cycle is given by Eq. (5.7) with $i = 1, 2, \dots, 10$. The equations of the sensor parameters, Euler angles, and measurements are represented by Eqs. (5.9), (5.10), and (5.11), respectively, with the state and measurement dynamic equations given by Eqs. (6.14) and (6.15).

A measurement cycle of $\Delta t = 0.04$ second was used for the centrifuge simulation. This measurement cycle is identical to the operational measurement cycle used for the Carousel VB Inertial Measurement Unit. The method of integrating the state and measurement dynamics was 4th-order Runge-Kutta with a step-size of 0.01 second. Based on a nominal platform rate of 5.2×10^{-4} rad/sec (see Section B.2 of Appendix B) it is implied that measurements were taken every 0.07 arc-minutes of platform angle. Based on a centrifuge rate of 3.85 rad/sec, it is implied that measurements were taken every 8.8 deg of centrifuge angle. Figure 5.1 also represents the flow diagram for the centrifuge measurement simulation program with the state and measurement dynamic of Eqs. (6.14) and (6.15). Since $\Delta t = 0.04$ second, it is implied that the maximum number of measurements over the torque profile would be 328,500. Fortunately, the filter converged in less than 15,000 cycles, so that it was not necessary to process all of these measurements.

6.3 FILTER ALGORITHM

Except for the elements of the state and measurement dynamic equations, the filter algorithm is identical to the 1-g simulation development given in Section 5.3 of Section 5. Since the state dynamic equation is an explicit function of time, it is implied that F and Φ are functions of time; therefore, the matrix differential equation, Eq. (4.22), should be used to obtain a solution of Φ . As discussed in Section 4.4 of Section 4, only the elements of the last three rows of Φ require a solution via Eq. (4.22). This implies a total of 30 differential equations. In the case of Γ , the adjoint matrix differential equation, Eq. (4.27), requires the integration of 60 differential equations to obtain Φ from t_n back to t_{n-1} , as discussed in Section 4; then 60 additional integrations are required to obtain Γ from Eq. (4.26), for a total of 120 integrations. This is a formidable task just to transition the "initial guess" of $Q(0)$ forward in time. Since $Q(0)$ is an adjustable initial condition, it was decided to consider F constant over the 0.04 second measurement cycle and obtain Γ by the power series approximation of Eq. (4.29) with F evaluated at $t = t_n$.

Another approach would be to consider F constant for the Φ computation as well, then use the power series approximation of Eq. (4.24), with F evaluated at $t = t_n$, to obtain Φ . An evaluation of approximating both Φ and Γ by the power series method is important, since, for the general calibration problem containing 63 states, we are dealing with 189 integrations for Φ and 3969 integrations for Γ . Therefore, the only significant difference in Figure 5.3 for the

centrifuge simulation is that Block 10 contained two options for obtaining Φ and Γ . One option obtained both by the power series method with $m = 5$. The second option obtained Φ by a 4th-order Runge-Kutta integration of 30 differential equations using a step-size of 0.01 second, and then used the power series approximation to obtain Γ .

The partial derivative matrices of F and H are contained in Section C.2 of Appendix C. The construction of their elements is based on the specified program option. As was the case for Section 5, $\bar{P}(0)$ was assumed a diagonal matrix; $Q(0)$ and $R^*(1)$ were assumed diagonal and stationary. The scaling for $\bar{P}(0)$ and $Q(0)$ was identical to Eqs. (5.13) and (5.14), respectively, with $i = 1, 2, \dots, 10$. The scaling for $R^*(1)$ was identical to Eq. (5.15). All the procedures and equations for $\hat{x}^*(N)$, $\Delta\hat{v}(N)$, $A(N)$, and $\hat{x}(N)$ are identical to those of Section 5 with $\Delta t = 0.04$ second, an integration step-size of 0.01 second, the dimensionality reduced from 17 to 10, and the state and measurement dynamics defined by Eqs. (6.14) and (6.15).

6.4 SIMULATION RESULTS

Before discussing the detailed final results of the centrifuge simulation, the results obtained from some preliminary runs will be given to show how some of the physical aspects of the problem and the correlation data obtained from the simulations were used to improve the estimates of the centrifuge calibrations. From Table 6.4, we see that the initial values of α and γ are a few minutes of arc. To simplify the notation, we will refer to this initial condition as the $\alpha = \gamma = 0$ condition.

Table 6.6 shows the results of three simulation runs where the only difference was the initial values assigned to α and γ . For the $\alpha = \gamma = 0$ case, we see that the estimation error \tilde{x} (i.e., $x - \hat{x}$) for all the sensor coefficients except K_{3Z} appear to be quite small. In the case of K_{3Z} we are attempting to estimate a true value of $x = 3.554 \mu\text{g}/\text{g}^3$ and $\tilde{x} = 1.667 \mu\text{g}/\text{g}^3$. Obviously, the estimate is very poor. Note, however, that K_{3Z} is a coefficient associated with the Z accelerometer, and the Z platform axis is vertically up at the start of the calibration. Since the filtering time is only 5 minutes, we see from the true values of α , β , and γ that the Z axis has only moved approximately 9 deg from the vertical. This means that the Z accelerometer has sensed only the local gravity value of 1-g, compared to the other platform axes which have sensed a peak-to-peak acceleration of 20 g's. The K_{3Z} coefficient information is essentially "buried" in the noise. To correct this physical situation, the initial condition of α was changed to -45 deg, which places the Z axis 45 deg above the horizontal and permits the Z accelerometer to sense a component of centrifuge acceleration. The results of this simulation are in the $\alpha = -45 \quad \gamma = 0$ column. We can now see the significant improvement in the K_{3Z} estimation error, from 1.667 to $0.017 \mu\text{g}/\text{g}^3$. An interesting comparison can also be made with the K_{3Z} correlation pattern for the two cases. The following correlation pattern gives the sensor parameter that K_{3Z} is correlated with and the amount of correlation, ρ , for the two cases

<u>Sensor Parameter</u>	<u>$\alpha = 0$ Correlation</u>	<u>$\alpha = -45$ Correlation</u>
D_{IX}	0.45	0.063
α	0.50	0.23
γ	0.40	0.026

The correlation pattern definitely shows the estimates of K_{3Z} should be better with the Z axis 45 deg above the horizontal. Once again we see a relationship between the correlation pattern, provided by the off-diagonal \bar{P} matrix terms, and the torque profile via platform orientation.

Comparing the $\alpha = 0$ to $\alpha = -45$ $\gamma = 0$ case, we see that another problem has developed. The estimate for D_{IX} has degraded significantly. A review of the 1-g simulation results showed that the correlation pattern (especially with α) and \tilde{x} improved tremendously when $\gamma = -45$ deg. The results of the $\alpha = -45$ $\gamma = -45$ column verify the 1-g analysis and show that a significant improvement in the D_{IX} estimate has occurred, along with a further improvement in the K_{3Z} estimate. The slight degradation of K_{1X} is not significant, since approximately 260 seconds later in the $\alpha = -45$ $\gamma = -45$ run, \tilde{x} for K_{1X} drops to $-0.78 \mu\text{g/g}$ and stays there; in other words, it takes a little longer to converge the K_{1X} estimate. Once again the correlation pattern of D_{IX} for all three cases shows the relative degradation or improvement of the D_{IX} estimate with respect to the platform orientation.

Table 6.6 Improvement in Estimates Versus Platform Orientation
Based on Correlation Pattern Data

State Variable	\bar{x}	$\alpha = 0 \quad \gamma = 0$ $\bar{\tilde{x}}$	$\alpha = -45 \quad \gamma = 0$ $\bar{\tilde{x}}$	$\alpha = -45 \quad \gamma = -45$ $\bar{\tilde{x}}$	Units
D_{IX}	72.711	0.494	2.316	0.377	meru/g
K_{IX}	999801.71	0.02	-0.78	-1.30	$\mu\text{g/g}$
D_{OOY}	4.162	-0.120	-0.007	-0.003	meru/g ²
D_{ISZ}	2.870	0.035	0.006	0.002	meru/g ²
K_{2Y}	15.683	0.022	0.184	0.110	$\mu\text{g/g}^2$
K_{3Z}	3.554	1.667	0.017	0.001	$\mu\text{g/g}^3$
K_{IPX}	3.725	0.795	-0.007	0.154	$\mu\text{g/g}^2$
α	-28921.564	0.242	0.149	0.249	arc-sec
β	-5475.727	-0.248	-0.236	-0.228	arc-sec
γ	-32605.899	0.667	0.399	0.160	arc-sec

Basic Option

N = 7500 cycles

Time = 5 min

<u>Sensor Parameter</u>	$\alpha = 0$ $\gamma = 0$	$\alpha = -45$ $\gamma = 0$	$\alpha = -45$ $\gamma = -45$
	<u>Correlation</u>	<u>Correlation</u>	<u>Correlation</u>
K_{2Y}	0.076	0.54	0.061
α	0.63	0.56	0.23

Based on the above, the two program options that contain D_{IX} , Basic and Option 2, were run with the initial values of α and γ set to -45 deg. In the case of Option 1, only the initial value of α was set to -45 deg to permit recovery of the K_{3Z} term.

Nothing has been said thus far about the initial state estimate $\bar{x}_0 = \hat{x}(0)$ for the centrifuge simulations. The initial estimates for all the higher-order coefficients, state variables x_5 through x_9 , were always set equal to zero. Since we assume we know nothing about these coefficients, zero is the logical choice. For the fixed and first-order coefficients, state variables x_1 through x_4 , the initial estimate of the scale factor was always set equal to $1.0 \times 10^6 \mu\text{g/g}$, and the other three coefficients were varied by either 10 percent or 30 percent of the respective x_{0i} ($i = 1, 2, 3$) contained in Table 6.4. In the case of the Euler angles, the 10-percent or 30-percent variations of x_{0i} ($i = 10, 11, 12$) were obviously applied about the new initial values of -45 deg, rather than x_0 , for those angles with the 45-deg offset. The difference in the results from the 10-percent and 30-percent simulations is so insignificant that only the 30-percent results for the three program

options will be presented. Selection of the 30-percent case is rather conservative, since the initial estimates for the fixed and first-order coefficients will normally be provided by the precentrifuge 1-g calibration; and as was shown in Section 5, even the 100-percent case converged to within 30 percent. A worst case run was also made for the centrifuge simulation, where all the coefficient initial estimates except the scale factor and offset angles ($\alpha = \gamma = -45$ deg) were set to zero.

As discussed in the last section, there were two options available for computing Φ and Γ . The option that obtained both by the power series approximation is referred to as $\text{TOPT} = 0$, where TOPT stands for transition option. The option that obtained Φ by integration and Γ by the power series approximation will be referred to as $\text{TOPT} = 1$. Table 6.7 contains a comparison of the results of the two transition options. Since the differences are so small, all the digits available from the computer printout are provided to permit a complete comparison. The results show that assuming F to be constant over the 0.04-second measurement interval and computing Φ and Γ from the power series approximation with $m = 5$ is a valid approximation. Therefore, $\text{TOPT} = 0$ was used for all the remaining simulation runs. This result is encouraging, since the 63-state general calibration program becomes much simpler if all the integrations associated with Φ and Γ can be eliminated. It should be noted that the approximation was probably valid because of the short measurement cycle time; however, for most missile applications, the measurement cycle time ranges from 0.02 to 0.05 second in order to meet operational accuracy requirements.

Table 6.7. Comparison of Transition Options

State Variable	\bar{x}	TOPT = 0 \bar{x}	TOPT = 1 \bar{x}	Units
D _{FX}	490.991	0.15588783	0.15589020	meru
K _{1X}	999801.66	-0.19370293	-0.19369833	μg/g
D _{OOY}	4.160	-0.0016879902	-0.0016863434	meru/g ²
D _{ISZ}	2.869	0.000095586813	0.000099143620	meru/g ²
K _{2Y}	15.697	0.037962037	0.037966557	μg/g ²
K _{3Z}	3.560	-0.0098858483	-0.0098863019	μg/g ³
K _{IPX}	3.741	0.18937816	0.18938898	μg/g ²
α	-219679.75	0.034046960	0.034048778	arc-sec
β	-18817.23	0.17029650	0.17026478	arc-sec
γ	-57893.59	-0.15227250	-0.15229208	arc-sec
Option 1		N = 15,000 cycles	Time = 10 min	

Block 9 of Figure 5.3 shows that two options were available for computing the F and H partials for the filter. Table 6.8 shows the results of two simulation runs, whose only difference was that one was based on the analytic partials of Appendix C and the other was based on the numerical partial routine. It should be understood that no effort was made to improve the results of the routine, such as adjusting the incremental perturbation levels, since the basic purpose of the numerical partials was to provide a basis for comparison and checkout of the hand calculated analytic partials. The results of the numerical partials compare quite well with the analytic results, especially to one who had the "pleasure" of hand calculating the 162 partials of Appendix C. With further refinements on the numerical partial routine, a major simplification of the 63-state calibration program could be achieved using numerical partials.

The results of the 30-percent case for the Basic Option, Option 1, and Option 2 are contained in Tables 6.9, 6.10, and 6.11, respectively. Except for K_{IPX} in two program options, all the values of the estimation error, \tilde{x} , are well within the error budget. The error budget values for K_{2Y} , K_{3Z} , and K_{IPX} were obtained from the Central Inertial Guidance Test Facility at Holloman AFB, since no values were defined for the Carousel VB error budget. The values for the above accelerometer error coefficients are nominal error values that are representative of the quality of accelerometer used on the Carousel VB platform. In the case of K_{IPX} , we see that the largest value of \tilde{x} was obtained with Option 1, where the initial offset was $\alpha = -45$ deg. For

Table 6.8. Comparison of Analytic and Numerical Partial

State Variable	\bar{x}	Analytic Partial \bar{x}	Numerical Partial \bar{x}	Units
K_{0X}	3504.957	2.719	3.391	μg
D_{IX}	66.888	0.286	1.816	meru/g
D_{OOY}	4.1599216	-0.0000966	-0.0015309	meru/g ²
D_{ISZ}	2.86957	-0.00827	0.00013	meru/g ²
K_{2Y}	15.6967	0.0533	0.0999	$\mu g/g^2$
K_{3Z}	3.56042	-0.00691	-0.00988	$\mu g/g^3$
K_{IPX}	3.7412	0.0824	0.1827	$\mu g/g^2$
α	-196238.93	-0.0353	-0.1121	arc-sec
β	-56762.46	0.0573	0.1324	arc-sec
γ	-218895.65	-0.4671	-0.1399	arc-sec

Option 2 N = 15,000 cycles Time = 10 min

Table 6.9. Results of 30-Percent Case Basic Option

State Variable	\hat{x}	σ	\bar{x}	$\bar{\bar{x}}$	Error Budget	Units
D _{IX}	72.4021	0.0125	72.6609	0.2588	2.25 - 7.80	meru/g
K _{1X}	999802.45	0.03	999801.66	-0.79	25.0 - 86.6	μg/g
D _{OOY}	4.1600156	0.0002020	4.1599216	-0.0000940	0.208	meru/g ²
D _{ISZ}	2.878289	0.000609	2.869569	-0.008719	0.087	meru/g ²
K _{2Y}	15.65374	0.00414	15.69673	0.04299	0.1	μg/g ²
K _{3Z}	3.567258	0.000350	3.560426	-0.006832	0.01	μg/g ³
K _{1PX}	3.62399	0.00375	3.74119	0.11720	0.1	μg/g ²
α	-196257.39	0.01	-196257.50	-0.11		arc-sec
β	-56786.08	0.01	-56785.98	0.10		arc-sec
γ	-218890.68	0.01	-218891.12	-0.44		arc-sec

N = 15,000 cycles

Time = 10 min

Table 6.10. Results of 30-Percent Case Option 1

<u>State Variable</u>	<u>\bar{x}</u>	<u>σ</u>	<u>\bar{x}</u>	<u>Error Budget</u>	<u>Units</u>
D _{FX}	490.83616	0.00820	490.99135	2.0 - 6.93	meru
K _{1X}	999801.86	0.02	999801.66	25.0 - 86.6	μg/g
D _{OOY}	4.161611	0.000245	4.159922	0.208	meru/g ²
D _{ISZ}	2.869464	0.000317	2.869569	0.087	meru/g ²
K _{2Y}	15.65831	0.00473	15.69673	0.1	μg/g ²
K _{3Z}	3.570305	0.000472	3.560426	0.01	μg/g ³
K _{IPX}	3.55182	0.00378	3.74119	0.1	μg/g ²
α	-219679.78	0.01	-219679.75		arc-sec
β	-18817.40	0.01	-18817.23		arc-sec
γ	-57893.43	0.01	-57893.59		arc-sec

N = 15,000 cycles

Time = 10 min

Table 6.11. Results of 30-Percent Case Option 2

<u>State Variable</u>	<u>\hat{x}</u>	<u>σ</u>	<u>\underline{x}</u>	<u>$\hat{\underline{x}}$</u>	<u>Error Budget</u>	<u>Units</u>
K _{0X}	3502.207	0.113	3504.957	2.749	25.0 - 86.6	μg
D _{IX}	66.6037	0.0125	66.8685	0.2848	2.25 - 7.80	meru/g
D _{OOY}	4.1600173	0.0002019	4.1599216	-0.0000957	0.208	meru/g ²
D _{ISZ}	2.877921	0.000608	2.869569	-0.008352	0.087	meru/g ²
K _{2Y}	15.64370	0.00414	15.69673	0.05302	0.1	$\mu\text{g/g}^2$
K _{3Z}	3.567346	0.000350	3.560426	-0.006920	0.01	$\mu\text{g/g}^3$
K _{IPX}	3.65704	0.00390	3.74119	0.08415	0.1	$\mu\text{g/g}^2$
α	-196238.90	0.01	-196238.93	-0.03		arc-sec
β	-56762.52	0.01	-56762.46	0.06		arc-sec
γ	-218895.18	0.01	-218895.65	-0.47		arc-sec

N = 15,000 cycles

Time = 10 min

the Basic Option and Option 2, the initial offset was $\alpha = \gamma = -45$ deg. We see that the value of \tilde{x} is improved for the Basic Option and within the error budget for Option 2. Comparing the K_{IPX} estimation error values for the two transition options of Table 6.7, we see that the approximation of Φ is not responsible for the degradation of the K_{IPX} estimate. Table 6.6 shows significant differences in the K_{IPX} value of \tilde{x} for three different initial offset cases of the Basic Option. The significant improvement of K_{IPX} for the $\alpha = -45$ $\gamma = 0$ case appears to conflict with the results of the 30-percent case, where the worst value of \tilde{x} for K_{IPX} was obtained with Option 1, where $\alpha = -45$ deg and $\gamma = 0$ deg. The $\alpha = -45$ $\gamma = -45$ and $\alpha = -45$ $\gamma = 0$ cases were both run for a total filtering time of 10 minutes. The results at the 10-minute point were identical to those shown in Tables 6.9 and 6.10 for the Basic Option and Option 1 (i.e., $\tilde{x} = 0.11720 \mu\text{g}/\text{g}^2$ and $\tilde{x} = 0.18937 \mu\text{g}/\text{g}^2$, respectively). The interesting point is that at the 5-minute point, for the $\alpha = -45$ $\gamma = 0$ case of Table 6.6, the correlation coefficients of K_{IPX} with D_{IX} , K_{2Y} , K_{3Z} , α , and β were 2 to 3 orders of magnitude lower than those values for the $\alpha = 0$ $\gamma = 0$ and $\alpha = -45$ $\gamma = -45$ cases at the 5 minute point. Also, the correlation pattern was improved for the 30-percent Option 2 case, as compared to the 30-percent Basic Option, with respect to K_{0X} and K_{1X} , respectively. It now becomes apparent that K_{IPX} is extremely sensitive to the platform orientation and to the other accelerometer parameters along the x axis; in other words, the estimate is improved when coupled with a bias term (K_{0X}), then with a scale factor term (K_{1X}).

Now, since K_{IPX} is a cross-axis term, it is not surprising that it is highly sensitive to the platform orientation. Also, it is not surprising that the correlation pattern is improved when compared to a constant bias term, which should be easily distinguished from a second-order term when sinusoidal acceleration is applied. Therefore, the conclusion is that a more favorable orientation that decouples K_{IPX} from the other sensor parameters is required for a good estimate of the K_{IPX} coefficient.

The results of the worst or 100-percent case using the Basic Option are contained in Table 6.12. Considering that the filtering time was only increased by 5 minutes over the 30-percent case, the results are truly incredible. Four of seven coefficients are already within the error budget, and the remaining three coefficients are extremely close.

Comparing the results of \tilde{x} or σ in Tables 6.9 through 6.12, we see that the relative difference between \tilde{x} and σ is larger for the centrifuge simulation than for the 1-g simulation. In the 1-g simulation, the values of \tilde{x} , which represent the state perturbations, were about the same magnitude or smaller than the standard deviations, σ , of the filtering error. Table 6.13 gives a comparison of the 1-g and centrifuge simulation filter performance for those fixed and first-order coefficients common to both simulations. In order to have a common base for comparison, the results are compared for an equal value of N measurement cycles, rather than an equal time of filtering. In other words, we are comparing the filter performance based on the

Table 6.12. Results of 100-Percent Case Basic Option

State Variable	\hat{x}	σ	\bar{x}	\bar{x}	Error Budget	Units
D _{IX}	72.9385	0.0100	72.6413	-0.2973	2.25 - 7.80	meru/g
K _{IX}	999800.01	0.03	999801.57	1.56	25.0 - 86.6	μg/g
D _{OOY}	4.162439	0.000190	4.156025	-0.006414	0.208	meru/g ²
D _{ISZ}	2.775282	0.000606	2.866052	0.090770	0.087	meru/g ²
K _{2Y}	15.74018	0.00370	15.70872	-0.03145	0.1	μg/g ²
K _{3Z}	3.568251	0.000341	3.552326	-0.015925	0.01	μg/g ³
K _{IPX}	4.57715	0.00316	3.72551	-0.85164	0.1	μg/g ²
α	-209160.27	0.01	-209160.26	0.02		arc-sec
β	-88160.82	0.01	-88160.65	0.16		arc-sec
γ	-244663.24	0.01	-244662.95	0.29		arc-sec

N = 22,500 cycles

Time = 15 min

Table 6.13. Comparison of Filter Performance for 1-g and Centrifuge Simulations

State Variable	Case	Centrifuge Simulation		1-g Simulation		Units
		σ	\bar{x}	σ	\bar{x}	
D _{FX}	30%	0.0123	0.1747	0.5157	0.9979	meru
D _{IX}	30%	0.0221	0.4579	1.7269	0.0578	meru/g
D _{IX}	100%	0.0192	0.7932	1.0494	11.9013	meru/g
K _{0X}	30%	0.1794	7.8668	6.3350	-4.5065	μ g
K _{1X}	30%	0.0349	0.8851	7.1207	-16.5733	μ g/g
K _{1X}	100%	0.0329	12.8885	6.6711	20.3858	μ g/g

30% Case	N = 6200	{	1-g Time = 1 hr 43 min 20 sec
			Centrifuge Time = 4 min 8 sec
100% Case	N = 7600	{	1-g Time = 2 hr 6 min 40 sec
			Centrifuge Time = 5 min 4 sec

results after processing the same number of measurements: 6200 in the 30-percent case and 7600 in the 100-percent case. The results of Table 6.13 show that even though the relative difference between \tilde{x} and σ is larger for the centrifuge simulation, the values of \tilde{x} (state perturbations) for the centrifuge simulation are smaller than those of 1-g simulation in the majority of cases. Comparing the σ values of the centrifuge versus the 1-g simulation, we now see that the filter performance was vastly improved for the centrifuge simulation. In fact, the performance was so improved that the value of Q was maintained in order to prevent the filter gain from approaching zero and thereby decoupling the filtered estimates from the measurement data as discussed in Section 5.3 of Section 5.

The results of the centrifuge simulation have again verified that the linearization is valid, that the effect of the Δv approximation is minimal, and that the computation of the filter can be simplified by assuming F is constant over the measurement interval and thereby ϕ can be obtained via the power series approximation. Except for K_{IPX} , the correlation data for the centrifuge simulation showed that there is no observability problem for those coefficients considered for the centrifuge simulation. This concludes the centrifuge simulation results.

SECTION 7

SUMMARY AND RECOMMENDATIONS FOR FUTURE STUDY

The objective of the report was to investigate a data reduction technique that obtains estimates of inertial sensor error model coefficients from a laboratory calibration of an Inertial Navigation System. The results of Sections 5 and 6 reveal that this objective has been achieved; however, throughout the preceding sections, a number of simplifying model assumptions were made based on calculations of and/or assumptions made concerning sensor and platform design characteristics, assumptions of the centrifuge performance and dynamic environment, and assumptions of the statistical model used for the sensor parameters. In this section, we will briefly review these simplifications and identify those areas where future study is required.

In Section 2, we specified that the performance model terms were limited to those associated with an acceleration environment. As mentioned in Section 3, a component of centrifuge rate will be sensed by the platform sensors based on the magnitude of the misalignment between the two spindle axes and/or variations in either the main or CRP drive system. Measurement data taken thus far on the centrifuge environment shows that an expansion of the sensor performance models is not necessary; however, since this assumption is based on the magnitude of centrifuge rate applied to the sensors and their sensitivity to rate, an evaluation of this assumption must be made for each platform

tested. Specific assumptions of the gyro and accelerometer sensors were

- (a) The gyro rotor spins at a constant speed about an axis of symmetry
- (b) The center of mass of the gyro rotor coincides with that of the gyro element.
- (c) The gyro rotor and gimbal support structure are rigid.
- (d) The gyro precession angle A_g is maintained small by the platform stabilization loop.
- (e) The accelerometer output axis angle A_O is maintained at null by the capture loop.
- (f) The gyro and accelerometer transient response can be neglected based on time constants of 2 milliseconds and 0.3 millisecond, respectively.

Assumptions (a) through (e) will be valid in most instances simply because these are closely controlled design specifications for all platform sensors used in inertial navigation applications. Assumption (f) is obviously related to the measurement cycle time of the platform. In the simulations, the assumption is valid, since the measurement cycle time is much larger than the normal criterion that the transient response is negligible after three time constants (i.e., a time period equal to three times the time constant). This is also an area that is closely controlled by design specifications with respect to the platform

operational measurement cycle time. The following assumptions were made concerning the platform performance model:

- (a) The platform gimbals are rigid.
- (b) The 2-Hz frequency of the centrifuge sinusoidal acceleration is within the system-gimbal-servo response.
- (c) The servo error is a deterministic quantity.

Assumption (a) is also related to the amount of centrifuge rate applied to the platform, since the rigidity of the gimbals is a direct function of the rate environment in which the platform was designed to operate. Assumption (b) is valid in most instances because of the design trade-off that must be made between the stabilization loop gain and bandwidth. Normal platform bandwidths range from 5 to 20 Hz, depending on the application. Assumption (c) has been found from experience to be quite valid based on servo tests and analyses conducted on numerous platforms. Therefore, it is concluded that, except for those involved with the centrifuge rate effect, the assumptions of Section 2 should be valid in most instances of platform testing on the centrifuge. In the case of the centrifuge rate effect, it is recommended that additional simulations be conducted based on actual centrifuge and platform performance data to determine what modifications are required for the sensor and platform performance models.

In Section 3, it was assumed that the inertial frame was non-rotating with respect to the fixed stars and that any deviations of the local gravity vector caused by mass anomalies were negligible. Based on a calibration time of approximately 4 hours, the inertial frame assumption is obviously valid. The mass anomaly contribution has

been verified, by measurements at the centrifuge test site, to be negligible. Specific assumptions concerning the centrifuge were

- (a) The spindle axes tilts were assumed to be constant small angles.
- (b) The dynamic change in the centrifuge radius was assumed to be constant at a stabilized g-level.
- (c) The misalignments and centrifuge rate variations were assumed to be measurable quantities; hence, the coordinate transformations were assumed to contain deterministic elements.
- (d) The platform axes were assumed defined by the physical case input axes of the sensors.

Assumptions (a) through (c) are based on preliminary data obtained from the initial evaluations of the centrifuge. It is important that additional performance data be obtained and evaluated to determine if the dynamic model and coordinate transformations defined in Section 3 are valid. It was mentioned in Section 3, that if the measurement accuracy of these centrifuge parameters is not sufficient to accurately account for the centrifuge rate effect or to determine the applied acceleration, then these parameters must be estimated by the filtering process. This assumes that the basic form of the dynamic model of the centrifuge is known, and that specific parameters in that model require to be identified or estimated. Therefore, it is extremely important to continue an evaluation of the centrifuge performance data to verify or modify the assumed models and transformations of

Section 3. Assumption (d) is quite common for platform performance models, since any error in the mounting of the sensors is included in the sensor misalignment angles. In the case of the Group 2 terms of Eq. (3.25), these also require additional evaluations at the higher centrifuge g-levels to determine if their contribution can be neglected without affecting the accuracy of the error model coefficient estimates.

In Sections 4 through 6, the following three major assumptions were made:

- (a) The statistical model assumed for the sensor parameters was a random constant in combination with a random walk.
- (b) The operating random changes of the sensor parameters were assumed to be zero mean, gaussian white, disturbance processes.
- (c) The disturbance process was assumed to be independent of the initial condition repeatability sources.

Section 4.3 of Section 4 contains an extensive discussion concerning these assumptions. Unfortunately, nothing further can be added here, except that, if additional sensor data reveals that the statistical model should incorporate correlation, then the simplification proposed by Bucy and Joseph, described at the end of Section 4.4, becomes an extremely important result. The alternative of adjusting the variance rather than augmenting the state vector would be a welcome simplification.

All the questions concerning linearization, Δv approximation, observability, and simplifying the computation of Φ and Γ were

answered by the simulation results of Sections 5 and 6. Areas requiring further study are the effect of modeling errors in the predicted filter loops; optimization of the filter performance with respect to $Q(0)$, $\bar{P}(0)$, and $R^*(1)$; and optimization of the torque profile for the 1-g calibration. The correlation patterns, provided by the off-diagonal terms of the filtering error covariance matrix, are an excellent source of information for generating an optimal torque profile. It is believed, based on the simulation results, that the correlation patterns will show that there exist "observability regions" where subsets of the model coefficient estimates are "optimal," based on the geometry of the 1-g calibration problem. Therefore, an optimal torque profile would consist of a prespecified set of commands that orient the platform axes within these regions in the minimum time. In the case of the centrifuge calibration, since the filter convergence is so rapid, it appears that an optimal torque program would consist of a prespecified set of offset Euler angles to recover the various types of model coefficients. This concludes the summary and the recommendations for further study.

REFERENCES

1. Harter, George A. "Error Analysis and Performance Optimization of Rocket Vehicle Guidance Systems," Inertial Guidance, edited by G.R. Pitman, Jr., John Wiley & Sons, New York, 1962, pp. 294-328.
2. Britting, Kenneth R. Inertial Navigation Systems Analysis, John Wiley & Sons, New York, 1971.
3. U.S. Air Force. "260-Inch Centrifuge Test Plan Information," Technical Report AFSWC-TR-71-13, 6585th Test Group, Holloman AFB, New Mexico, March 1971.
4. Sutherland, Jr., A.A. and A. Gelb. "Application of the Kalman Filter to Aided Inertial Systems," Analytic Sciences Corporation, Reading, Massachusetts, Technical Report TR-134-1 on Contract N60530-67-C-1052 (Naval Weapons Center, China Lake, California), October 1967 (Available from the Clearinghouse for Federal Scientific and Technical Information, Springfield, Virginia).
5. Crawford, B.S. "Analysis of Strapdown Sensor Testing," Analytic Sciences Corporation, Reading, Massachusetts, Technical Report TR-147-2 on Contract NAS 12-678 (NASA Electronics Research Center, Cambridge, Massachusetts), June 1970 (Available from the Clearinghouse for Federal Scientific and Technical Information, Springfield, Virginia).
6. Brock, L.D. and G.T. Schmidt. "General Questions on Kalman Filtering in Navigation Systems," Theory and Applications of Kalman Filtering, edited by C.T. Leondes, AGARDograph 139, February 1970, pp. 205-230.
7. Greenwood, Donald T. Principles of Dynamics, Prentice-Hall, Englewood Cliffs, New Jersey, 1965.
8. Wrigley, Walter, et al. Gyroscopic Theory, Design, and Instrumentation, Massachusetts Institute of Technology Press, Cambridge, Massachusetts, 1969.
9. Engebretson, H.J. "Inertial Instruments in Major System Usage," Proceedings of the Institute of Navigation/NASA Meeting on Problems in Inertial Guidance, Cambridge, Massachusetts, January 21, 1970, Institute of Navigation, Washington, D.C., January 1970, pp. 1-18.
10. Delco Electronics. "Universal Space Guidance System - Carousel VB Inertial Measurement Unit," System Technical Description EP 1028, Milwaukee, Wisconsin, December 1971.

11. Taylor, Marvin. "Fundamentals of Gyro Design," Gyroscopes - Theory and Design, edited by P.H. Savet, McGraw-Hill, New York, 1961, pp. 204-248.
12. Lorenzini, Dino A. Gyro Error Modeling, D.Sc. in Engineering, Department of Aeronautics and Astronautics, Massachusetts Institute of Technology, Cambridge, Massachusetts, February 1970, pp. 1-29.
13. Davis, Raymond E. and Francis S. Foote. Surveying - Theory and Practice, 4th ed., McGraw-Hill, New York, 1953.
14. Thede, R.R. "Centrifuge Testing of Gyros on a Counter-Rotating Platform," 6585th Test Group, Holloman AFB, New Mexico, Working Paper WP-GDA-71-3, September 1971, pp. 1-5.
15. Sage, Andrew P. Optimum Systems Control, Prentice-Hall, Englewood Cliffs, New Jersey, 1968.
16. Meditch, James S. Stochastic Optimal Linear Estimation and Control, McGraw-Hill, New York, 1969.
17. Jazwinski, Andrew H. Stochastic Processes and Filtering Theory, Academic Press, New York, 1970.
18. Papoulis, Athanasios. Probability, Random Variables, and Stochastic Processes, McGraw-Hill, New York, 1965.
19. Hsu, Jay C. and Andrew U. Meyer. Modern Control Principles and Applications, McGraw-Hill, New York, 1968.
20. Bucy, Richard S. and Peter D. Joseph. Filtering for Stochastic Processes with Applications to Guidance, Interscience Division of John Wiley & Sons, New York, 1968.

APPENDIX A

KINEMATIC ACCELERATION OF THE SENSOR FRAME

The kinematic acceleration of the sensor frame with respect to the inertial reference frame is developed using the basic equations of Coriolis and the equations for differentiating a vector \underline{R} .

The equations for differentiation of a vector \underline{R} are as follows:

$$\dot{\underline{R}} = \underline{1}_r \dot{R} + \underline{\omega}_r \times \underline{R} \quad (\text{A. 1})$$

$$\begin{aligned} \ddot{\underline{R}} = \underline{1}_r \ddot{R} + 2 (\underline{\omega}_r \times \underline{1}_r) \dot{R} + \dot{\underline{\omega}}_r \times \underline{R} \\ + \underline{\omega}_r \times (\underline{\omega}_r \times \underline{R}) \end{aligned} \quad (\text{A. 2})$$

where

\dot{R}, \ddot{R} - are the scalar velocity and scalar acceleration of \underline{R}

$\underline{\omega}_r$ = angular velocity of the vector \underline{R} and $\underline{1}_r$

$\underline{1}_r$ = unit vector in the direction of \underline{R}

The first term of Eq. (A.1) is the rate of change of the length of vector \underline{R} , and the second term (whose direction is perpendicular to \underline{R}) gives the rate of change of \underline{R} due to the rotation $\underline{\omega}_r$. The first term of Eq. (A.2) is the second rate of change of the length of vector \underline{R} (i.e., linear acceleration along \underline{R}); the second and third terms are both tangential accelerations; and the last term is the centripetal

acceleration resulting from the rotation of \underline{R} and is directed toward the center of rotation.

The equations of Coriolis for rotating bodies are as follows [7]:

$$\dot{\underline{R}}_{ij}^k = \dot{\underline{R}}_{ij}^i + \underline{\omega}_{ki} \times \underline{R}_{ij} \quad (\text{A. 3})$$

$$\begin{aligned} \ddot{\underline{R}}_{ij}^k = & \ddot{\underline{R}}_{ij}^i + \dot{\underline{\omega}}_{ki}^k \times \underline{R}_{ij} + 2\underline{\omega}_{ki} \times \dot{\underline{R}}_{ij}^i \\ & + \underline{\omega}_{ki} \times (\underline{\omega}_{ki} \times \underline{R}_{ij}) \end{aligned} \quad (\text{A. 4})$$

Equation (A. 3) shows that the rate of change of a vector \underline{R}_{ij} , as viewed from a reference frame k , is equal to the rate of change of the vector \underline{R}_{ij} , as seen from a moving frame i , plus the angular velocity of the moving frame, with respect to the reference frame $\underline{\omega}_{ki}$, crossed with the original vector. Equation (A. 4) gives the kinematic acceleration of frame j with respect to frame i , as viewed from reference frame k . The first term of Eq. (A. 4) is generally referred to as the "linear" acceleration term, as seen from the moving frame i , even though it may contain the tangential and centripetal components defined in Eq. (A. 2). The second term of Eq. (A. 4) is the tangential acceleration due to the angular acceleration of the moving frame, with respect to the reference frame; the third term is the Coriolis acceleration, which is generated by a change in the direction of $\dot{\underline{R}}_{ij}^i$, relative to the moving frame i , plus a portion of the rate of change of the velocity $\underline{\omega}_{ki} \times \underline{R}_{ij}$, due to a change in magnitude or direction of the position vector \underline{R}_{ij} . The fourth term is the centripetal acceleration resulting

from the rotation of the moving frame with respect to the reference frame.

The basic coordinate frames connecting the inertial frame to the sensor frame are shown in the vector map of Figure A.1. All the coordinate frames from inertial space to the sensor axes are defined in Section 3. The basic coordinate frames are the major transformations linking inertial space to the sensor axes. The intermediate transformations that are excluded from the basic frames are essentially those frames that account for misalignments of the physical members of the centrifuge, such as the main spindle, the counter-rotating platform spindle, and the Inertial Navigation System mounting fixture.

The position of the basic coordinate frames is described in the following vector equations (Reference Figure A.1).

$$\underline{R}_{rs} = \underline{R}_{rp} + \underline{R}_{ps} \quad (\text{A. 5})$$

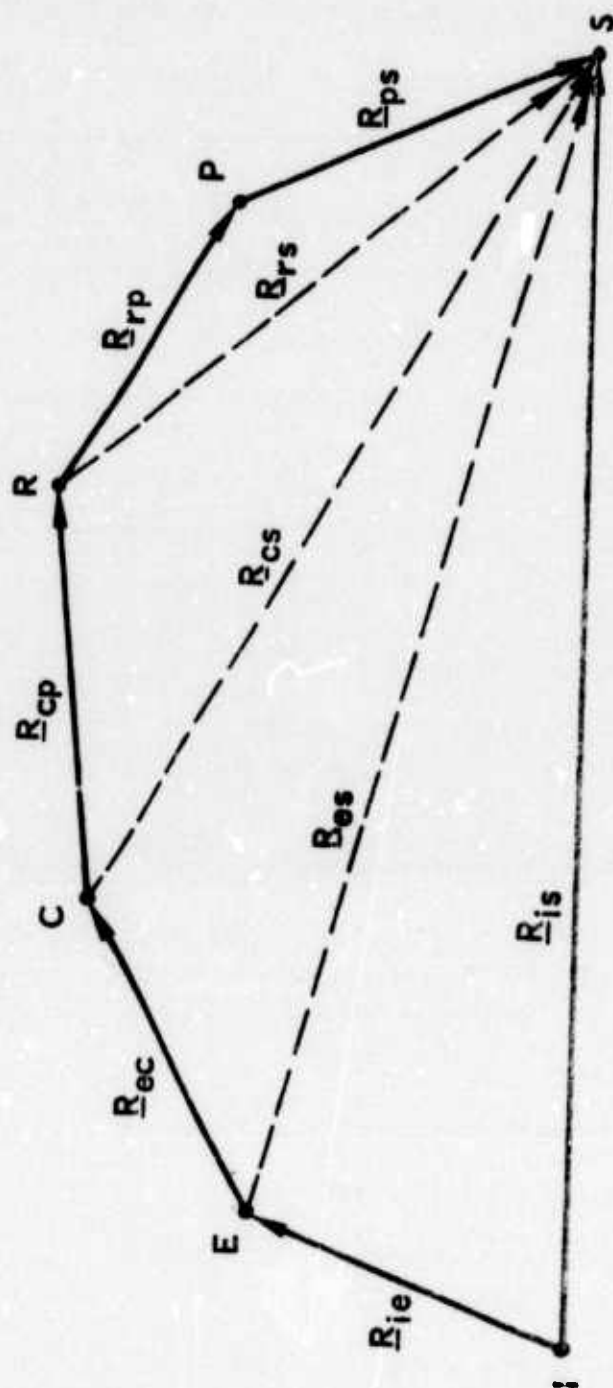
$$\underline{R}_{cs} = \underline{R}_{cr} + \underline{R}_{rs} \quad (\text{A. 6})$$

$$\underline{R}_{es} = \underline{R}_{ec} + \underline{R}_{cs} \quad (\text{A. 7})$$

$$\underline{R}_{is} = \underline{R}_{ie} + \underline{R}_{es} \quad (\text{A. 8})$$

The first and second derivatives of Eq. (A.5) are:

$$\dot{\underline{R}}_{rs}^r = \dot{\underline{R}}_{rp}^r + \dot{\underline{R}}_{ps}^r \quad (\text{A. 9})$$



LEGEND:

I - INERTIAL FRAME

E - EARTH FRAME

C - CENTRIFUGE MAIN ARM FRAME

R - CENTRIFUGE COUNTER-ROTATING PLATFORM FRAME

P - SYSTEM INNER GIMBAL PLATFORM FRAME

S - SENSOR FRAME

Figure A. 1. Vector Map of Basic Coordinate Frames

$$\ddot{\underline{R}}_{rs}^r = \ddot{\underline{R}}_{rp}^r + \ddot{\underline{R}}_{ps}^r \quad (\text{A.10})$$

Applying the Coriolis Eqs. (A.3) and (A.4) to $\dot{\underline{R}}_{ps}^r$ and $\ddot{\underline{R}}_{ps}^r$, respectively, gives:

$$\dot{\underline{R}}_{ps}^r = \dot{\underline{R}}_{ps}^p + \underline{\omega}_{rp} \times \underline{R}_{ps} \quad (\text{A.11})$$

$$\begin{aligned} \ddot{\underline{R}}_{ps}^r &= \ddot{\underline{R}}_{ps}^p + \dot{\underline{\omega}}_{rp}^r \times \underline{R}_{ps} + 2\underline{\omega}_{rp} \times \dot{\underline{R}}_{ps}^p \\ &\quad + \underline{\omega}_{rp} \times (\underline{\omega}_{rp} \times \underline{R}_{ps}) \end{aligned} \quad (\text{A.12})$$

From Eqs. (A.11) and (A.12), Eqs. (A.9) and (A.10) become:

$$\dot{\underline{R}}_{rs}^r = \dot{\underline{R}}_{rp}^r + \dot{\underline{R}}_{ps}^p + \underline{\omega}_{rp} \times \underline{R}_{ps} \quad (\text{A.13})$$

$$\begin{aligned} \ddot{\underline{R}}_{rs}^r &= \ddot{\underline{R}}_{rp}^r + \ddot{\underline{R}}_{ps}^p + \dot{\underline{\omega}}_{rp}^r \times \underline{R}_{ps} + 2\underline{\omega}_{rp} \\ &\quad \times \dot{\underline{R}}_{ps}^p + \underline{\omega}_{rp} \times (\underline{\omega}_{rp} \times \underline{R}_{ps}) \end{aligned} \quad (\text{A.14})$$

The first and second derivatives of Eq. (A.6) are:

$$\dot{\underline{R}}_{cs}^c = \dot{\underline{R}}_{cr}^c + \dot{\underline{R}}_{rs}^c \quad (\text{A.15})$$

$$\ddot{\underline{R}}_{cs}^c = \ddot{\underline{R}}_{cr}^c + \ddot{\underline{R}}_{rs}^c \quad (\text{A.16})$$

Applying the Coriolis equations to $\dot{\underline{R}}_{rs}^c$ and $\ddot{\underline{R}}_{rs}^c$ yields:

$$\dot{\underline{R}}_{cs}^c = \dot{\underline{R}}_{cr}^c + \dot{\underline{R}}_{rs}^r + \underline{\omega}_{cr} \times \underline{R}_{rs} \quad (\text{A.17})$$

$$\begin{aligned} \ddot{\underline{R}}_{cs}^c = & \ddot{\underline{R}}_{cr}^c + \ddot{\underline{R}}_{rs}^r + \dot{\underline{\omega}}_{cr}^c \times \underline{R}_{rs} + 2\underline{\omega}_{cr} \\ & \times \dot{\underline{R}}_{rs}^r + \underline{\omega}_{cr} \times (\underline{\omega}_{cr} \times \underline{R}_{rs}) \end{aligned} \quad (\text{A.18})$$

Substituting Eqs. (A.13) and (A.14) into Eqs. (A.17) and (A.18) yields:

$$\dot{\underline{R}}_{cs}^c = \dot{\underline{R}}_{cr}^c + \dot{\underline{R}}_{rp}^r + \dot{\underline{R}}_{ps}^p + \underline{\omega}_{cr} \times \underline{R}_{rs} + \underline{\omega}_{rp} \times \underline{R}_{ps} \quad (\text{A.19})$$

$$\begin{aligned} \ddot{\underline{R}}_{cs}^c = & \ddot{\underline{R}}_{cr}^c + \ddot{\underline{R}}_{rp}^r + \ddot{\underline{R}}_{ps}^p + \dot{\underline{\omega}}_{rp}^r \times \underline{R}_{ps} \\ & + \dot{\underline{\omega}}_{cr}^c \times \underline{R}_{rs} + 2\underline{\omega}_{rp} \times \dot{\underline{R}}_{ps}^p \\ & + 2\underline{\omega}_{cr} \times \left(\dot{\underline{R}}_{rp}^r + \dot{\underline{R}}_{ps}^p + \underline{\omega}_{rp} \times \underline{R}_{ps} \right) \\ & + \underline{\omega}_{rp} \times (\underline{\omega}_{rp} \times \underline{R}_{ps}) + \underline{\omega}_{cr} \times (\underline{\omega}_{cr} \times \underline{R}_{rs}) \end{aligned} \quad (\text{A.20})$$

The derivatives of Eq. (A.7) are:

$$\dot{\underline{R}}_{es}^e = \dot{\underline{R}}_{ec}^e + \dot{\underline{R}}_{cs}^e \quad (\text{A.21})$$

$$\ddot{\underline{R}}_{es}^e = \ddot{\underline{R}}_{ec}^e + \ddot{\underline{R}}_{cs}^e \quad (\text{A.22})$$

Applying the Coriolis equations to $\dot{\underline{R}}_{cs}^e$ and $\ddot{\underline{R}}_{cs}^e$ yields:

$$\dot{\underline{R}}_{es}^e = \dot{\underline{R}}_{ec}^e + \dot{\underline{R}}_{cs}^c + \underline{\omega}_{ec} \times \underline{R}_{cs} \quad (\text{A.23})$$

$$\begin{aligned} \ddot{\underline{R}}_{es}^e = & \ddot{\underline{R}}_{ec}^e + \ddot{\underline{R}}_{cs}^c + \dot{\underline{\omega}}_{ec} \times \underline{R}_{cs} + 2 \underline{\omega}_{ec} \times \dot{\underline{R}}_{cs}^c \\ & + \underline{\omega}_{ec} \times (\underline{\omega}_{ec} \times \underline{R}_{cs}) \end{aligned} \quad (\text{A.24})$$

Substituting Eqs. (A.19) and (A.20) into Eqs. (A.23) and (A.24) gives:

$$\begin{aligned} \dot{\underline{R}}_{es}^e = & \dot{\underline{R}}_{ec}^e + \dot{\underline{R}}_{cr}^c + \dot{\underline{R}}_{rp}^r + \dot{\underline{R}}_{ps}^p + \underline{\omega}_{ec} \times \underline{R}_{cs} \\ & + \underline{\omega}_{cr} \times \underline{R}_{rs} + \underline{\omega}_{rp} \times \underline{R}_{ps} \end{aligned} \quad (\text{A.25})$$

$$\begin{aligned} \ddot{\underline{R}}_{es}^e = & \ddot{\underline{R}}_{ec}^e + \ddot{\underline{R}}_{cr}^c + \ddot{\underline{R}}_{rp}^r + \ddot{\underline{R}}_{ps}^p \\ & + \dot{\underline{\omega}}_{ec} \times \underline{R}_{cs} + \dot{\underline{\omega}}_{cr} \times \underline{R}_{rs} + \dot{\underline{\omega}}_{rp} \times \underline{R}_{ps} \\ & + 2 \underline{\omega}_{ec} \times \left(\dot{\underline{R}}_{cr}^c + \dot{\underline{R}}_{rp}^r + \dot{\underline{R}}_{ps}^p + \underline{\omega}_{cr} \times \underline{R}_{rs} + \underline{\omega}_{rp} \times \underline{R}_{ps} \right) \\ & + 2 \underline{\omega}_{cr} \times \left(\dot{\underline{R}}_{rp}^r + \dot{\underline{R}}_{ps}^p + \underline{\omega}_{rp} \times \underline{R}_{ps} \right) + 2 \underline{\omega}_{rp} \times \dot{\underline{R}}_{ps}^p \\ & + \underline{\omega}_{ec} \times (\underline{\omega}_{ec} \times \underline{R}_{cs}) + \underline{\omega}_{cr} \times (\underline{\omega}_{cr} \times \underline{R}_{rs}) + \underline{\omega}_{rp} \times (\underline{\omega}_{rp} \times \underline{R}_{ps}) \end{aligned} \quad (\text{A.26})$$

The derivatives of Eq. (A.8) are:

$$\dot{\underline{R}}_{is}^i = \dot{\underline{R}}_{ie}^i + \dot{\underline{R}}_{es}^i \quad (\text{A.27})$$

$$\ddot{\underline{R}}_{is}^i = \ddot{\underline{R}}_{ie}^i + \ddot{\underline{R}}_{es}^i \quad (\text{A. 28})$$

Applying the Coriolis equations to $\dot{\underline{R}}_{es}^i$ and $\ddot{\underline{R}}_{es}^i$ yields:

$$\dot{\underline{R}}_{is}^i = \dot{\underline{R}}_{ie}^i + \dot{\underline{R}}_{es}^e + \underline{\omega}_{ie} \times \underline{R}_{es} \quad (\text{A. 29})$$

$$\begin{aligned} \ddot{\underline{R}}_{is}^i = & \ddot{\underline{R}}_{ie}^i + \ddot{\underline{R}}_{es}^e + \dot{\underline{\omega}}_{ie}^i \times \underline{R}_{es} + 2 \underline{\omega}_{ie} \times \dot{\underline{R}}_{es}^e \\ & + \underline{\omega}_{ie} \times (\underline{\omega}_{ie} \times \underline{R}_{es}) \end{aligned} \quad (\text{A. 30})$$

Substituting Eqs. (A. 25) and (A. 26) into Eq. (A. 30) gives an expression for the kinematic acceleration of the sensor frame, with respect to the inertial frame, as viewed from the inertial frame.

$$\begin{aligned} \ddot{\underline{R}}_{is}^i = & \ddot{\underline{R}}_{ie}^i + \ddot{\underline{R}}_{ec}^e + \ddot{\underline{R}}_{cr}^c + \ddot{\underline{R}}_{rp}^r + \ddot{\underline{R}}_{ps}^p \quad \textcircled{1} \\ & + \dot{\underline{\omega}}_{ie}^i \times \underline{R}_{es} + \dot{\underline{\omega}}_{ec}^e \times \underline{R}_{cs} + \dot{\underline{\omega}}_{cr}^c \times \underline{R}_{rs} + \dot{\underline{\omega}}_{rp}^r \times \underline{R}_{ps} \quad \textcircled{2} \\ & + 2 \underline{\omega}_{ie} \times \left(\dot{\underline{R}}_{ec}^e + \dot{\underline{R}}_{cr}^c + \dot{\underline{R}}_{rp}^r + \dot{\underline{R}}_{ps}^p + \underline{\omega}_{ec} \times \underline{R}_{cs} \right. \\ & \quad \left. + \underline{\omega}_{cr} \times \underline{R}_{rs} + \underline{\omega}_{rp} \times \underline{R}_{ps} \right) \\ & + 2 \underline{\omega}_{ec} \times \left(\dot{\underline{R}}_{cr}^c + \dot{\underline{R}}_{rp}^r + \dot{\underline{R}}_{ps}^p + \underline{\omega}_{cr} \times \underline{R}_{rs} + \underline{\omega}_{rp} \times \underline{R}_{ps} \right) \quad \textcircled{3} \\ & + 2 \underline{\omega}_{cr} \times \left(\dot{\underline{R}}_{rp}^r + \dot{\underline{R}}_{ps}^p + \underline{\omega}_{rp} \times \underline{R}_{ps} \right) + 2 \underline{\omega}_{rp} \times \dot{\underline{R}}_{ps}^p \end{aligned}$$

$$\begin{aligned}
 &+ \underline{\omega}_{ie} \times (\underline{\omega}_{ie} \times \underline{R}_{es}) + \underline{\omega}_{ec} \times (\underline{\omega}_{ec} \times \underline{R}_{cs}) \\
 &+ \underline{\omega}_{cr} \times (\underline{\omega}_{cr} \times \underline{R}_{rs}) + \underline{\omega}_{rp} \times (\underline{\omega}_{rp} \times \underline{R}_{ps})
 \end{aligned}$$

(A. 31)

- ① indicates linear acceleration terms
- ② indicates tangential acceleration terms
- ③ indicates Coriolis acceleration terms
- ④ indicates centripetal acceleration terms

where

$$\underline{R}_{es} = \underline{R}_{ec} + \underline{R}_{cr} + \underline{R}_{rp} + \underline{R}_{ps}$$

$$\underline{R}_{cs} = \underline{R}_{cr} + \underline{R}_{rp} + \underline{R}_{ps}$$

$$\underline{R}_{rs} = \underline{R}_{rp} + \underline{R}_{ps}$$

APPENDIX B

CALCULATION OF APPLIED ACCELERATION GROUP 2 TERMS

The Group 2 terms of the applied acceleration equation are determined for both simulations. The Group 2 terms discussed in Section 3.3 of Section 3, and defined in Eq. (3.25), are undesirable, since they consist of platform rate, platform acceleration, and higher-order products and cross-products of the platform rate. The calculations will show that the Group 2 terms can be neglected for both the 1-g and operating centrifuge simulations.

B.1 CALCULATIONS FOR THE 1-g SIMULATION

Since the maximum contribution will occur when the coordinate transformations are all identity matrices I , we assume

$$C_r^p = C_c^r = C_e^c = C_c^e = C_r^c = C_p^r \equiv I \quad (B.1)$$

For the 1-g simulation, $\Delta W_{cr}^{rk} \equiv 0$, so the Group 2 terms reduce to

$$C_p^s \left[2W_{ie}^{ek} W_{rp}^{pk} R_{ps}^p + \dot{W}_{rp}^{pk} R_{ps}^p + W_{rp}^{pk} W_{rp}^{pk} R_{ps}^p \right] \quad (B.2)$$

as can be seen from Eq. (3.25).

The first calculation is to determine the contribution that the Group 2 terms make toward the platform rates defined by Eq. (2.33). We determine $\delta\omega_{xp}$, $\delta\omega_{yp}$, and $\delta\omega_{zp}$ based on the variables defined in Section 5 for the 1-g simulation. We first need the acceleration

Preceding page blank

applied to each gyro by the Group 2 terms. Hence, we first select the appropriate values of C_p^s and R_{ps}^p from Eqs. (3.20) and (3.18) respectively. An expansion of the first Group 2 term of Eq. (B.2) is

$$\begin{bmatrix} 0 & -2WES & 2WEC \\ 2WES & 0 & 0 \\ -2WEC & 0 & 0 \end{bmatrix} \begin{bmatrix} 0 & -\omega_{zp} & \omega_{yp} \\ \omega_{zp} & 0 & -\omega_{xp} \\ -\omega_{yp} & \omega_{xp} & 0 \end{bmatrix} R_{ps}^p \quad (B.3)$$

The second term is

$$\begin{bmatrix} 0 & -\dot{\omega}_{zp} & \dot{\omega}_{yp} \\ \dot{\omega}_{zp} & 0 & -\dot{\omega}_{xp} \\ -\dot{\omega}_{yp} & \dot{\omega}_{xp} & 0 \end{bmatrix} R_{ps}^p \quad (B.4)$$

and finally the last term is

$$\begin{bmatrix} 0 & -\omega_{zp} & \omega_{yp} \\ \omega_{zp} & 0 & -\omega_{xp} \\ -\omega_{yp} & \omega_{xp} & 0 \end{bmatrix} \begin{bmatrix} 0 & -\omega_{zp} & \omega_{yp} \\ \omega_{zp} & 0 & -\omega_{xp} \\ -\omega_{yp} & \omega_{xp} & 0 \end{bmatrix} R_{ps}^p \quad (B.5)$$

A list of the parameters used in the calculation is

$$WEC = 6.12 \times 10^{-5} \text{ rad/sec}$$

$$WES = 3.96 \times 10^{-5} \text{ rad/sec}$$

$$g = 32.124 \text{ ft/sec}^2$$

$$\eta_{x_0} = 1.26 \times 10^{-3} \text{ rad}$$

$$\psi_{x_i} = 1.48 \times 10^{-3} \text{ rad}$$

$$D_{IX} = 5.25 \times 10^{-6} \text{ rad/sec/g}$$

$$D_{IY} = 4.96 \times 10^{-6} \text{ rad/sec/g}$$

$$D_{IZ} = 4.52 \times 10^{-6} \text{ rad/sec/g}$$

$$K_{1X} = K_{1Y} = K_{1Z} = 1.0 \text{ g/g}$$

The platform rate and platform acceleration values taken from the computer simulation results are

$$\omega_{xp} = -4.71 \times 10^{-4} \text{ rad/sec}$$

$$\omega_{yp} = -4.05 \times 10^{-4} \text{ rad/sec}$$

$$\omega_{zp} = 4.60 \times 10^{-4} \text{ rad/sec}$$

$$\dot{\omega}_{xp} = 4.47 \times 10^{-8} \text{ rad/sec}^2$$

$$\dot{\omega}_{yp} = -1.69 \times 10^{-8} \text{ rad/sec}^2$$

$$\dot{\omega}_{zp} = 3.06 \times 10^{-8} \text{ rad/sec}^2$$

where

$$\dot{\omega}_{ip} \cong \frac{\omega_{ip}(t_n) - \omega_{ip}(t_{n-1})}{\Delta t} \quad [i = x, y, z]$$

$$\Delta t = t_n - t_{n-1} = 1.0 \text{ second}$$

When the above parameters are substituted in the expanded terms we obtain the following values for the acceleration applied to the three gyros.

$$\begin{aligned}
\delta A_{is}^{SGX} &= \begin{bmatrix} \delta a_{IX} \\ \delta a_{OX} \\ \delta a_{SX} \end{bmatrix} = \begin{bmatrix} 0.468 \times 10^{-9} \text{ g's} \\ -1.228 \times 10^{-9} \text{ g's} \\ 1.939 \times 10^{-9} \text{ g's} \end{bmatrix} \\
\delta A_{is}^{SGY} &= \begin{bmatrix} \delta a_{IY} \\ \delta a_{OY} \\ \delta a_{SY} \end{bmatrix} = \begin{bmatrix} 0.791 \times 10^{-9} \text{ g's} \\ -2.263 \times 10^{-9} \text{ g's} \\ -2.345 \times 10^{-9} \text{ g's} \end{bmatrix} \\
\delta A_{is}^{SGZ} &= \begin{bmatrix} \delta a_{IZ} \\ \delta a_{OZ} \\ \delta a_{SZ} \end{bmatrix} = \begin{bmatrix} -0.866 \times 10^{-9} \text{ g's} \\ -1.586 \times 10^{-9} \text{ g's} \\ 1.415 \times 10^{-9} \text{ g's} \end{bmatrix}
\end{aligned} \tag{B.6}$$

From Eq. (2.33), the delta platform rate equations are

$$\begin{aligned}
\delta \omega_{xp} &= -D_{IX} \delta a_{IX} \\
\delta \omega_{yp} &= -D_{IY} \delta a_{IY} \\
\delta \omega_{zp} &= \eta_{x_o} D_{IX} \delta a_{IX} - D_{IZ} \delta a_{IZ}
\end{aligned} \tag{B.7}$$

Substituting the values from Eq. (B.6) into (B.7) gives

$$\begin{aligned}
\delta \omega_{xp} &= -2.457 \times 10^{-15} \text{ rad/sec} \\
\delta \omega_{yp} &= -3.923 \times 10^{-15} \text{ rad/sec} \\
\delta \omega_{zp} &= 3.917 \times 10^{-15} \text{ rad/sec}
\end{aligned} \tag{B.8}$$

Comparing these values with those obtained from the computer simulation, we see that the contribution of the Group 2 terms is 11 orders of magnitude below the 1-g simulation rates. The Group 2 term rate contribution can obviously be neglected.

The same procedure is used to obtain the platform acceleration contribution of the Group 2 terms. The only difference is that C_p^s is obtained from Eq. (3.19) for the accelerometers. The acceleration applied to the three accelerometers is

$$\begin{aligned} \delta A_{is}^{SAX} &= \begin{bmatrix} \delta a_{IAX} \\ \delta a_{PX} \\ \delta a_{OAX} \end{bmatrix} = \begin{bmatrix} 1.136 \times 10^{-9} \text{ g's} \\ -1.966 \times 10^{-9} \text{ g's} \\ 2.398 \times 10^{-9} \text{ g's} \end{bmatrix} \\ \delta A_{is}^{SAY} &= \begin{bmatrix} \delta a_{IAY} \\ \delta a_{PY} \\ \delta a_{OAY} \end{bmatrix} = \begin{bmatrix} 0.204 \times 10^{-9} \text{ g's} \\ -1.291 \times 10^{-9} \text{ g's} \\ -1.839 \times 10^{-9} \text{ g's} \end{bmatrix} \\ \delta A_{is}^{SAZ} &= \begin{bmatrix} \delta a_{IAZ} \\ \delta a_{PZ} \\ \delta a_{OAZ} \end{bmatrix} = \begin{bmatrix} -1.640 \times 10^{-9} \text{ g's} \\ -2.853 \times 10^{-9} \text{ g's} \\ 0.655 \times 10^{-9} \text{ g's} \end{bmatrix} \end{aligned} \quad (B.9)$$

From Eq. (2.34), the delta platform acceleration equations are

$$\begin{aligned}\delta A_X &= K_{1X} \delta a_{1AX} \\ \delta A_Y &= K_{1Y} \delta a_{1AY} \\ \delta A_Z &= K_{1Z} \delta a_{1AZ}\end{aligned}\tag{B.10}$$

Substituting the values of Eq. (B.9) into (B.10) gives

$$\begin{aligned}\delta A_X &= 1.136 \times 10^{-9} \text{ g's} \\ \delta A_Y &= 0.204 \times 10^{-9} \text{ g's} \\ \delta A_Z &= -1.640 \times 10^{-9} \text{ g's}\end{aligned}\tag{B.11}$$

These values are 4 orders of magnitude below the measurement noise level of 13.0×10^{-6} g's. The Group 2 terms can therefore be completely neglected for the 1-g simulation.

B.2 CALCULATIONS FOR THE CENTRIFUGE SIMULATION

The calculations for the centrifuge simulation are quite similar to the 1-g case. The assumption of Eq. (B.1) still holds. Using the platform rates from the centrifuge computer results and a value of $\delta\omega = 3 \times 10^{-6}$ rad/sec (Reference Section 3.1 of Section 3), the maximum contribution of the $\Delta W_{cr}^{rk} W_{rp}^{pk} R_{ps}^p$ term of Eq. (3.25) is 0.009×10^{-9} g's. Hence, Eq. (B.2) can represent the Group 2 term equation for the centrifuge simulation.

A list of the additional parameters required for the centrifuge calculation is

$$D_{OZ} = 4.52 \times 10^{-6} \text{ rad/sec/g}$$

$$D_{OOY} = 0.29 \times 10^{-6} \text{ rad/sec/g}^2$$

$$D_{ISZ} = 0.22 \times 10^{-6} \text{ rad/sec/g}^2$$

$$K_{2Y} = 12 \times 10^{-6} \text{ g/g}^2$$

$$K_{3Z} = 3 \times 10^{-6} \text{ g/g}^3$$

$$K_{IPX} = 5 \times 10^{-6} \text{ g/g}^2$$

$$AX = 0$$

$$AY = -10.00020568 \text{ g's}$$

$$AZ = 1.00031805 \text{ g's}$$

$$\omega_c t = 90^\circ$$

The value of $\omega_c t$ was based on an analysis of the delta equations to give the worst case condition. The platform rate and platform acceleration values taken from the computer simulation results are

$$\omega_{xp} = -5.24 \times 10^{-4} \text{ rad/sec}$$

$$\omega_{yp} = -5.58 \times 10^{-4} \text{ rad/sec}$$

$$\omega_{zp} = -0.94 \times 10^{-4} \text{ rad/sec}$$

$$\dot{\omega}_{xp} = -4.43 \times 10^{-6} \text{ rad/sec}^2$$

$$\dot{\omega}_{yp} = -3.17 \times 10^{-5} \text{ rad/sec}^2$$

$$\dot{\omega}_{zp} = -3.29 \times 10^{-6} \text{ rad/sec}^2$$

Note that the platform acceleration values are 2 to 3 orders of magnitude larger than those of the 1-g case. Because of this, the major contribution is from Eq. (B.4).

When the above parameters are substituted in the expanded terms, we obtain the following values for the acceleration applied to the three gyros:

$$\begin{aligned} \delta A_{is}^{SGX} &= \begin{bmatrix} \delta a_{IX} \\ \delta a_{OX} \\ \delta a_{SX} \end{bmatrix} = \begin{bmatrix} 0.163 \times 10^{-6} \text{ g's} \\ -0.085 \times 10^{-6} \text{ g's} \\ -0.031 \times 10^{-6} \text{ g's} \end{bmatrix} \\ \delta A_{is}^{SGY} &= \begin{bmatrix} \delta a_{IY} \\ \delta a_{OY} \\ \delta a_{SY} \end{bmatrix} = \begin{bmatrix} -0.015 \times 10^{-6} \text{ g's} \\ 0.079 \times 10^{-6} \text{ g's} \\ -0.165 \times 10^{-6} \text{ g's} \end{bmatrix} \\ \delta A_{is}^{SGZ} &= \begin{bmatrix} \delta a_{IZ} \\ \delta a_{OZ} \\ \delta a_{SZ} \end{bmatrix} = \begin{bmatrix} 0.021 \times 10^{-6} \text{ g's} \\ -0.141 \times 10^{-6} \text{ g's} \\ 0.018 \times 10^{-6} \text{ g's} \end{bmatrix} \end{aligned} \quad (B.12)$$

The following delta approximations, which neglect second-order δa terms, were used in the development of the delta equations that are given next.

$$\Delta(a + \delta a)^2 \cong 2a \delta a$$

$$\Delta(a + \delta a)^3 \cong 3a^2 \delta a \quad (\text{B. 13})$$

$$\Delta(a + \delta a)(b + \delta b) \cong a \delta b + b \delta a$$

From Eq. (2.33), the delta platform rate equations are

$$\delta \omega_{xp} = -D_{IX} \delta a_{IX}$$

$$\delta \omega_{yp} = -D_{IY} \delta a_{IY} + 2D_{OY} (AZ) \delta a_{OY} \quad (\text{B. 14})$$

$$\delta \omega_{zp} = -D_{OZ} \delta a_{OZ} - D_{ISZ} [(AY) \delta a_{IZ} + (AZ) \delta a_{SZ}]$$

From the values of Eq. (B.12), the results of Eq. (B.14) are

$$\delta \omega_{xp} = -8.558 \times 10^{-13} \text{ rad/sec}$$

$$\delta \omega_{yp} = 1.202 \times 10^{-13} \text{ rad/sec} \quad (\text{B. 15})$$

$$\delta \omega_{zp} = 6.795 \times 10^{-13} \text{ rad/sec}$$

Comparing these values with those obtained from the centrifuge simulation shows that the contribution of the Group 2 terms is 9 orders of magnitude below the centrifuge simulation rates.

The acceleration applied to the three accelerometers is

$$\begin{aligned}
\delta A_{is}^{SAX} &= \begin{bmatrix} \delta a_{IAX} \\ \delta a_{PX} \\ \delta a_{OAX} \end{bmatrix} = \begin{bmatrix} 0.155 \times 10^{-6} \text{ g's} \\ -0.014 \times 10^{-6} \text{ g's} \\ -0.022 \times 10^{-6} \text{ g's} \end{bmatrix} \\
\delta A_{is}^{SAY} &= \begin{bmatrix} \delta a_{IAY} \\ \delta a_{PY} \\ \delta a_{OAY} \end{bmatrix} = \begin{bmatrix} -0.024 \times 10^{-6} \text{ g's} \\ 0.007 \times 10^{-6} \text{ g's} \\ -0.174 \times 10^{-6} \text{ g's} \end{bmatrix} \\
\delta A_{is}^{SAZ} &= \begin{bmatrix} \delta a_{IAZ} \\ \delta a_{PZ} \\ \delta a_{OAZ} \end{bmatrix} = \begin{bmatrix} -0.019 \times 10^{-6} \text{ g's} \\ 0.016 \times 10^{-6} \text{ g's} \\ 0.110 \times 10^{-6} \text{ g's} \end{bmatrix}
\end{aligned} \tag{B.16}$$

When the approximations of Eq. (B.13) are used, the delta platform acceleration equations, from Eq. (2.34), are

$$\begin{aligned}
\delta A_X &= K_{1X} \delta a_{IAX} + K_{IPX} \{ [(AX) \delta a_{PX}] - [(AZ) \delta a_{IAX}] \} \\
\delta A_Y &= K_{1Y} \delta a_{IAY} + 2K_{2Y} (AY) \delta a_{IAY} \\
\delta A_Z &= K_{1Z} \delta a_{IAZ} + 3K_{3Z} (AZ)^2 \delta a_{IAZ}
\end{aligned} \tag{B.17}$$

Substituting the values of Eq. (B.16) into (B.17) gives

$$\delta A_X = 0.155 \times 10^{-6} \text{ g's}$$

$$\delta A_Y = -0.024 \times 10^{-6} \text{ g's} \quad (\text{B. 18})$$

$$\delta A_Z = -0.019 \times 10^{-6} \text{ g's}$$

In the 1-g simulation, the time between measurements Δt is 1 second; therefore, a direct comparison between the δA values and the $13 \times 10^{-6} \text{ g's}$, 1 sigma, of measurement noise is valid. In the centrifuge simulation, $\Delta t = 0.04 \text{ second}$ and $13 \times 10^{-6} \text{ g-sec}$, 1 sigma, of velocity noise is added each Δt cycle. Hence, a more valid comparison would be in the velocity domain. Changing Eq. (B. 18) to δv velocity values over the measurement interval gives

$$\delta v_X = 6.20 \times 10^{-9} \text{ g-sec}$$

$$\delta v_Y = -0.96 \times 10^{-9} \text{ g-sec} \quad (\text{B. 19})$$

$$\delta v_Z = -0.76 \times 10^{-9} \text{ g-sec}$$

These values are 3 to 4 orders of magnitude below the velocity measurement noise level of $13 \times 10^{-6} \text{ g-sec}$, 1 sigma.

The calculations show that the Group 2 terms can be completely neglected for the centrifuge simulation.

APPENDIX C

ANALYTIC PARTIALS

The analytic partials of the state and measurement functions for both simulations are contained in this appendix.

C.1 ANALYTIC PARTIALS FOR THE 1-g SIMULATION

The partials of the state function are defined by the following (17×17) matrix of partial derivatives.

$$F[\hat{\mathbf{x}}(t_{n-1}|t_{n-1})] \triangleq \left[\frac{\partial f_i[\hat{\mathbf{x}}(t_{n-1}|t_{n-1})]}{\partial \mathbf{x}_j} \right] \quad (C.1)$$

$$i, j = 1, 2, \dots, 17$$

where

f_i - are the elements of $\underline{f}(\underline{x})$ defined in Section 5

$\hat{\mathbf{x}}(t_{n-1}|t_{n-1})$ - are the filtered state estimates

The first 14 rows of $\underline{f}(\underline{x})$ are zero, implying that the first 14 rows of F contain zero elements.

$$F_{ij} = 0 \text{ for } \begin{matrix} i = 1 \text{ thru } 14 \\ j = 1 \text{ thru } 17 \end{matrix} \quad (C.2)$$

Therefore, only the last three rows of F need to be evaluated. The following is a list of the nonzero elements of F in the last three rows. All elements not listed are zero.

Define

$$\hat{x}_i = \hat{x}_i(t_{n-1} | t_{n-1}) \quad i = 1, 2, \dots, 17$$

$\hat{E}_{ij}(i, j = 1, 2, 3)$ - are the elements of the Euler transformation matrix E in Section 5, evaluated at \hat{x}_i

$\hat{\omega}_{xp}, \hat{\omega}_{zp}$ - are the platform rate equations defined in Section 5, evaluated at \hat{x}_i

$$C15 = \cos(\hat{x}_{15})$$

$$C16 = \cos(\hat{x}_{16})$$

$$C17 = \cos(\hat{x}_{17})$$

$$S15 = \sin(\hat{x}_{15})$$

$$S16 = \sin(\hat{x}_{16})$$

$$S17 = \sin(\hat{x}_{17})$$

$$C217 = \cos(2 \hat{x}_{17})$$

The nonzero elements of F are

$$F_{15,1} = (\hat{x}_{13} S17 - C17)/C16$$

$$F_{15,3} = - S17/C16$$

$$F_{15,4} = (2 \hat{x}_{13} C17 S17 S16 S15 + \hat{x}_{13} C15 C217 - C17 \hat{E}_{13})/C16$$

$$F_{15,6} = - S17 \hat{E}_{33}/C16$$

$$F_{15,13} = (2 \hat{x}_4 C17 S17 S16 S15 + \hat{x}_4 C15 C217 \\ + \hat{x}_1 S17 + S17 TGX)/C16$$

$$F_{15,15} = [\hat{x}_4 \hat{x}_{13} (2 C17 S17 S16 C15 - S15 C217) \\ - WES S16 C15 + WEC S16 S15 - \hat{x}_4 C17 \hat{E}_{12} \\ - \hat{x}_6 S17 \hat{E}_{32}] / C16$$

$$F_{15,16} = [\hat{x}_4 C17 \hat{E}_{23} (2 \hat{x}_{13} S17 - C17) - \hat{E}_{22} WEC \\ - \hat{E}_{23} (WES + \hat{x}_6 S17 S17)] / C16 + (S16 C17 \hat{\omega}_{xp} \\ + S16 S17 \hat{\omega}_{zp}) / (C16 C16)$$

$$F_{15,17} = [\hat{x}_4 \hat{x}_{13} (S16 S15 C217 - 2 C17 S17 C15) \\ + WES C15 - WEC S15 + \hat{x}_4 C17 \hat{E}_{33} \\ - \hat{x}_6 S17 \hat{E}_{13} - \hat{\omega}_{xp} S17 + \hat{\omega}_{zp} C17] / C16$$

$$F_{16,1} = \hat{x}_{13} C17 + S17$$

$$F_{16,3} = - C17$$

$$F_{16,4} = \hat{x}_{13} (S16 S15 C217 - 2 S17 C17 C15) + S17 \hat{E}_{13}$$

$$F_{16,6} = - C17 \hat{E}_{33}$$

$$F_{16,13} = \hat{x}_4 (S16 S15 C217 - 2 S17 C17 C15) + C17 (\hat{x}_1 + TGX)$$

$$F_{16,15} = \hat{x}_4 \hat{x}_{13} (S16 C15 C217 + 2 C17 S17 S15 + C15 WEC \\ + S15 WES - \hat{x}_6 C17 \hat{E}_{32} + \hat{x}_4 S17 \hat{E}_{12})$$

$$F_{16,16} = \hat{E}_{23} [\hat{x}_4 \hat{x}_{13} C217 + C17 S17 (\hat{x}_4 - \hat{x}_6)]$$

$$F_{16,17} = -\hat{\omega}_{xp} C17 - \hat{\omega}_{zp} S17 - \hat{x}_4 \hat{x}_{13} (2 C17 S17 S16 S15 \\ + C15 C217) - WEC S16 C15 - S16 S15 WES \\ - \hat{x}_6 C17 \hat{E}_{13} - \hat{x}_4 S17 \hat{E}_{33}$$

$$F_{17,1} = S16 F_{15,1}$$

$$F_{17,2} = -1$$

$$F_{17,3} = S16 F_{15,3}$$

$$F_{17,4} = S16 F_{15,4}$$

$$F_{17,5} = -\hat{E}_{23}$$

$$F_{17,6} = S16 F_{15,6}$$

$$F_{17,13} = S16 F_{15,13}$$

$$F_{17,15} = S16 F_{15,15} - \hat{E}_{22} (\hat{x}_5 + WES) + WEC \hat{E}_{23}$$

$$F_{17,16} = S16 F_{15,16} + S16 S15 (\hat{x}_5 + WES) + WEC S16 C15 \\ + \hat{\omega}_{xp} C17 + \hat{\omega}_{zp} S17$$

$$F_{17,17} = S16 F_{15,17}$$

The partials of the measurement function are defined by the following (3×17) matrix of partial derivatives.

$$H[\hat{x}(t_n | t_{n-1})] \triangleq \left[\frac{\partial h_i[\hat{x}(t_n | t_{n-1})]}{\partial x_j} \right] \quad (C.3)$$

$$i = 1, 2, 3 \quad j = 1, 2, \dots, 17$$

where

h_i - are the elements of $\underline{h}(\underline{x})$ defined in Section 5

$\hat{x}(t_n | t_{n-1})$ - are the predicted state estimates

The following is a list of the nonzero elements of H . All elements not listed are zero.

Define

$$\hat{x}_i^* = \hat{x}_i(t_n | t_{n-1}) \quad i = 1, 2, \dots, 17$$

$\hat{E}_{ij}^*(i, j = 1, 2, 3)$ - are the elements of E evaluated at \hat{x}_i^*

$$S15 = \sin(\hat{x}_{15}^*)$$

The nonzero elements of H are

$$H_{1,7} = 1$$

$$H_{1,10} = \hat{E}_{13}^* - \hat{x}_{14}^* \hat{E}_{23}^*$$

$$H_{1,14} = -\hat{x}_{10}^* \hat{E}_{23}^*$$

$$H_{1,15} = \hat{x}_{10}^* (\hat{E}_{12}^* - \hat{x}_{14}^* \hat{E}_{22}^*)$$

$$H_{1,16} = S_{15} \hat{x}_{10}^* (\hat{E}_{11}^* - \hat{E}_{21}^* \hat{x}_{14}^*)$$

$$H_{1,17} = -\hat{x}_{10}^* \hat{E}_{33}^*$$

$$H_{2,8} = 1$$

$$H_{2,11} = \hat{E}_{23}^*$$

$$H_{2,15} = \hat{x}_{11}^* \hat{E}_{22}^*$$

$$H_{2,16} = S_{15} \hat{x}_{11}^* \hat{E}_{21}^*$$

$$H_{3,9} = 1$$

$$H_{3,12} = \hat{E}_{33}^*$$

$$H_{3,15} = \hat{x}_{12}^* \hat{E}_{32}^*$$

$$H_{3,16} = \hat{x}_{12}^* S_{15} \hat{E}_{31}^*$$

$$H_{3,17} = \hat{x}_{12}^* \hat{E}_{13}^*$$

C.2 ANALYTIC PARTIALS FOR THE CENTRIFUGE SIMULATION

The partials of the state function are defined by the following
(10 × 10) matrix of partial derivatives.

$$F[\hat{x}(t_{n-1}|t_{n-1}), t] \triangleq \left[\frac{\partial f_i[\hat{x}(t_{n-1}|t_{n-1}), t]}{\partial x_j} \right] \quad (C.4)$$

$$i, j = 1, 2, \dots, 10$$

where

f_i - are the elements of $\underline{f}(\underline{x}, t)$ defined in Section 6

$\hat{\underline{x}}(t_{n-1} | t_{n-1})$ - are the filtered state estimates

As in Section C.1, only the last three rows of F are required to be evaluated, since the first seven rows contain zero elements.

$$F_{ij} = 0 \text{ for } \begin{matrix} i = 1 \text{ thru } 7 \\ j = 1 \text{ thru } 10 \end{matrix} \quad (\text{C.5})$$

The following is a list of the nonzero elements of F in the last three rows. All elements not listed are zero.

Define

$$\hat{\underline{x}}_i = \hat{\underline{x}}_i(t_{n-1} | t_{n-1}) \quad i = 1, 2, \dots, 10$$

$\hat{E}_{ij}(i, j = 1, 2, 3)$ - are the elements of the Euler transformation matrix defined in Section 6, evaluated at $\hat{\underline{x}}_i$

$\hat{\omega}_{xp}, \hat{\omega}_{zp}$ - are the platform rate equations defined in Section 6, evaluated at $\hat{\underline{x}}_i$

$\hat{A}X, \hat{A}Y, \hat{A}Z$ - are the elements of the applied acceleration (AX, AY, AZ) defined in Section 6, evaluated at \hat{E}_{ij}

$D_{IY}, D_{OZ}, D_{IX}, G1, G2, \omega_c t$ - are parameters defined in Section 6

$$x_5 \equiv \hat{x}_3$$

$$x_6 \equiv \hat{x}_4$$

$$C10 = \cos(x_{10}) \equiv \cos(\hat{x}_8)$$

$$C11 = \cos(x_{11}) \equiv \cos(\hat{x}_9)$$

$$C12 = \cos (x_{12}) \equiv \cos (\hat{x}_{10})$$

$$S10 = \cos (x_{10}) \equiv \cos (\hat{x}_8)$$

$$S11 = \cos (x_{11}) \equiv \cos (\hat{x}_9)$$

$$S12 = \cos (x_{12}) \equiv \cos (\hat{x}_{10})$$

The above identities are based on the structure of the centrifuge simulation. As explained in Section 6, there are 12 state variables that are structured into a 10-element state vector for three different options of the simulation program. Therefore, the above identities show the relationship between the state variables and the elements of the state vector for the F partials. The state vector represents different state variables for each option, implying that the analytic partials will be different. The changes for each option are identified below.

Define

$$C = \cos (\omega_c t)$$

$$S = \sin (\omega_c t)$$

$$G = 1.0 + G2*S \text{ where } * \text{ represents the product of the two variables.}$$

$$G1E13 = G1*\hat{E}_{13}*S + \hat{E}_{12}*G$$

$$WECE13 = WEC*\hat{E}_{13} - WES*\hat{E}_{12}$$

$$G1E23 = G1*\hat{E}_{23}*S + \hat{E}_{22}*G$$

$$G1E33 = G1*\hat{E}_{33}*S + \hat{E}_{32}*G$$

$$WECE33 = WEC*\hat{E}_{33} - WES*\hat{E}_{32}$$

$$G1S11 = G1*(S11*C - \hat{E}_{22}*S) + \hat{E}_{23}*G$$

$$G1C11 = G1*(C11*C - C10*\hat{E}_{21}*S) + S10*\hat{E}_{21}*G$$

$$G1E21 = G1*(\hat{E}_{21}*C + \hat{E}_{22}*S) - \hat{E}_{23}*G$$

$$WECE22 = WEC*\hat{E}_{22} + WES*\hat{E}_{23}$$

$$G1E31 = G1*(\hat{E}_{31}*C + \hat{E}_{32}*S) - \hat{E}_{33}*G$$

$$WECE32 = WEC*\hat{E}_{32} + WES*\hat{E}_{33}$$

$$G1E11 = G1*(\hat{E}_{11}*C + \hat{E}_{12}*S) - \hat{E}_{13}*G$$

$$WECE12 = WEC*\hat{E}_{12} + WES*\hat{E}_{13}$$

For the Basic Option we define

$$x_3 \equiv \hat{x}_1$$

The nonzero partials for the Basic Option are

$$F_{8,1} = -C12/C11*\hat{A}X$$

$$F_{8,4} = -S12/C11*\hat{A}Z*\hat{A}Y$$

$$F_{8,8} = \left\{ C12(-x_3*G1E13 + WECE13) + S12[-D_{OZ}*G1E13 - x_6(\hat{A}Z*G1E23 + \hat{A}Y*G1E33) + WECE33] \right\} / C11$$

$$F_{8,9} = \left\{ C12 \left[C12(-x_3 * G1S11 - WECE22) \right. \right. \\ \left. \left. + S12 \left[-D_{OZ} * C12 * G1S11 - x_6(\hat{A}Z * G1C11 \right. \right. \right. \\ \left. \left. - \hat{A}Y * S12 * G1E21) - S12 * WECE22 \right] \right\} / C11 \\ + S11(\hat{\omega}_{xp} * C12 + \hat{\omega}_{zp} * S12) / (C11 * C11)$$

$$F_{8,10} = \left\{ C12(-x_3 * G1E31 + WECE32) - S12 * \hat{\omega}_{xp} \right. \\ \left. + S12(-D_{OZ} * G1E31 + x_6 * \hat{A}Y * G1E11 \right. \\ \left. - WECE12) + \hat{\omega}_{zp} * C12 \right\} / C11$$

$$F_{9,1} = S12 * \hat{A}X$$

$$F_{9,4} = -C12 * \hat{A}Z * \hat{A}Y$$

$$F_{9,8} = C12 \left[-D_{OZ} * G1E13 - x_6(\hat{A}Z * G1E23 + \hat{A}Y * G1E33) \right. \\ \left. + WECE33 \right] - S12(-x_3 * G1E13 + WECE13)$$

$$F_{9,9} = C12 \left[-D_{OZ} * C12 * G1S11 - x_6(\hat{A}Z * G1C11 \right. \\ \left. - \hat{A}Y * S12 * G1E21) - S12 * WECE22 \right] \\ - S12 \left[C12(-x_3 * G1S11 - WECE22) \right]$$

$$F_{9,10} = C12(-D_{OZ} * G1E31 + x_6 * \hat{A}Y * G1E11 - WECE12 \\ - \hat{\omega}_{xp}) - S12(-x_3 * G1E31 + WECE32 + \hat{\omega}_{zp})$$

$$F_{10,1} = S11 * F_{8,1}$$

$$F_{10,3} = -\hat{A}Z * \hat{A}Z$$

$$F_{10,4} = S_{11} * F_{8,4}$$

$$F_{10,8} = S_{11} * F_{8,8} - D_{IY} * G_{1E23} - 2x_5 * \hat{A}Z * G_{1E33} \\ + WEC * \hat{E}_{23} - WES * \hat{E}_{22}$$

$$F_{10,9} = S_{11} * F_{8,9} - D_{IY} * G_{1C11} + 2x_5 * \hat{A}Z * S_{12} * G_{1E21} \\ - \hat{E}_{21} (WEC * C_{10} + WES * S_{10}) + \hat{\omega}_{xp} * C_{12} + \hat{\omega}_{zp} * S_{12}$$

$$F_{10,10} = S_{11} * F_{8,10} + 2x_5 * \hat{A}Z * G_{1E11}$$

For Option 1 we define

$$x_3 \equiv D_{IX}$$

The nonzero partials for Option 1 are

$$F_{8,1} = -C_{12}/C_{11}$$

$$F_{9,1} = S_{12}$$

$$F_{10,1} = S_{11} * F_{8,1}$$

All the rest of the partials of Option 1 are identical with those of the Basic Option with $x_3 = D_{IX}$.

For Option 2 we define

$$x_3 \equiv \hat{x}_2$$

The nonzero partials of Option 2 are

$$F_{8,2} = -C12/C11 * \hat{A}\hat{X}$$

$$F_{9,2} = S12 * \hat{A}\hat{X}$$

$$F_{10,2} = S11 * F_{8,2}$$

All the rest of the partials of Option 2 are identical with those of the Basic Option with $x_3 = \hat{x}_2$.

The partials of the measurement function are defined by the following (3×10) matrix of partial derivatives.

$$H[\hat{x}(t_n | t_{n-1}), t_n] \triangleq \left[\frac{\partial h_i[\hat{x}(t_n | t_{n-1}), t_n]}{\partial x_j} \right]$$

C. 6

$$i = 1, 2, 3 \quad j = 1, 2, \dots, 10$$

where

h_i - are the elements of $\underline{h}(\underline{x}, t)$ defined in Section 6

$\hat{x}(t_n | t_{n-1})$ - are the predicted state estimates

The following is a list of the nonzero elements of H. As was the case for the F matrix, the structure of H is based on the program options.

Define

$$\hat{x}_i^* = \hat{x}_i(t_n | t_{n-1}) \quad i = 1, 2, \dots, 10$$

$\hat{E}_{ij}^*(i, j = 1, 2, 3)$ - are the elements of E evaluated at \hat{x}_i^*

$$x_7 \equiv \hat{x}_5^*$$

$$x_8 \equiv \hat{x}_6^*$$

$$x_9 \equiv \hat{x}_7^*$$

$\hat{A}X^*, \hat{A}Y^*, \hat{A}Z^*$ - are the elements of the applied acceleration evaluated at \hat{E}_{ij}^*

K_{1X}, K_{1Y}, K_{1Z} - are parameters defined in Section 6

$$C = \cos(\omega_c t_n)$$

$$S = \sin(\omega_c t_n)$$

$$G = 1.0 + G_2^* S$$

$C10, C11$, etc. - are the same as for the F partials with \hat{x}_i replaced by \hat{x}_i^*

Let

$$AX \equiv \hat{A}X^*$$

$$AY \equiv \hat{A}Y^*$$

$$AZ \equiv \hat{A}Z^*$$

$$E_{ij} \equiv \hat{E}_{ij}^* \text{ for } i, j = 1, 2, 3$$

Define

$$X4X9 = x_4 - x_9 * AZ$$

$$X9AX = x_9 * AX$$

$$G1E33 = G1 * E_{33} * S + E_{32} * G$$

$$G1E21 = G1(E_{21} * C + E_{22} * S) - E_{23} * G$$

$$G1E11 = G1(E_{11} * C + E_{12} * S) - E_{13} * G$$

$$K1Y2X7 = K_{1Y} + 2x_7 * AY$$

$$K1Z3X8 = K_{1Z} + 3x_8 * AZ * AZ$$

For the Basic Option we define

$$x_4 \equiv \hat{x}_2^*$$

The nonzero partials for the Basic Option are

$$H_{1,2} = AX$$

$$H_{1,7} = -AX * AZ$$

$$H_{1,8} = (G1 * E_{13} * S + E_{12} * G) * X4X9 - X9AX * G1E33$$

$$H_{1,9} = -G1E21(C12 * X4X9 - X9AX * S12)$$

$$H_{1,10} = (G1 * E_{31} * C + G1 * E_{32} * S - E_{33} * G) * X4X9$$

$$+ X9AX * G1E11$$

$$H_{2,5} = AY * AY$$

$$H_{2,8} = (G1 * E_{23} * S + E_{22} * G) * K1Y2X7$$

$$H_{2,9} = [G1(C11 * C - C10 * E_{21} * S) + S10 * E_{21} * G] * K1Y2X7$$

$$H_{3,6} = (AZ)^3$$

$$H_{3,8} = G1E33 * K1Z3X8$$

$$H_{3,9} = -S12 * G1E21 * K1Z3X8$$

$$H_{3,10} = -G1E11 * K1Z3X8$$

Option 1 partials are identical to those for the Basic Option.

For Option 2 we define

$$x_4 \equiv K_1X$$

$$H_{1,1} = 1.0$$

and the partials are identical to the Basic Option with $x_4 = K_1X$

This completes the analytic partials for the centrifuge simulation.